

**Emission of Energetic Neutral Atoms from the
Magnetosphere-Atmosphere Interactions at Callisto
and Europa**

C. Michael Haynes¹, Tyler Tippens¹, Peter Addison¹, Lucas Liuzzo², Andrew
R. Poppe², Sven Simon^{1,3}

¹School of Earth and Atmospheric Sciences, Georgia Institute of Technology, Atlanta, Georgia, USA

²Space Sciences Laboratory, University of California, Berkeley, California, USA

³School of Physics, Georgia Institute of Technology, Atlanta, Georgia, USA

Key Points:

- We model the energetic neutral atom (ENA) flux generated by charge exchange of magnetospheric ions with Callisto's and Europa's atmospheres
- The bulk of the ENA flux is detectable in a band normal to the magnetospheric field and created by ions with pitch angles near 90 degrees
- Magnetic field line draping attenuates the intensity of observable ENA flux and qualitatively alters the emission morphology at both moons

16 **Abstract**

17 We analyze the emission of energetic neutral atom (ENA) flux from charge exchange be-
 18 tween Jovian magnetospheric ions and the atmospheres of Callisto and Europa. For this
 19 purpose, we combine the draped electromagnetic fields from a hybrid plasma model with
 20 a particle tracing tool for the energetic ions. We determine the ENA flux through a con-
 21 centric sphere located just outside of each moon's atmosphere, thereby capturing the com-
 22 plete physics imprinted in these emission patterns. In order to constrain the modifica-
 23 tions to the ENA emissions that arise from the periodic change of the ambient plasma
 24 conditions, we calculate the emission morphology at multiple positions during a Jovian
 25 synodic rotation. To isolate the influence of field line draping, we compare to the emis-
 26 sion patterns in uniform fields. Our major results are: (a) At Europa and Callisto, the
 27 majority of detectable ENA emissions are concentrated into a band normal to the Jo-
 28 vian magnetospheric field. (b) The fraction of observable ENA flux that contributes to
 29 this band depends on the number of complete gyration that the parent ions can com-
 30 plete within the moon's atmosphere. (c) Field line draping partially deflects impinging
 31 parent ions around both moons, thereby attenuating the ENA flux and driving signif-
 32 icant morphological changes to the emission patterns. (d) The band of elevated ENA flux
 33 is locally maximized on the opposite (antipodal) side of the moon where the flux is lo-
 34 cally minimized. At Europa, detectable ENA emissions are maximized slightly west of
 35 the ramside apex. At Callisto, they maximize near the Jupiter-facing apex.

36 **1 Introduction**

37 The Galilean satellites Callisto and Europa possess nearly circular, tidally locked,
 38 prograde orbits that approximately coincide with Jupiter's equatorial plane and are em-
 39 bedded within the giant planet's magnetosphere. Europa (radius $R_E = 1,560.8$ km) or-
 40 bits Jupiter at a mean radial distance of $9.4R_J$ (where $R_J = 71,492$ km is Jupiter's equa-
 41 torial radius), and Callisto (radius $R_C = 2,410.3$ km) is found at its mean orbital ra-
 42 dius of $26.3R_J$. Both moons possess tenuous atmospheres (e.g., Hall et al., 1995; Cun-
 43 ningham et al., 2015; Vorburger et al., 2015; Plainaki et al., 2018) with molecular oxy-
 44 gen as the primary constituent (e.g., Saur et al., 2011; Roth et al., 2016; Carberry Mo-
 45 gan et al., 2020). Callisto's atmosphere was also observed to possess a carbon dioxide
 46 component several orders of magnitude less dense than the molecular oxygen (Carlson,
 47 1999). In addition, recent modeling provides initial evidence of an appreciable molec-

48 ular hydrogen component in Callisto's atmosphere (Carberry Mogan et al., 2022). The
49 atmosphere of Europa also shows evidence of a localized H₂O profile concentrated above
50 the subsolar trailing apex (Roth, 2021). In contrast to the transient plumes of water va-
51 por detected at Europa on various occasions (Roth, Saur, et al., 2014; Jia et al., 2018;
52 Arnold et al., 2019; Paganini et al., 2019), this atmospheric H₂O component appears to
53 be persistent, i.e., it does not vary drastically with time. The primary ionization mech-
54 anisms of these atmospheres are photoionization at Callisto (e.g., Hartkorn et al., 2017)
55 and electron impact ionization at Europa (Saur et al., 1998; Roth, Rutherford, et al., 2014;
56 Carberry Mogan et al., 2023). Charge exchange interactions between impinging mag-
57 netospheric ions and neutral atmospheric particles further contribute to atmospheric ion-
58 ization (Lindsay & Stebbings, 2005; Dennerl, 2010).

59 Jupiter's vast magnetosphere is generated by the interaction between the planet's
60 internal magnetic field and the solar wind. Jupiter's internal dipole moment is tilted by
61 9.6° with respect to its axis of rotation. This inclination causes the magnetic latitude
62 at the locations of Europa and Callisto to periodically vary. In Jupiter's immediate vicin-
63 ity, the magnetospheric field is primarily given by the superposition of the dipole and
64 quadrupole terms of the planet's internal field (Connerney et al., 2022). At equatorial
65 distances beyond $\approx 5R_J$, the magnetospheric field becomes increasingly stretched in the
66 radial direction from the growing magnetodisc contribution (e.g., Connerney et al., 2020).
67 Accordingly, near Callisto, the field at times is largely parallel to the moon's orbital plane.
68 However, the ambient magnetospheric field at Europa's orbit is still predominantly south-
69 ward (Kivelson et al., 1999; Vance et al., 2021).

70 The periodic migration of Jupiter's magnetic equator sweeping past Callisto and
71 Europa manifests as a time-varying horizontal component and a nearly constant north-
72 south component of Jupiter's magnetospheric field at the orbit of each moon (Kivelson
73 et al., 1999; Connerney et al., 2022). The time variability of the horizontal component
74 generates an induction signal in conducting regions of both moons that possesses mul-
75 tiple excitation periods, the respective moon's synodic orbital period being the domi-
76 nant cycle by about an order of magnitude (Kivelson et al., 1999; Zimmer et al., 2000;
77 Seufert et al., 2011). Induced magnetic fields at Europa mainly stem from a salty sub-
78 surface ocean under its icy crust (Kivelson et al., 2000; Vance et al., 2021). Currents in
79 Europa's ionosphere produce a secondary induction signal a small fraction (<1%) of the
80 amplitude attributed to the oceanic induction signature (Hartkorn & Saur, 2017). Al-

81 ternatively, the dominant conducting source region at Callisto, whether it be a subsur-
 82 face ocean (e.g., Khurana et al., 1998; Zimmer et al., 2000), an anisotropic, conductive
 83 ionosphere (Hartkorn & Saur, 2017; Vance et al., 2021), or some combination of the two
 84 is under debate. The induced field can be approximately described by a dipole centered
 85 at each moon, with their magnetic moments antiparallel to the Jovian inducing compo-
 86 nent (Saur et al., 2010; Vance et al., 2018).

87 Europa and Callisto are constantly overtaken by a sub-corotating population of ther-
 88 mal magnetospheric plasma (e.g., Kivelson et al., 2004; Bagenal et al., 2015, 2016), con-
 89 fined to a disc-shaped equatorial plasma sheet that is centered near the Jovian magnetic
 90 equator (e.g., Bagenal & Delamere, 2011). This plasma is incident upon both moons'
 91 trailing hemispheres with a relative bulk velocity on the order of 100 km/s (Kivelson et
 92 al., 2004; Bagenal et al., 2015). The ion population within Jupiter's plasma sheet is mostly
 93 comprised of protons, oxygen, and sulfur (Bagenal et al., 2015; Kim et al., 2020). The
 94 vertical and radial profiles of the plasma density within the sheet has been empirically
 95 modeled using Voyager and Galileo observations: the number density of the plasma sheet
 96 decreases with a Gaussian profile as a function of north-south distance to its center.

97 Ionization of Europa's and Callisto's neutral envelopes creates a population of pickup
 98 ions. The acceleration of these pickup ions by the magnetospheric fields drains momen-
 99 tum from the incident flow, slowing and diverting the magnetospheric plasma around
 100 each moon (e.g., Rubin et al., 2015; Liuzzo et al., 2016). As the impinging flow is slowed,
 101 the frozen-in magnetospheric field drapes around the moon and piles up at the ramside
 102 of either satellite. At Callisto, the large gyroradii of ionospheric pickup ions impose sub-
 103 stantial hemispherical asymmetries on the perturbed electromagnetic field patterns (Liuzzo
 104 et al., 2015). At large distances from these moons' interaction regions, a system of Alfvén
 105 wings is generated that ultimately connect to the Jovian ionosphere (Neubauer, 1980,
 106 1998). The presence of an induced dipole field reduces the cross sections of the Alfvén
 107 wing tubes and the strength of the wing-aligned currents, compared to a scenario with-
 108 out induction (Neubauer, 1999).

109 There also exists a population of magnetically confined energetic ($E \geq 1$ keV) elec-
 110 trons and ions that simultaneously drift azimuthally through Jupiter's magnetosphere
 111 and bounce along field lines between mirror points (e.g., Paranicas et al., 2000, 2009; Koll-
 112 mann et al., 2017; Shen et al., 2022). The influx pattern of the energetic ion population

onto the surfaces of Callisto and Europa differs from that of the thermal population due to the larger gyroradii and significant field-aligned velocity components that grant the energetic ions increased access to both moons' polar regions (e.g., Liuzzo et al., 2019b; Addison et al., 2021, 2022). Field line draping and the induced dipole significantly reduce and redistribute energetic ion precipitation patterns compared to uniform fields (Liuzzo et al., 2019b, 2022; Addison et al., 2021; Nordheim et al., 2022). At Callisto, the draping pattern protects the ramside from energetic ion precipitation in the keV range, while MeV ions can still access the moon uniformly. The induced dipole field tends to focus energetic ions into the regions where the axis of the dipole moment intersects Callisto's surface. (Liuzzo et al., 2019a). When Europa is located near the center of the Jovian plasma sheet, field line draping acts to shield the ramside from heavy precipitation by magnetospheric ions. In this configuration, the draping is the strongest, and the energetic ion influx around the moon's ramside apex is minimized compared to large distances to the center of the Jovian plasma sheet (Addison et al., 2021). At high polar latitudes, the influx differs between the ramside and wakeside hemispheres by about a factor of two (Addison et al., 2021). The sensitivity of energetic ion trajectories at Europa and Callisto to the local field perturbations necessitates the inclusion of both the plasma interaction and the induced dipole when analyzing energetic ion dynamics in either moon's vicinity.

Energetic neutral atoms, henceforth referred to as ENAs, are generated when impinging energetic ions undergo charge exchange with cold neutral particles from a Europa's or Callisto's atmosphere. The cold ion produced by the charge exchange interaction is picked up by the ambient magnetospheric fields and swept downstream, draining momentum from the flow (e.g., Mitchell et al., 2005). The charge exchange process is forward-scattered (Johnson et al., 1988; Lindsay & Stebbings, 2005), allowing the freshly neutralized energetic particle to retain its velocity at the instant of the charge exchange. The energy lost due to gravitation by an ENA traveling through Jupiter's magnetosphere is negligible, so its ballistic trajectory is rectilinear, similar to that of a photon emitted from a light source (e.g., Mauk et al., 2003; Mitchell et al., 2005). The strong dependence of energetic ion trajectories at Europa and Callisto on perturbations in the local electromagnetic fields inherently imprints information about the field configuration on the pattern of emitted ENAs. As such, the morphology of ENA emissions from a moon's atmosphere can help constrain the structure of the moon-magnetospheric interaction re-

145 gion (see also Dandouras & Amsif, 1999; Wulms et al., 2010; Kabanovic et al., 2018; Tip-
146 pens et al., 2022).

147 ENA detectors capture ENA emissions as an image, analogous to how cameras de-
148 tect photons (Mitchell et al., 1993). Specifically, such ENA imagers produce a two-dimensional
149 “snapshot” of the ENA flux integrated along the detectors’ lines of sight. Therefore, ENA
150 imaging of a moon’s interaction region can greatly facilitate the interpretation of in-situ
151 plasma and field data that is only captured along a one-dimensional spacecraft trajec-
152 tory. The information contained in a single ENA snapshot can potentially reveal features
153 of the plasma interaction as a whole that could otherwise be identified only through re-
154 peated flybys with duplicate trajectories that occur under similar upstream conditions
155 (e.g., Wulms et al., 2010; Kabanovic et al., 2018; Tippens et al., 2022). ENA observa-
156 tions in concert with plasma and electromagnetic field data therefore provide powerful
157 remote sensing capabilities for observing moon-magnetosphere interactions.

158 ENAs associated with the moons of the outer solar system have been observed both
159 from Europa’s neutral gas torus (Mauk et al., 2003, 2020) and as a result of the inter-
160 action between Saturn’s magnetosphere and Titan’s atmosphere (e.g., Mitchell et al., 2005;
161 Smith et al., 2009; Brandt et al., 2012). At the time of this writing, Cassini is the only
162 spacecraft to have visited the outer solar system with an ENA camera aboard (Mitchell
163 et al., 1996; Krimigis et al., 2004). In late 2000, the Ion and Neutral Camera (INCA)
164 imaged the Jovian magnetosphere as the spacecraft reached its closest approach distance
165 of about $140R_J$. INCA observed ENAs in the (50–80) keV energy channel, primarily
166 generated by charge exchange interactions with magnetospheric H^+ ions. The observed
167 ENA emission pattern resembled an elliptical cloud possessing three distinct intensity
168 maxima, one of which was produced by charge exchange with the Jovian atmosphere.
169 The two weaker emission peaks, located at a distance of $\approx 10R_J$ to the planet, were at-
170 tributed to the limb-brightened ansae of a dense, trans-Europian neutral gas torus viewed
171 edge-on by INCA (Mauk et al., 2003).

172 After advancing beyond the Jovian system, INCA observed ENA emissions dur-
173 ing more than 100 separate Titan flybys, including the initial pass on 26 October 2004
174 (denoted TA). These in-situ observations provided a plethora of ENA images of Titan’s
175 interaction with Saturn’s outer magnetosphere (e.g., Dandouras & Amsif, 1999; Mitchell
176 et al., 2005; Garnier et al., 2010). Similar to the Galilean moons, Titan’s interaction with

177 the impinging Kronian magnetospheric plasma results in strong magnetic field line drap-
 178 ing and pileup (e.g., Neubauer et al., 2006; Simon et al., 2015). Wulms et al. (2010) made
 179 a first step in constraining the impact of the draped fields on the morphology of ENA
 180 emissions at Titan. These authors combined the perturbed fields from an MHD model
 181 of Titan's interaction with a test particle tracer to analyze the motion of energetic pro-
 182 tons near Titan and their charge exchange with the moon's atmosphere. Modeling the
 183 ENA flux into a point-like detector, akin to INCA, is not feasible due to prohibitively
 184 few particle trajectories that would intersect the detector in the simulation. Therefore,
 185 Wulms et al. (2010) used a plane detector positioned at infinite distance to Titan that
 186 captured all ENAs approaching the detector approximately along its normal, partially
 187 emulating the limited field of view of the actual INCA detector.

188 Wulms et al. (2010) modeled Titan's ENA emission morphology both with draped
 189 magnetospheric fields and with a uniform background field as a baseline to constrain the
 190 contribution of the moon's plasma interaction to the emission signatures. Their mod-
 191 eled ENA flux maps for both uniform and draped fields revealed a crescent-shaped in-
 192 tensity distribution interrupted by a broad gap with nearly zero ENA flux. However, the
 193 ENA emissions in draped fields were found to be maximized on the opposite side of Ti-
 194 tan compared to the case of uniform fields; i.e, the crescent is rotated about Titan's po-
 195 lar axis by $\sim 180^\circ$ in longitude when draping is included, in agreement with the emis-
 196 sion pattern observed during TA. Thus, the results of Wulms et al. (2010) highlight the
 197 strong dependence of the ENA emission morphology on local magnetic field perturba-
 198 tions near the source of the ENAs.

199 Kabanovic et al. (2018) calculated the field perturbations at Titan during TA with
 200 the AIKEF (adaptive, kinetic ions, electron fluid) hybrid model (Müller et al., 2011)).
 201 They then implemented an ENA tracing model similar to that of Wulms et al. (2010),
 202 and compared their results using the hybrid model to the ENA emission maps obtained
 203 for draped fields from the preceding MHD model from Wulms et al. (2010). In contrast
 204 to the MHD picture, the hybrid approach captures the asymmetries in the magnetic drap-
 205 ing pattern at Titan that stem from the large gyroradii of ionospheric pick-up ions (Simon
 206 et al., 2007). Similar, large-scale asymmetries in the draped fields are also formed at Cal-
 207 listo (Liuzzo et al., 2015). When using the draped fields from the hybrid model and the
 208 same detector geometry as Wulms et al. (2010), the modeled ENA emissions were still
 209 found to possess a crescent-shaped intensity distribution. However, the broad emission

gap that interrupts the crescent in MHD fields (Wulms et al., 2010) is partially filled in. Kabanovic et al. (2018) also demonstrated that their modeled ENA emissions are reduced in magnitude by about a factor of two when the magnetospheric background field near Titan is increased from 3.77 nT to 6.0 nT. The emission gap captured by their plane detector was found to grow with ambient magnetospheric field strength because the decrease in gyroradii is accompanied with a reduced accessibility of Titan's atmosphere to energetic ions (see also Regoli et al., 2016). Ergo, even rather subtle changes to the draped magnetic fields leave a clearly discernible imprint in the ENA emission pattern at Titan.

Recently, Tippens et al. (2022) studied the impact of varying magnetospheric field orientations on Titan's ENA emission morphology using a combination of the AIKEF hybrid model and a test particle tracer, similar to Kabanovic et al. (2018). These authors employed a spherical ENA detector that encapsulates all of Titan's atmosphere. Such a detector geometry allows a comprehensive analysis of observable ENA generation at Titan without truncating any physical effects: due to its point-like nature (compared to the scale of the plasma interaction) and limited field of view, an actual space-craft detector would capture only a small fraction of the ENA flux emanated from Titan's atmosphere. Tippens et al. (2022) found that the majority of emitted ENAs are focused into an equatorial band of high flux perpendicular to the magnetospheric background field orientation. The latitudinal extension of this band is determined by the maximum altitude below which the bulk of the detectable ENA production takes place. Tippens et al. (2022) further established that ENA emissions through any segment of a global, spherical detector carry information from the entirety of the interaction region and are not necessarily determined by the regions of the atmosphere in closest proximity. In addition, these authors demonstrated that field line draping around Titan significantly reduces the overall intensity of the ENA emissions.

The Jupiter Energetic Neutrals and Ions (JENI) detector in the Particle Environment Package (PEP) on the JUpiter ICy moons Explorer (JUICE) spacecraft functions as an ENA camera (Grasset et al., 2013), the energy range of which is from around 1 keV up to several 100 keV (Galli et al., 2022). Charge exchange cross sections for protons with molecular oxygen (the primary constituent of Europa's and Callisto's atmospheres) fall precipitously at incident ion energies above 100 keV (Lindsay & Stebbings, 2005), suggesting that most ENAs emanating from these two moons' atmospheres will be observ-

able between about 1–100 keV. The JUICE spacecraft is scheduled to target both Europa and Callisto for multiple flybys (e.g., Grasset et al., 2013; Liuzzo et al., 2018), and may capture ENA images at both moons in analogy to Cassini’s persistent ENA imaging of Titan’s interaction region.

The Europa neutral torus that was markedly apparent in the INCA observation of the Jovian system is sourced by escaping hydrogen from Europa’s atmosphere (Smith et al., 2019). Due to INCA resolution limitations and the large passing distance during Cassini’s flyby, there were no distinct observations of ENA emissions from Europa’s local interaction region. Europa’s neutral torus is approximately ten to twelve orders of magnitude less in peak number density than the atmosphere at the moon’s surface (Plainaki et al., 2018; Smith et al., 2019; Roth et al., 2023), suggesting that Europa’s atmosphere may serve as a highly localized source of intense ENA emissions. Callisto’s magnetospheric environment shares strong similarities with the conditions at Titan, including pickup ion gyroradii on the order of the respective moon’s diameter and an occasionally super-alfvénic upstream flow that gives rise to highly draped fields (Liuzzo et al., 2015; Simon et al., 2015). The atmospheric scale heights at Callisto and Titan are comparable (e.g., Vorburger et al., 2015; Carberry Mogan et al., 2020; Tippens et al., 2022, and references therein). In addition, the density of Titan’s upper atmosphere (above altitudes of 1,100 km) where observable ENAs are generated is comparable to the atmospheric density at Callisto (Liuzzo et al., 2015; Tippens et al., 2022). The upstream energetic proton flux at keV energies is 1-2 orders of magnitude stronger at Callisto than at Titan (e.g., Mauk et al., 2004; Regoli et al., 2018; Liuzzo et al., 2022). This suggests that intense, observable ENA emissions may be emanating from Callisto’s atmosphere.

An increase in the ambient magnetospheric field strength by about a factor of two at Titan already produced an extended ENA emission gap in the Saturn-averted hemisphere associated with the reduced gyroradii of the energetic parent ions (Kabanovic et al., 2018). Periodic variation of Callisto and Europa in magnetic latitude relative to the center of the Jovian plasma sheet is accompanied by similar (Europa) or even much stronger (Callisto) changes in the magnitude of the background field (Kivelson et al., 1999; Kivelson et al., 2004; Connerney et al., 2022). Analogous to Titan, this effect is expected to generate variations in ENA emission intensity and morphology.

To date, modeling of local ENA emissions at Europa and Callisto has not been carried out by any study. In light of the upcoming JUICE mission's ENA detection capabilities, we combine the AIKEF hybrid code (Müller et al., 2011) with a particle tracing tool to model global ENA emissions from Callisto's and Europa's atmospheres. In particular, our study seeks to address the following questions:

- What is the effect of magnetic field line draping on the intensity and morphology of ENA emissions originating from the atmospheres of Europa and Callisto?
- How does the variability in the moons' plasma environments during a Jovian synodic rotation drive changes in the global ENA emission signatures?
- How do ENA emission intensity and morphology at these moons vary as a function of magnetospheric parent ion energy?
- Do the anisotropies observed in the pitch angle distribution of energetic ions at Europa (Sarkango et al., 2023) map into the ENA emission patterns?
- Does Europa's localized water atmosphere, as recently identified by Roth (2021), leave a discernible imprint in the ENA emission morphology?

This work is structured as follows: the employed hybrid plasma and ENA particle tracing models are described in section 2. In section 3.1, we present the modeled perturbed field environments at each moon, as obtained from AIKEF. Section 3.2 discusses ENA emission maps generated for different electromagnetic field configurations at Europa. In sections 3.3 and 3.4, we investigate how anisotropies in the ambient protons' pitch angle distribution or a local water vapor "bulge" in the atmosphere affect the ENA emission morphology at Europa. Our results for ENA emissions at Callisto in uniform and draped fields are presented in section 3.5. A summary of analysis and conclusions drawn can be found in section 4.

2 Modeling ENA emissions

In section 2.1, we introduce the setup of the AIKEF hybrid model (Müller et al., 2011) applied to calculate the three-dimensional structure of the draped fields at each moon. Section 2.2 then describes our ENA generation model. Energetic protons are traced through the perturbed electromagnetic fields from AIKEF in each moon's local environment. As these ions interact with Callisto's or Europa's atmosphere, they undergo charge exchange and produce ENAs. These ENAs propagate along rectilinear ballistic trajec-

305 tories and may be detectable by a spacecraft. The same combination of AIKEF model
 306 and a particle tracing tool to calculate ENA emission patterns has already been applied
 307 at Titan (Kabanovic et al., 2018; Tippens et al., 2022).

308 At both moons, the right-handed Cartesian Satellite Interaction System with co-
 309 ordinates $\mathbf{r} = (x, y, z)$ is employed, where the origin lies at the center of the moon. The
 310 corresponding unit vectors of the basis are $(\hat{\mathbf{x}}, \hat{\mathbf{y}}, \hat{\mathbf{z}})$. Here, $\hat{\mathbf{z}}$ points northward and is aligned
 311 with the Jovian spin axis, and $\hat{\mathbf{y}}$ bears towards Jupiter. The unit vector $\hat{\mathbf{x}}$ completes the
 312 system and points in the direction of corotation. To describe the ENA flux emanating
 313 from various regions around the moons, we introduce the spherical West Longitude co-
 314 ordinate system. Longitude is defined as 0° at the moon's sub-Jovian apex, and increases
 315 westward. The downstream, anti-Jovian, and upstream apices are therefore located at
 316 90° W, 180° W, and 270° W, respectively. Latitude is given with 90° corresponding to
 317 the moon's geographic north pole and -90° to its south pole.

318 2.1 Modeling the Perturbed Electromagnetic Environments of Callisto 319 and Europa

320 We apply the AIKEF hybrid model (Müller et al., 2011) to calculate the three-dimensional
 321 structure of the perturbed electromagnetic fields near each moon. AIKEF has been uti-
 322 lized in numerous preceding studies of both Callisto (Liuzzo et al., 2015, 2016, 2017, 2018,
 323 2019a, 2019b, 2022) and Europa (Breer et al., 2019; Arnold et al., 2019; Arnold, Liuzzo,
 324 & Simon, 2020; Arnold, Simon, & Liuzzo, 2020; Addison et al., 2021, 2022). AIKEF quan-
 325 titatively replicated fine structures in Galileo magnetometer data from the Europa E26
 326 flyby that were consistent with the presence of a plume (Arnold et al., 2019). Output
 327 from the AIKEF model has also been found to agree well with magnetic field and plasma
 328 signatures observed by Galileo during Callisto flybys C3, C9 and C10 (Liuzzo et al., 2015,
 329 2016). The AIKEF model treats thermal ions as macroparticles and electrons as a mass-
 330 less, charge-neutralizing fluid. Therefore, it is capable of resolving asymmetries associ-
 331 ated with the ionospheric Hall effect or flow shear between magnetospheric and ionospheric
 332 species, as well as any asymmetries in the plasma interaction due to the large pick-up
 333 ion gyroradii at Callisto (e.g., Liuzzo et al., 2015, 2016). For a detailed description of
 334 the computations performed by AIKEF, the reader is referred to Müller et al. (2011) as
 335 well as any of our preceding publications on Callisto and Europa. The three-dimensional
 336 AIKEF datasets for Callisto that we use in this study have also been applied by Liuzzo

337 et al. (2022) in a companion study of energetic particle precipitation onto the top of that
 338 moon's atmosphere.

339 The extent of the AIKEF simulation domain is chosen such that the electromagnetic
 340 fields have returned to their undisturbed background values at its outer boundaries,
 341 except for two highly-localized regions within the Alfvén wing tubes. For Callisto's en-
 342 vironment, Liuzzo et al. (2022) applied a cubical domain with side length $30R_C$, centered
 343 at the moon. At Europa, we apply a cuboid-shaped domain with extensions of $-8R_E \leq$
 344 $x \leq 22R_E$ in the x dimension, $-10R_E \leq y \leq 10R_E$ in the y dimension, and $-30R_E \leq$
 345 $z \leq 30R_E$ in the z dimension analogous to Addison et al. (2021). At both moons we
 346 apply a hierarchically-gridded mesh to adequately resolve, e.g., the atmospheric scale height.
 347 Specifically, at Europa we use a grid resolution of $0.02R_E$ (31 km) for $|x|, |y|, |z| \leq 1.5R_E$,
 348 $0.04R_E$ for $1.5R_E < |x|, |y|, |z| \leq 3R_E$, and $0.08R_E$ for $|x|, |y|, |z| > 3R_E$. From the
 349 model of Liuzzo et al. (2022), we adopt a grid resolution of $0.05R_C$ (120 km), $0.1R_C$, and
 350 $0.2R_C$ in cubes of the same size (but scaled in units of R_C instead of R_E) at Callisto.

351 We seek to constrain the impact of different sets of magnetospheric upstream con-
 352 ditions on the shape and intensity of ENA emissions, so we consider *two model config-*
 353 *urations at each of the two moons*. We implement ambient plasma conditions that Eu-
 354 *ropa or Callisto encounter at the center of the Jovian plasma sheet and at the maximum*
 355 *distance below the center of the plasma sheet. The background magnetic field vectors*
 356 \mathbf{B}_0 *in each case are enumerated in Table 1. At Europa, the background field vectors are*
 357 *determined by a combination of the latest Juno magnetodisc and internal Jovian field*
 358 *models (Connerney et al., 2020, 2022). Callisto's orbit falls beyond the realm of appli-*
 359 *cability of the Juno magnetodisc model. Therefore, the hybrid model setup adopted from*
 360 *Liuzzo et al. (2022) implements a combination of the VIP4 model for Jupiter's internal*
 361 *field (Connerney et al., 1998) superimposed with the Khurana (1997) model of Jupiter's*
 362 *magnetodisc field.*

363 Near the center of the Jovian plasma sheet, the horizontal component $|\mathbf{B}_h|$
 364 $= \sqrt{B_{x,0}^2 + B_{y,0}^2}$ of the ambient magnetic field is weak compared to the southward $B_{z,0}$
 365 component at both moons (Kivelson et al., 1999; Connerney et al., 2020, 2022). At Eu-
 366 *ropa's orbit, the observed $|\mathbf{B}_h|$ at the center of the plasma sheet is about five times weaker*
 367 *than the southward component (Kivelson et al., 1999). When Callisto is located at the*
 368 *center of the sheet, $|\mathbf{B}_h|$ is weaker than 1 nT compared to the southward component $B_{z,0} =$*

Moon	Europa		Callisto	
Position w.r.t plasma sheet	Center	Below	Center	Below
\mathbf{B}_0 [nT]	(0, 0, -410.0)	(4.0, 209.0, -385.0)	(0, 0, -4.0)	(9.0, 35.3, -6.6)
$ \mathbf{B}_0 $ [nT]	410.0	438.1	4.0	37.0
$\mathbf{B}_h = (B_{x,0}, B_{y,0})$ [nT]	(0, 0)	(4.0, 209.0)	(0, 0)	(9.0, 35.3)
\mathbf{M}_{ind} [10^{27} J/nT]	(0, 0, 0)	(-0.01, -3.97, 0)	(0, 0, 0)	(-0.63, -2.50, 0)
n_0 [cm $^{-3}$]	200	40	0.15	0.04
$ \mathbf{u}_0 $ [km/s]	100	100	192	192
β_i	$4.6 \cdot 10^{-2}$	$3.8 \cdot 10^{-2}$	$1.6 \cdot 10^1$	$7.5 \cdot 10^{-3}$
β_e	$4.6 \cdot 10^{-2}$	$3.8 \cdot 10^{-2}$	$1.3 \cdot 10^{-1}$	$7.7 \cdot 10^{-4}$
$ \mathbf{v}_{A,0} $ [km/s]	147	351	56	1,006
M_A	0.68	0.28	3.45	0.19
M_S	2.20	2.20	0.86	2.10
M_{MS}	0.65	0.28	0.84	0.19

Table 1. AIKEF Model Parameters (\mathbf{B}_0 : Jovian magnetospheric background field, \mathbf{B}_h : horizontal components of the ambient magnetospheric field, \mathbf{M}_{ind} : induced magnetic moment, n_0 : upstream thermal plasma density, and \mathbf{u}_0 : sub-corotational flow velocity). Values of the plasma beta $\beta_s = \frac{2\mu_0 n_0 k_B T_s}{\mathbf{B}_0^2}$ are computed for thermal magnetospheric ion ($s=i$) and electron ($s=e$) species separately using temperatures T_s from Kivelson et al. (2004), where subscript s represents species. The Alfvén speed $|\mathbf{v}_{A,0}| = \frac{B_0}{\sqrt{\mu_0 m_0 n_0}}$ as well as Alfvénic (M_A), sonic (M_S), and magnetosonic (M_{MS}) Mach numbers are also given.

369 –4 nT. Thus, at the center of the plasma sheet, the tilt of the background field against
 370 the north-south direction at either moon does not exceed $\arctan(1/4) \approx 14^\circ$. To main-
 371 tain a diagnostically accessible geometry that allows straightforward analysis of the physics
 372 of ENA generation, we do not take into account the weak \mathbf{B}_h component for either moon
 373 at the center of the plasma sheet (see Table 1 and Liuzzo et al., 2022). In other words,
 374 we consider the magnetospheric field at the center of the sheet to be purely southward.
 375 As shown by Tippens et al. (2022) for Titan, the tilt of the ambient magnetospheric field
 376 vector would merely cause a corresponding rotation (by $< 14^\circ$) of the ENA emission

377 pattern against the z axis, but would not affect the physical mechanisms shaping the ENA
 378 flux distribution.

379 While we do consider the plasma interaction of each moon at maximum distance
 380 below the center of Jupiter's plasma sheet, we do not present a dedicated analysis of the
 381 corresponding scenario at maximum distance above the sheet. Between these two sce-
 382 narios, only the signs of the $B_{x,0}$ and $B_{y,0}$ components flip; the field magnitude remains
 383 largely unchanged (Kivelson et al., 1999; Bagenal et al., 2015; Connerney et al., 2020,
 384 2022). When moving from above to below the plasma sheet, certain features of the in-
 385 teraction (e.g., the pick-up tail or the magnetic pileup region) are relocated, but the in-
 386 volved physics does not change (e.g., Simon & Motschmann, 2009). Furthermore, the
 387 thermal plasma density is symmetric about the center of the plasma sheet, so the up-
 388 stream density is identical for equivalent positions above and below the center (Bagenal
 389 & Delamere, 2011; Roth, Retherford, et al., 2014). Thus, we expect the morphology of
 390 ENA emissions from either moon to possess the same key features at maximum distance
 391 above or below the center of the sheet.

392 When Callisto and Europa are at their maximum distance from the center of the
 393 Jovian plasma sheet, the moons' inductive responses are the strongest (assuming no phase
 394 lag). We follow numerous preceding studies and assume the inductive response to stem
 395 from a spherically symmetric, infinitely conducting region of the same size as the respec-
 396 tive moon. Such an approach was found to reproduce key features of Galileo magnetome-
 397 ter observations at both Europa (e.g., Zimmer et al., 2000; Arnold et al., 2019; Harris
 398 et al., 2021) and Callisto (e.g., Liuzzo et al., 2015; Rubin et al., 2015; Lindkvist et al.,
 399 2015). Under these conditions, the induced magnetic dipole moment \mathbf{M}_{ind} at either moon
 400 is centered at its core and given by

$$\mathbf{M}_{\text{ind}} = -\frac{2\pi R^3}{\mu_0} \mathbf{B}_{h,0} \quad , \quad (1)$$

401 where R is the moon's mean radius (i.e., $R = R_E$ at Europa and $R = R_C$ at Callisto).
 402 A more rigorous treatment of the inductive response would include e.g., finite conduc-
 403 tivity of the ocean layer, radial gradients in ocean temperature that map into the con-
 404 ductivity profile, as well as an anisotropic geometry of the conducting layer (e.g., Schilling
 405 et al., 2007; Seufert et al., 2011; Vance et al., 2021; Styczinski & Harnett, 2021). How-
 406 ever, as we will show in section 3, the induced dipole moment plays only a very subtle

407 role in shaping the ENA emission morphology at Europa and Callisto; i.e., we expect our
 408 results to be very robust against minor changes of this parameter.

409 The bulk velocity \mathbf{u}_0 of the incident magnetospheric flow at Europa ($\mathbf{u}_0 = 100 \text{ km/s} \hat{\mathbf{x}}$)
 410 is approximately 85% of rigid corotation. At Callisto, a value of $\mathbf{u}_0 = 192 \text{ km/s} \hat{\mathbf{x}}$ has
 411 been found to replicate Galileo magnetometer observations (Liuzzo et al., 2016, 2017).
 412 This is only approximately 60% of the local corotation velocity at Callisto's orbit (Kivelson
 413 et al., 2004). At Europa, the distribution of the thermal ions is given by a mixture of
 414 protons, atomic oxygen, and doubly-ionized atomic sulfur (Bagenal et al., 2016), with
 415 a mean upstream ion mass $m_0 \approx 18.5 \text{ amu}$ (Clark et al., 2020). The AIKEF simulations
 416 applied by Liuzzo et al. (2022) for Callisto include a thermal ion population that
 417 consists exclusively of atomic oxygen i.e., $m_0 \approx 16.0 \text{ amu}$ (e.g., Kivelson et al., 2004).
 418 At both moons, the Gaussian profile,

$$n_0(d) = n_{ps,0} \exp \left\{ - \left(\frac{d}{H_{ps}} \right)^2 \right\} , \quad (2)$$

419 describes the variation in the number density n_0 of the upstream thermal plasma as a
 420 function of vertical distance d to the center of the Jovian plasma sheet, with equatorial
 421 density $n_{ps,0}$ and vertical scale height of the plasma sheet H_{ps} . The parameters $n_{ps,0}$ and
 422 H_{ps} vary as a function of radial distance to Jupiter. Galileo observations from a large
 423 number of crossings near Europa's orbit, obtained by the Plasma Subsystem (PLS), sug-
 424 gest $n_{ps,0} = 50 \text{ cm}^{-3}$ with a scale height of $H_{ps} \approx 1.8R_J$ (Bagenal & Delamere, 2011).
 425 However, Roth, Retherford, et al. (2014) found that a base density value of $n_{ps,0} = 200 \text{ cm}^{-3}$
 426 with a vertical scale height of $H_{ps} \approx 0.9R_J$ is most suitable to reproduce Galileo Plasma
 427 Wave Subsystem (PWS) observations of the upstream density from the spacecraft's tar-
 428 geted Europa flybys (Kurth et al., 2001). We therefore apply the values of $n_{ps,0}$ and H_{ps}
 429 from Roth, Retherford, et al. (2014) to calculate the upstream density for our Europa
 430 model. At Callisto's orbit, the thermal plasma density at the center of the sheet has fallen
 431 to $n_{ps,0} = 0.15 \text{ cm}^{-3}$ and the scale height H_{ps} has enlarged to $3.7R_J$, in accordance with
 432 Galileo PLS observations (Bagenal & Delamere, 2011; Liuzzo et al., 2022).

433 We consider the atmospheres of both moons to be dominated by molecular oxy-
 434 gen, with a minor contribution from carbon dioxide at Callisto, consistent with model-
 435 ing results and Hubble Space Telescope (HST) observations (e.g., Saur et al., 2011; Cun-
 436 ningham et al., 2015; Liuzzo et al., 2015; Plainaki et al., 2018; Carberry Mogan et al.,
 437 2021). While additional traces of hydrogen are also present at both moons (e.g., Car-

438 berry Mogan et al., 2020; Roth, Rutherford, et al., 2017), these light particles do not ap-
 439 preciably drain momentum from the magnetospheric flow and therefore have negligible
 440 effect on the plasma interaction (see also Simon et al., 2007). At both Europa and Cal-
 441 listo, our treatment of the atmosphere includes an asymmetry in the neutral density pro-
 442 file such that the atmospheric density peaks at the ramside apex and is minimized at the
 443 wakeside apex, consistent with the models of Rubin et al. (2015), Liuzzo et al. (2015, 2016),
 444 Arnold et al. (2019), Addison et al. (2021), and Harris et al. (2021). It is thus defined
 445 with respect to ψ , the angle between a given position vector $\mathbf{r} = (x, y, z)$ and the $-\hat{\mathbf{x}}$
 446 axis. This angle is given by $\cos \psi = -x/|\mathbf{r}|$. At both moons, the neutral envelope is rep-
 447 resented by a barometric law for the density as a function of altitude h and a factor to
 448 prescribe the strength of the asymmetry as a function of ψ . The hybrid simulation re-
 449 sults adapted from Liuzzo et al. (2022) at Callisto utilize a neutral density profile (for
 450 both O₂ and CO₂) with scale heights $h_{i,C}$ (for species i), and surface density $n_{i,0}$ of the
 451 form

$$n_{n,i}(h, \psi) = n_{i,0} \cos\left(\frac{\psi}{2}\right) \exp\left(-\frac{h}{h_{i,C}}\right) , \quad \text{where } i = \text{O}_2, \text{CO}_2 . \quad (3)$$

452 The model of Liuzzo et al. (2022) uses a surface density of $n_{\text{O}_2,0} = 10^{16} \text{ m}^{-3}$ and a scale
 453 height $h_{\text{O}_2,C} = 230 \text{ km}$ to describe the molecular oxygen component. For the CO₂ con-
 454 stituent, these authors employ a surface density of $n_{\text{CO}_2,0} = 4 \cdot 10^{13} \text{ m}^{-3}$ and use $h_{\text{CO}_2,C} =$
 455 230 km. Their chosen parameters yield column densities for each species consistent with
 456 the observed (Carlson, 1999; Cunningham et al., 2015; Roth et al., 2016) as well as the
 457 modeled values (Vorburger et al., 2015).

458 For Europa's molecular oxygen atmosphere, we employ the asymmetric density pro-
 459 file implemented by Arnold et al. (2019), as well as Arnold, Liuzzo, and Simon (2020),
 460 and Addison et al. (2021, 2022):

$$n_n(h, \psi) = \begin{cases} n_{n,0} (1 + 10 \cos \psi) \exp\left(-\frac{h}{h_{s,E}}\right); & \psi \leq 90^\circ \\ n_{n,0} \exp\left(-\frac{h}{h_{s,E}}\right); & 90^\circ < \psi \leq 180^\circ \end{cases} . \quad (4)$$

461 Using a surface density of $n_{n,0} = 5 \cdot 10^{13} \text{ m}^{-3}$ and a scale height of $h_{s,E} = 100 \text{ km}$,
 462 this atmospheric model is concordant with HST observations of the molecular oxygen
 463 column density (Hall et al., 1995; Roth, Saur, et al., 2014; Plainaki et al., 2018), as well
 464 as estimates of the molecular oxygen column density utilizing Keck/HIRES observations
 465 of Europa's auroral emissions during Jupiter eclipses (de Kleer et al., 2023). The den-
 466 sity of Europa's dilute hydrogen corona is four orders of magnitude below that of the molec-

467 ular oxygen component (Roth, Retherford, et al., 2017). Therefore, we include it neither
 468 in AIKEF nor in our ENA generation model.

469 Recently, a persistent H₂O atmosphere above Europa's subsolar trailing apex was
 470 identified in HST observations (Roth, 2021). This water vapor atmosphere is estimated
 471 to have a surface density comparable to that of the molecular oxygen constituent. How-
 472 ever, it is tightly confined around Europa's subsolar apex (Cervantes & Saur, 2022). The
 473 number density profile of this additional component can be expressed as

$$n_{n,\text{H}_2\text{O}}(h, \varphi) = n_{\text{H}_2\text{O},0} \cos^\gamma \varphi \exp\left(-\frac{h}{h_{s,\text{H}_2\text{O}}}\right) , \quad (5)$$

474 where φ is the angle between a vector from the moon's center to the subsolar apex and
 475 the vector \mathbf{r} from the center of the moon to a certain point in the atmosphere. We use
 476 $\gamma = 6$, in analogy to Cervantes and Saur (2022), who found this value to be consistent
 477 with HST observations of the H₂O profile. In addition, we set the scale height to $h_{s,\text{H}_2\text{O}} =$
 478 138 km, and the surface density at the subsolar apex to $n_{0,\text{H}_2\text{O}} = 2.14 \cdot 10^{14} \text{ m}^{-3}$, con-
 479 sistent with the column density derived by Roth (2021). The ratio of the total numbers
 480 of H₂O to O₂ molecules in our model atmosphere is approximately 0.23, consistent with
 481 the latest constraints provided by observations of the moon's optical aurorae by de Kleer
 482 et al. (2023): these authors found a ratio of 0.25.

483 To constrain a possible contribution of the H₂O component to ENA emissions, we
 484 consider a single test case for Europa (situated at the center of the Jovian plasma sheet)
 485 with the inclusion of this profile *in addition to* the molecular oxygen component. Eu-
 486 ropa's subsolar apex and ramside apex were coincident during the occultation observa-
 487 tions that inferred the presence of the H₂O exosphere (Roth, 2021), leaving it ambigu-
 488 ous whether the H₂O bulge follows the subsolar point as Europa orbits Jupiter or remains
 489 concentrated around the trailing apex regardless of the moon's orbital position. We thus
 490 position the H₂O exosphere in the same configuration as it was observed, with the sub-
 491 solar and ramside apices coincident.

492 At Europa, electron impact ionization dominates photoionization by at least an or-
 493 der of magnitude (Saur et al., 1998), so we include only this process to generate the moon's
 494 ionosphere from its neutral envelope. Carberry Mogan et al. (2023) recently estimated
 495 a range of $3.3 \cdot 10^{-6} \text{ s}^{-1}$ to $13.6 \cdot 10^{-6} \text{ s}^{-1}$ for the rate of electron impact ionization of
 496 H₂O at Europa. This range of rates largely overlaps with that of the rates for electron
 497 impact ionization of O₂ at Europa ($1.66 \cdot 10^{-6} \text{ s}^{-1}$ – $8.5 \cdot 10^{-6} \text{ s}^{-1}$, see Carberry Mo-

498 gan et al. (2023)). Therefore, we proceed analogous to Arnold et al. (2019) and Cervantes
 499 and Saur (2022), who use the same cross sections for O₂ and H₂O. At Callisto, photoion-
 500 ionization plays the primary role in ionospheric generation (Hartkorn & Saur, 2017), man-
 501 dating its inclusion in the hybrid model. In addition, AIKEF takes into account an isotropic
 502 contribution from electron impacts to emulate Callisto's nightside ionosphere (e.g., Li-
 503 uzzo et al., 2015, 2022). The dayside and ramside apices are set to be coincident at Cal-
 504 listo for this study (see also Liuzzo et al., 2022).

505 2.2 ENA emission model

506 While the AIKEF model can, in principle, resolve the motion of energetic ion macropar-
 507 ticles, the velocities of particles in the keV regime are more than an order of magnitude
 508 greater than the bulk velocity of the thermal ions. Since the timestep in AIKEF is lim-
 509 ited by the Courant-Friedrichs-Lowy condition, treating thermal and energetic ion pop-
 510 ulations simultaneously would require a prohibitively minuscule timestep in the hybrid
 511 model. Near the orbits of Europa and Callisto, energetic ions carry only a small portion
 512 of the plasma's current density (Mauk et al., 2004; Kim et al., 2020). Thus, their weak
 513 contribution to the currents can be neglected when calculating the electromagnetic field
 514 perturbations. Instead, the energetic ions can be treated as test particles injected into
 515 the steady-state field configuration from AIKEF (analogous to, e.g., Breer et al., 2019;
 516 Addison et al., 2021, 2022; Liuzzo et al., 2019a, 2019b, 2022).

517 To determine the impact of field line draping on the morphology of ENA emissions
 518 at Europa and Callisto, we model ENA production in both the uniform magnetospheric
 519 background field \mathbf{B}_0 and in the draped fields at each moon, similar to Wulms et al. (2010),
 520 Kabanovic et al. (2018), and Tippens et al. (2022) for Titan. In the uniform case, the
 521 electric field is equivalent to the convective term, $\mathbf{E}_0 = -\mathbf{u}_0 \times \mathbf{B}_0$. We consider mo-
 522 noenergetic parent proton populations at discrete energies of $E \in \{1, 10, 40, 70, 100\}$ keV.
 523 Above 100 keV, the value of both the charge exchange cross section as well as the am-
 524 bient energetic proton fluxes at each moon decay rapidly (Cooper et al., 2001; Paran-
 525 icas et al., 2002; Lindsay & Stebbings, 2005). Thus, this energy range covers the segment
 526 of the energetic ion distribution near the moons that makes the strongest contributions
 527 to the observable ENA flux. The gyroradii r_g of protons in the considered energy regime
 528 are provided in Table 2.

Proton gyroradii $r_g[R]$					
Moon	Callisto		Europa		
Position w.r.t. plasma sheet	Center	Below	Center	Below	
<u>Energy</u>					
Thermal	0.21	0.02	$1.63 \cdot 10^{-3}$	$1.53 \cdot 10^{-3}$	
1 keV	0.47	0.05	0.01	0.01	
10 keV	1.50	0.16	0.02	0.02	
40 keV	2.99	0.32	0.05	0.04	
70 keV	3.97	0.43	0.06	0.06	
100 keV	4.74	0.51	0.07	0.07	

Table 2. Energetic proton gyroradii in units of respective moon radius R ($R = R_E$ at Europa and $R = R_C$ at Callisto). Values are computed assuming a pitch angle of $\alpha = 90^\circ$. Gyroradii of thermal protons traveling with bulk velocity $|\mathbf{u}_0|$ are included for comparison, where the kinetic energy is given by $m_p |\mathbf{u}_0|^2/2$. This corresponds to 52.2 eV at Europa and 192.4 eV at Callisto.

The setup of our ENA generation model is displayed in Figure 1, using Callisto as an example. Parent ions are launched from the nodes of a starting grid that is attached to the outer faces of the AIKEF simulation domain, illustrated by the white lattice in Figure 1. This ensures that even for the highest proton energies considered (100 keV) there is still a distance of at least $2.5r_g$ between any plane of the starting grid and the Callisto (see Table 2). Due to the 10 – 100 times stronger magnetic field at Europa, the distance between the moon and the faces of the starting grid (in units of proton gyro-radii) is even larger. The directions from which energetic protons can impinge upon the moon’s atmosphere are dependent upon the orientation of \mathbf{B}_0 . Velocities $\sqrt{2E/m_p}$ (where m_p is proton mass) of protons within our considered energy regime range from approximately 440 km/s to 4,400 km/s. As such, the corotation drift velocity (on the order of 100 km/s) provides only a minor contribution to the net velocity, and particles with pitch angles near 0° and 180° will move along magnetic field lines much faster than their drift in the $+x$ direction.

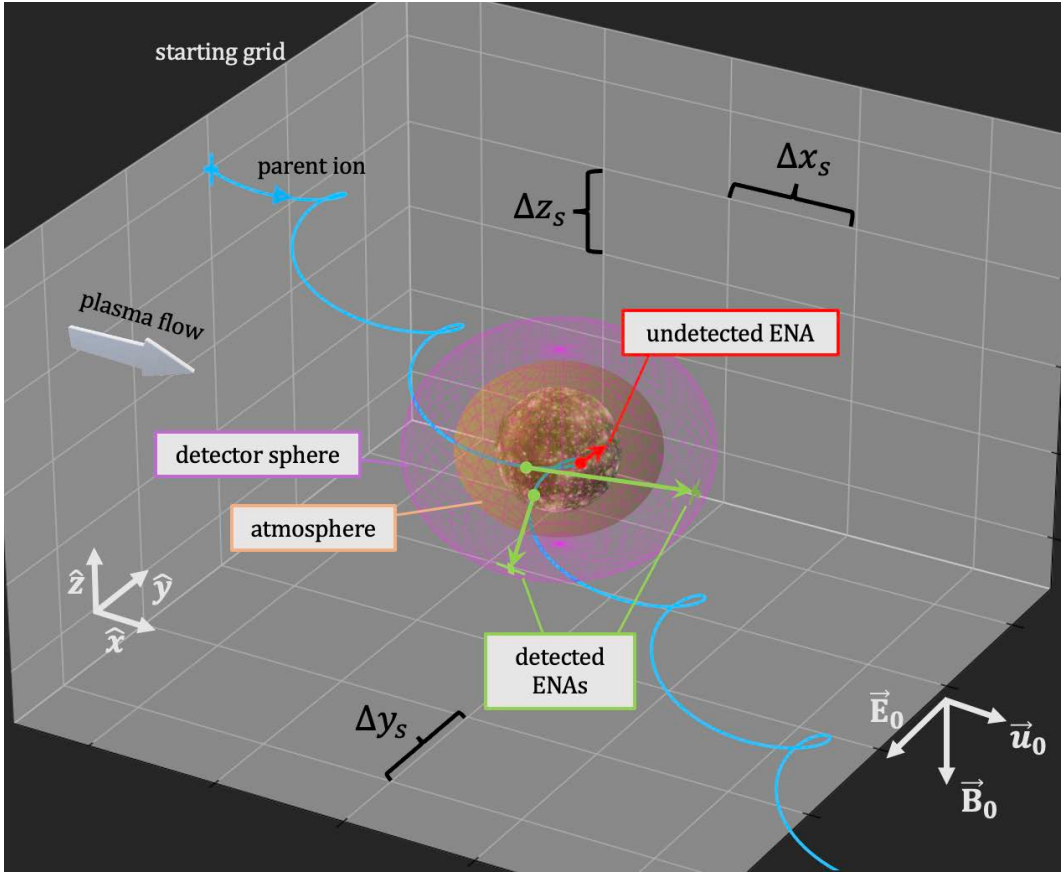


Figure 1. A depiction of the ENA generation model at Callisto, for the case with the moon located at the center of the Jovian plasma sheet. The downstream, northern, and Jupiter-averted faces of the starting grid cuboid (white mesh on grey background) are omitted to allow viewing into the model domain, and the radius of the detector (purple sphere around the atmosphere) is enlarged for clarity. At Callisto, a step size of $\Delta x_s = \Delta y_s = \Delta z_s = 0.04R_C$ is used in each of the six planes of the starting grid. A single parent ion trajectory (light blue) is displayed, initiated at a grid node on the upstream face of the starting grid. This parent ion remains within Callisto's atmosphere (orange shaded region) for nearly an entire gyration and generates ENAs. ENAs that collide with the moon (red) are not detected, but ENAs with a velocity vector bearing away from the moon (green) are observed by the spherical model detector that encompasses the moon's entire atmosphere. The figure is not to scale.

543
544
545
546

Energetic protons bouncing between mirror points in the Jovian magnetosphere can generate ENAs as they enter Europa's or Callisto's interaction region and interact with the atmosphere. To incorporate such particles in our model scenario, we include faces of the starting grid at the northern ($z > 0$) and southern ($z < 0$) as well as the

547 Jupiter-facing ($y > 0$) and Jupiter-averted ($y < 0$) boundaries of the AIKEF domain.
 548 In general, parent ions launched from the northern/southern and Jupiter-facing/Jupiter-
 549 averted faces of the starting grid can potentially reach the moon's atmosphere and pro-
 550 duce ENAs whenever the background field \mathbf{B}_0 possesses a component orthogonal to the
 551 respective face. Energetic parent ions are also launched from the downstream face ($x >$
 552 0) of the starting grid. Note that protons initiated at the downstream face can reach ei-
 553 ther moon by traveling along the magnetic field lines only if the background field pos-
 554 sseses a component normal to that face. Otherwise, the corotation drift will carry these
 555 protons away from the moon and they cannot travel towards upstream. We refer the reader
 556 to section 2.3 of Tippens et al. (2022) for further discussion of the starting grid and how
 557 it captures bouncing protons capable of interacting with either moon's atmosphere. In
 558 Figure 1, the upstream, Jupiter-facing and southern planes of the starting grid are de-
 559 picted.

560 Each face of the starting grid is populated with nodes that are equally spaced along
 561 the x , y , and z directions, forming squares of area dA . At each of these nodes we launch
 562 energetic protons of a given initial energy, a sample of which is indicated by the inter-
 563 sections of the white lines in Figure 1. If energetic proton gyroradii greatly exceed the
 564 moon's atmospheric scale height, these ions can only complete partial gyrations within
 565 the moon's atmosphere when initialized at a certain phase of their gyration. At Europa,
 566 energetic proton gyroradii are smaller than or comparable to the atmospheric scale height
 567 $h_{s,E}$ (see Table 2). For this reason, parent protons can complete multiple gyrations within
 568 the atmosphere (and produce ENAs), irrespective of the phase of its gyration when ini-
 569 tialized on the starting grid. However, at Callisto, energetic proton gyroradii range from
 570 about $0.02R_C$ to $4.7R_C$ within the considered energy range (see Table 2). Thus, depend-
 571 ing on their initial gyrophase and the resolution of the starting grid, a large fraction of
 572 the newly initiated protons may miss Callisto's atmosphere entirely, even if the trajec-
 573 tories of their guiding centers come close to the moon. We found that this may lead to
 574 "blurring" of our modeled ENA emission maps. In order to obtain a sufficiently smooth
 575 ENA emission pattern, the starting grid at Callisto therefore requires a *higher* spatial
 576 resolution than at Europa where energetic ions can complete many gyrations within the
 577 atmosphere.

578 The length scales of Callisto's interaction region are comparable to those at Titan,
 579 in particular regarding the size of ion gyroradii relative to the diameter of the moon and

the spatial extension of the electromagnetic field perturbations (in units of the respective moon's radius), see, e.g., Liuzzo et al. (2015) and Simon et al. (2015). Accordingly, at Callisto we define a separation of $0.04R_C$ between adjacent nodes of the starting grid in each direction, similar to Wulms et al. (2010), Kabanovic et al. (2018), and Tippens et al. (2022). Since the starting grid of the ENA generation model is attached to the outer faces of the AIKEF domain, this yields $(30R_C/0.04R_C)^2 = 562,500$ unique positions of initialized ions on each of the 6 faces at Callisto. At Europa, a coarser starting grid resolution of $0.15R_E$ is sufficient for a smooth distribution of the modeled ENA fluxes.

At each starting grid node, we initialize a population of parent protons whose velocity vectors isotropically cover a sphere in velocity space. The velocity sphere is discretized in zenith and azimuth using polar coordinates ϕ_v and θ_v , with resolution on the velocity sphere $\Delta\theta_v = \Delta\phi_v = 5^\circ$. We initialize each particle with a velocity magnitude $v_0 = \sqrt{\frac{2E}{m_p}}$ such that

$$\dot{\mathbf{r}}(t=0) = (v_0 \sin \theta_v \cos \phi_v, v_0 \sin \theta_v \sin \phi_v, v_0 \cos \theta_v) \quad , \quad (6)$$

where \mathbf{r} is the position of the particle.

Each newly initialized parent ion is “weighted” with a flux value derived from angularly resolved proton spectral energy distributions $\tilde{I}(E)$ observed by the Galileo Energetic Particle Detector (EPD) in the uniform plasma environment outside of each moon's interaction region. At Europa, we employ energetic proton distributions $\tilde{I}(E)$ taken during the close Galileo flybys at multiple distances to the center of the Jovian plasma sheet (e.g., Cooper et al., 2001; Paranicas et al., 2002, 2009). For the center of the sheet, we use the fit provided for the observed EPD spectrum from E12. The E12 flyby occurred at a distance of only $d \approx 0.1R_J$ (see equation (2)) to the center of the sheet. For model setups with Europa located at maximum distance below Jupiter's plasma sheet, we implement the fit to the ambient $\tilde{I}(E)$ from the E26 flyby which took place at a distance of $d \approx 1.0R_J$ below the sheet.

When Callisto is at the center of the Jovian plasma sheet, we employ the fit to EPD data obtained from a Galileo sheet crossing near the moon's orbital distance (Mauk et al., 2004, see their Table 1, label G8 PS/A). Callisto was not proximal to the spacecraft during these observations, so this $\tilde{I}(E)$ spectrum provides an adequate representation of the ambient magnetospheric proton flux. Callisto's M shell value (e.g., Szalay et al., 2017; Liuzzo et al., 2019b, 2022) changes by almost a factor of 3 going from the center

of Jupiter's plasma sheet ($M = 26.3$) to the maximum distance below ($M > 70$). The intensity $\tilde{I}(E)$ of the ambient energetic proton flux has been suggested to fall by about an order of magnitude moving from the center to maximum distance from the center of the Jovian plasma sheet (Paranicas et al., 2018; Kollmann et al., 2018; Liuzzo et al., 2022). When Callisto is situated at maximum distance below Jupiter's plasma sheet, we proceed analogous to Liuzzo et al. (2022) and use the energetic proton distribution observed at the center (Mauk et al., 2004), but downscaled by a factor of 10 at all energies.

The energy spectrum $\tilde{I}(E)$ represents the number flux of particles at a certain energy per steradian (e.g., Paranicas et al., 2009). In the classical regime, this quantity is related to the distribution function f of the proton population with speed $v = |\dot{\mathbf{r}}|$ in phase space by

$$\tilde{I}(E) = \frac{v^2}{m_p} f = \frac{2E}{m_p^2} f , \quad (7)$$

see, e.g., Kollmann et al. (2018). The pitch angle distribution (PAD) included in our model was determined from in-situ spacecraft observations of energetic particle fluxes near Europa and Callisto. The observed particle fluxes $\tilde{I}(E)$ and the PAD can be related to the total energetic proton flux $I(E)$, integrated across all viewing directions, through

$$\tilde{I}(E) = \frac{I(E) p(\alpha(\theta_v, \phi_v))}{\int_0^{2\pi} \int_0^\pi p(\alpha(\theta_v, \phi_v)) d\Omega_v} , \quad (8)$$

where $p(\alpha(\theta_v, \phi_v))$ is the PAD, α denotes the pitch angle, and $d\Omega_v \equiv \sin \theta_v d\theta_v d\phi_v$ (see also Addison et al., 2021). The initial weight of each proton macroparticle is given by $J = \tilde{I}(E)d\Omega_v = \tilde{I}(E) \sin \theta_v \Delta\theta_v \Delta\phi_v$ for initial energy E when launched at the starting grid. The angular factor $\sin \theta_v$ takes into account that the velocity vectors of newly initiated protons are closer to each other near the poles of the velocity sphere than when near its equator.

Galileo observations of the ambient proton fluxes at Callisto's orbit suggest an isotropic PAD in the energy range we consider (Paranicas et al., 2002; Mauk et al., 2004). In addition, Juno observations revealed a nearly isotropic proton PAD near Callisto at energies of 117 keV, i.e., slightly above our considered energy range (Shen et al., 2022). A recent survey of Juno data (Sarkango et al., 2023) suggests that the proton PAD inward of Callisto's orbit may have a nonuniform shape at energies below 200 keV; i.e., the proton fluxes minimize around pitch angles of $\alpha \approx 90^\circ$ and maximize at $\alpha = 0^\circ$ and $\alpha = 180^\circ$. For our study, we treat the PAD near Callisto as isotropic. We do investigate the influence of anisotropies in the PAD on ENA emissions at Europa (see below). However,

we expect the effect of such anisotropies to be very similar at both moons. Using an isotropic PAD for all Callisto runs of our ENA generation model, p is unity and equation (8) becomes

$$\tilde{I}(E) = \frac{I(E)}{\int_0^{2\pi} \int_0^\pi d\Omega_v} = \frac{I(E)}{4\pi} . \quad (9)$$

Galileo EPD spectra obtained farther inward within the Jovian magnetosphere demonstrate approximately uniform fluxes across all pitch angles in Europa's energetic proton environment (Mauk et al., 2004). Notwithstanding this, deviations from isotropy have been detected at Europa for certain proton energies: for instance, Galileo observations in the energy range $80 \leq E \leq 220$ keV show a depletion in proton flux for pitch angles near 90° (Lagg et al., 2003). Kollmann et al. (2016) identified a persistent minimum in proton flux around $\alpha = 70^\circ$ at energies of 130 keV. Most recently, the Juno spacecraft found evidence of an anisotropic proton PAD near Europa at $E \approx 117$ keV: the observed proton flux around $\alpha = 90^\circ$ is approximately a factor of two lower than when $\alpha = 0^\circ$ or $\alpha = 180^\circ$ (Shen et al., 2022). Sarkango et al. (2023) demonstrated the presence of a similar anisotropy in the PAD for the energy range analyzed in our study ($E \leq 100$ keV; see their figure 1(a)).

For most applications of the ENA model at Europa, we follow Mauk et al. (2004) and treat the PAD of the ambient proton population as isotropic. However, to constrain the influence of this assumption on the ENA emission morphology, we also consider a test case for Europa at the center of the plasma sheet with newly launched parent ions weighted according to a PAD that assigns more flux to the population traveling along the magnetic field than that propagating normal to it. Building upon the findings of Shen et al. (2022) and Sarkango et al. (2023), we assume (across all considered energies) that the energetic proton flux reflects the observations by Juno: particularly, the flux perpendicular to the magnetic field is about 50% smaller than it is for pitch angles of $\alpha = 0^\circ$ or 180° . For \mathbf{B}_0 antiparallel to the z axis (as is the case in our setup for Europa at the center of the plasma sheet) we can model this PAD with the form

$$p(\alpha(\theta_v, \phi_v)) = 1 - \frac{\sin \alpha}{2} = 1 - \frac{\sin \theta_v}{2} . \quad (10)$$

The factor in the denominator of equation (8) is given by

$$\int_0^{2\pi} \int_0^\pi p(\alpha(\theta_v, \phi_v)) d\Omega_v = \pi(4 - \frac{\pi}{2}) \approx 7.632 . \quad (11)$$

668 This yields an initial macroparticle weight upon launch equal to

$$J = \frac{I(E)}{\pi(4 - \frac{\pi}{2})} \left(1 - \frac{\sin \theta_v}{2}\right) \sin \theta_v \Delta \theta_v \Delta \phi_v . \quad (12)$$

669 When a newly launched proton macroparticle travels through a cross section dA
 670 on the starting grid (depicted by the white grid lines in Figure 1), it represents a par-
 671 ticle “passage rate” (in units of 1/s) of

$$dF = f \dot{\mathbf{r}} \cdot \hat{\mathbf{n}} dA d^3v = f \dot{\mathbf{r}} \cdot \hat{\mathbf{n}} dA v^2 \sin \theta_v d\theta_v d\phi_v , \quad (13)$$

672 where $\hat{\mathbf{n}}$ is the unit vector normal to the grid element (see also section 3 of Wulms et al.,
 673 2010). The dependence of the value dF on the cell size dA of the starting grid is impor-
 674 tant to bear in mind when comparing model results obtained with *different* starting grid
 675 resolutions. Consider, e.g., two ENA model runs carried out for Europa under identi-
 676 cal ambient magnetospheric conditions (i.e., the ambient distribution function f in equa-
 677 tion (13) is the *same* in both cases). However, the cell size dA_1 of the starting grid in
 678 the first scenario is larger than the cell size dA_2 of the second scenario ($dA_1 > dA_2$).
 679 Thus, the number of proton macroparticles launched within the *larger* cell area dA_1 is
 680 elevated by a factor of dA_1/dA_2 in the second scenario compared to the first. This im-
 681 plies that in the *second* scenario, the amount of differential flux J_2 (in units of $[cm^2 sr keV s]^{-1}$)
 682 initiated in the *larger* cell area dA_1 (covered by multiple cells of area dA_2) is also increased,
 683 compared to scenario 1, by the same factor of dA_1/dA_2 :

$$J_2|_{dA_1} = J_1|_{dA_1} \frac{dA_1}{dA_2} . \quad (14)$$

684 However, the passage rate dF (in units of 1/s) through area dA_1 needs to be *equal* in
 685 both model scenarios to ensure a valid comparison. Merely using equation (14) and $J \propto$
 686 $\tilde{I}(E) \propto f$ (see equation (7)) would yield

$$dF_2|_{dA_1} = dF_1|_{dA_1} \left(\frac{dA_1}{dA_2} \right) . \quad (15)$$

687 Thus, the rate dF_2 in scenario 2 would be artificially enhanced compared to the rate dF_1
 688 in scenario 1, solely because of the smaller size of the cells on the starting grid in sce-
 689 nario 2. To account for this artificial increase in rate dF , the modeled rate dF_2 in sce-
 690 nario 2 needs to be rescaled according to

$$d\tilde{F}_2|_{dA_1} = dF_2|_{dA_1} \frac{dA_2}{dA_1} . \quad (16)$$

691 Similar to the approach of Tippens et al. (2022), we propagate energetic proton macropar-
 692 ticles through uniform fields or the perturbed electromagnetic fields calculated by AIKEF

(see the blue trajectory in Figure 1). In the case of perturbed fields, the electromagnetic field vectors at the position of the macroparticle are determined from the eight adjacent nodes of the AIKEF simulation grid through trilinear interpolation. The equation of motion for a proton (charge e) at position \mathbf{r} in electric field \mathbf{E} and magnetic field \mathbf{B} is given by

$$\ddot{\mathbf{r}} = \frac{e}{m_p} (\mathbf{E} + \dot{\mathbf{r}} \times \mathbf{B}) . \quad (17)$$

The trajectory of each proton macroparticle is evolved through space with a Runge-Kutta scheme of fourth order. Since the relativistic Lorentz factor for protons even at the highest energy considered ($E = 100$ keV) does not exceed 0.1% deviation from unity, a relativistic treatment of parent ion dynamics is not necessary.

If the particle's trajectory crosses one of the outer boundaries of the model domain enclosed by the starting grid, the trajectory is allowed to evolve over $2 r_g$ (see Table 2) beyond the boundary before it is removed from the simulation (akin to Regoli et al. (2016) and Tippens et al. (2022)): such particles can *not* return to the moon and produce ENAs. Energetic protons exiting the domain are not immediately removed since they may still enter Europa's and Callisto's atmospheres later in time. The uniform magnetospheric background field \mathbf{B}_0 and the corresponding convective electric field $\mathbf{E}_0 = -\mathbf{u}_0 \times \mathbf{B}_0$ are used to evolve particle trajectories outside of the AIKEF domain. An adaptive timestep is implemented to solve equation (17) dependent both on proximity to the moon as well as the gyroperiod $T_p = \frac{2\pi m_p}{e|\mathbf{B}|}$ in the local magnetic field \mathbf{B} . The timestep Δt in the energetic particle tracer is given by

$$\Delta t(\mathbf{r}) = \begin{cases} \frac{T_p}{80} & |\mathbf{r}| > 4R \\ \frac{T_p}{160} & |\mathbf{r}| \leq 4R \end{cases} , \quad (18)$$

where R is again the radius of the respective moon. If the local magnetic field strength $|\mathbf{B}|$ is less than the background field magnitude $|\mathbf{B}_0|$, then the gyroperiod in the background field is used as a baseline for Δt . In other words, the timestep at either level of resolution is not permitted to grow above what it would be in the uniform magnetospheric background field.

During its evolution after being launched, an energetic proton undergoes acceleration by the electromagnetic fields. To calculate the modified flux that it represents when entering Europa's or Callisto's atmosphere, we need to combine equation (7) with Liouville's theorem. By equating the distribution function at initialization on the starting grid to its value at the top of the atmosphere, we can derive a relationship between

723 the differential particle fluxes at these locations. Namely, if the macroparticle begins its
 724 evolution at the starting grid with velocity $\dot{\mathbf{r}}_1$ and weight J_1 , and reaches the top of the
 725 moon's atmosphere with a velocity $\dot{\mathbf{r}}_2$, the modified weight J_2 becomes

$$J_2 = \left(\frac{|\dot{\mathbf{r}}_2|}{|\dot{\mathbf{r}}_1|} \right)^2 J_1 \quad . \quad (19)$$

726 A similar rescaling of the flux is done whenever a proton exits and subsequently re-enters
 727 Callisto's or Europa's atmosphere, as displayed by the particle trajectory in Figure 1.

728 Apart from charge exchange interactions inside of a moon's atmosphere that gen-
 729 erate ENAs, scattering through wave-particle interactions by, e.g., ion cyclotron waves
 730 (Nénon et al., 2018) and Whistler-mode waves (Shprits et al., 2018) may cause localized
 731 phase space depletions that prevent the conservation of the distribution function. So far,
 732 the presence of such waves near Callisto has neither been conclusively established through
 733 observations nor modeling results. In contrast to Callisto's environment, the model of
 734 Desai et al. (2017) revealed that pick-up of ionospheric ions causes ion cyclotron waves
 735 to develop within $3R_E$ of Europa's wakeside hemisphere, consistent with those observed
 736 during Galileo flybys E11 and E15 (Volwerk et al., 2001). However, data from the few
 737 Galileo flybys of Europa provide only limited information on the locations of regions with
 738 strong wave activity. Besides, Shprits et al. (2018) emphasize that these regions are prob-
 739 ably highly localized. Therefore, we still consider Liouville's theorem to be valid in good
 740 approximation outside of Europa's and Callisto's atmospheres, similar to the particle trac-
 741 ing models of, e.g., Addison et al. (2021, 2022), and Liuzzo et al. (2022).

742 We propagate parent protons from the starting grid to the top of each moon's at-
 743 mosphere. The atmospheric profiles in the ENA generation model are identical to the
 744 atmospheric profiles used to calculate the electromagnetic field configurations with AIKEF
 745 at each moon (see section 2.1). In Figure 1, the proton enters the atmosphere when the
 746 blue trajectory intersects the region shaded in orange. At an altitude of one moon ra-
 747 dius above the surface, the number density of both Callisto's and Europa's atmosphere
 748 in our model has fallen by 5 orders of magnitude relative to the surface density. We there-
 749 fore do not consider ENA generation beyond an altitude of R above each moon's sur-
 750 face. At altitudes greater than R , the atmospheric profiles in our model contain only 0.002%
 751 of the integrated atmospheric number density at Europa, and 0.3% at Callisto. For this
 752 reason, we expect the ENA production at altitudes greater than R to generate only a

753 very minor contribution to the emitted ENA flux, concordant with the findings of Tippens
 754 et al. (2022) at Titan.

755 At Callisto, the column density of the CO₂ component is approximately a factor
 756 of 25 lower than that of O₂ (see also Liuzzo et al., 2015). Therefore, ENA emissions from
 757 the CO₂ constituent are expected to be weak compared to those emitted through charge
 758 exchange with the O₂ profile. Further, cross sections for charge exchange between pro-
 759 tons and CO₂ molecules have been measured only for energies above 100 keV (Toburen
 760 et al., 1968; Belkić, 2021). Ergo, we do not consider ENA generation through charge ex-
 761 change with CO₂ at Callisto. However, the CO₂ component of Callisto's atmosphere is
 762 still present in the AIKEF runs where –due to its large mass– it contributes to flow de-
 763 celeration and field line draping (Liuzzo et al., 2015). Roth, Alday, et al. (2017) ascer-
 764 tained the presence of a dilute atomic hydrogen corona at Callisto. However, these au-
 765 thors estimated a column density of $(6\text{--}12) \cdot 10^{11} \text{ cm}^{-2}$, which is at least three orders
 766 of magnitude less than that of the molecular oxygen profile. Therefore, this constituent
 767 is included neither in AIKEF nor in our ENA generation model at Callisto. In addition,
 768 a recent modeling study suggested the presence of an appreciable molecular hydrogen
 769 component in Callisto's atmosphere (Carberry Mogan et al., 2022). This component is
 770 not included in the current model setup, and we will elaborate on its potential impact
 771 on the ENA emissions in section 3.5.

772 Whenever a proton macroparticle enters Callisto's or Europa's atmosphere, it con-
 773 tinuously interacts with the neutral gas through charge exchange, analogous to Wulms
 774 et al. (2010), Kabanovic et al. (2018), and Tippens et al. (2022). During a timestep within
 775 the atmosphere, a macroparticle moves along a path element ds with length $ds = |ds|$.
 776 The loss of energetic proton weight dJ within the atmosphere is determined by the at-
 777 tenuation equation (Wulms et al., 2010; Kabanovic et al., 2018; Tippens et al., 2022),

$$\frac{dJ}{ds} = -\sigma(E) n_n(\mathbf{r}) J \quad , \quad (20)$$

778 where $n_n(\mathbf{r})$ is the neutral density evaluated at the midpoint of the spatial step ds . The
 779 energy-dependent cross section $\sigma(E)$ for the ENA-generating interaction H⁺+O₂ →
 780 H + O₂⁺ (at Europa and Callisto) is given in Table 1 of Lindsay and Stebbings (2005)
 781 and displayed in Figure 2 (green). For the H₂O charge exchange interaction at Europa,
 782 i.e., H⁺ + H₂O → H + H₂O⁺, the cross section can be found in Table 4 of Wedlund
 783 et al. (2019) and is also displayed in Figure 2 (blue).

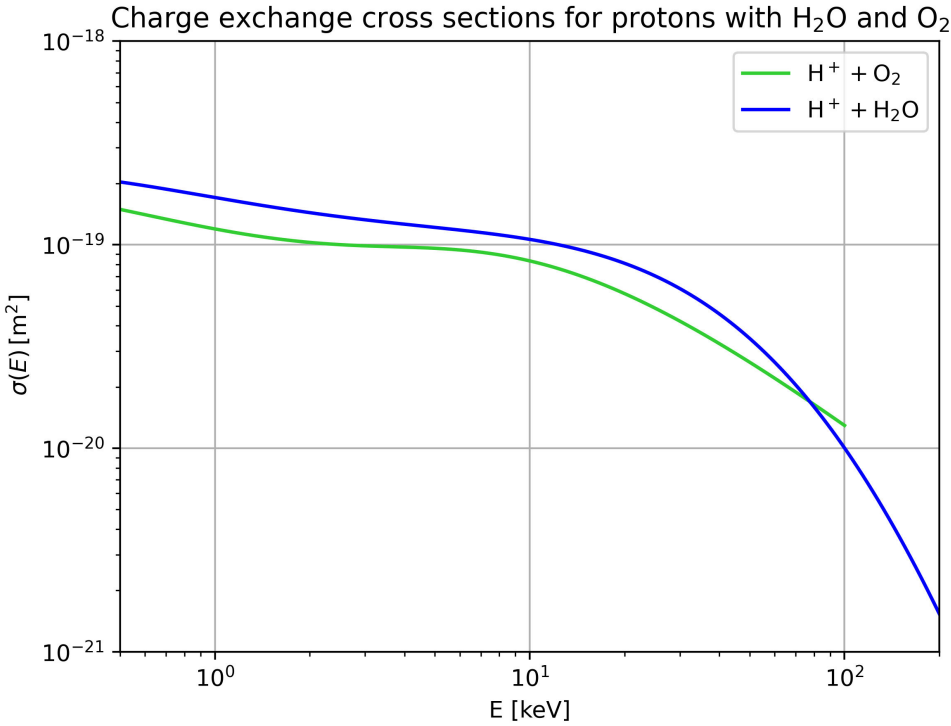


Figure 2. Charge exchange cross sections for protons with molecular oxygen and water vapor, given by Lindsay and Stebbings (2005) and Wedlund et al. (2019), respectively. The cross section for $H^+ + O_2 \rightarrow H + O_2^+$ is only available for energies $0.05 \text{ keV} \leq E \leq 100 \text{ keV}$; i.e., covering the energy range that we analyze in our study.

In addition to protons, an abundance of singly charged atomic sulfur and oxygen
 (as well as multiply charged ions of the same species) is persistently observed in the am-
 bient plasma at Europa and Callisto (e.g., Cooper et al., 2001; Mauk et al., 2004; Nénon
 & André, 2019; Clark et al., 2020). These energetic ion species are not included in our
 ENA generation model for two reasons. First, charge exchange cross sections through-
 out the energy range $1 \text{ keV} \leq E \leq 100 \text{ keV}$ are not available in the literature. For in-
 stance, cross sections for charge exchange between singly ionized atomic oxygen and neu-
 tral molecular oxygen have been determined experimentally only for energies between
 1 and 5 keV (Lindsay & Stebbings, 2005), and at three discrete higher energies (Loand
 & Tite, 1969). Nénon and André (2019) were able to use observations of Europa's neu-
 tral torus to estimate that the ratio of charge exchange cross sections between sulfur ions
 and atomic oxygen or molecular hydrogen is less than 1.5. Nevertheless, no profiles of

796 the energy dependent cross sections $\sigma(E)$ were determined, in particular not for the en-
 797 ergy range relevant to our study.

798 Second, the distribution of charge states within the energetic heavy ion populations
 799 near Europa and Callisto (i.e, the number ratio between singly and multiply charged sul-
 800 fur or oxygen ions) is still under debate (e.g., Clark et al. (2016, 2020) and references
 801 therein). The measured heavy ion energy spectra (e.g., Paranicas et al. (2009)) do not
 802 discriminate between singly and multiply charged ions. Since, e.g., O^{2+} or S^{3+} ions are
 803 not expected to be neutralized on the small length scales of Europa’s or Callisto’s local
 804 interaction regions (e.g., Nénon and André (2019)), only a certain fraction of the inci-
 805 dent oxygen/sulfur ion populations would actually be able to generate ENAs near these
 806 moons. Hence, the observed heavy ion energy spectrograms would have to be “down-
 807 scaled” to consider only the ENA-generating, singly charged portion of the incident ion
 808 population (with the ratio of singly and multiply charged ions scarcely constrained). For
 809 these two reasons, we defer the analysis of ENA-generation by heavy ions ions to a fu-
 810 ture investigation. Including the heavy ion species would mainly enhance the intensity
 811 of ENA emissions and their detectability by spacecraft.

812 While inside the atmosphere, each parent ion produces a single ENA macroparti-
 813 cle during each time step. Equation (20) is used to convert part of the flux J carried by
 814 the parent ion macroparticle into ENA flux. During each timestep that an energetic par-
 815 ent ion spends in Europa’s or Callisto’s atmosphere, the ENA generation model records
 816 the position and velocity coordinates of the macroparticle as its weight is attenuated by
 817 dJ , as well as the flux $Y = |dJ|$ of the newly generated ENA macroparticle (see also
 818 Wulms et al., 2010; Kabanovic et al., 2018; Tippens et al., 2022). Since the considered
 819 near-resonant charge exchange interactions are highly forward scattered (Dandouras &
 820 Amsif, 1999; Lindsay & Stebbings, 2005), the velocity vector of each newly-emitted ENA
 821 macroparticle is identical to the parent proton’s velocity the moment the ENA is cre-
 822 ated. Starting from the position of the parent ion at the moment of charge exchange,
 823 the rectilinear trajectory of each ENA is traced until it encounters one of two fates: ei-
 824 ther it intersects the moon’s surface and it is deleted from the simulation (red tra-
 825 jectory in figure 1), or it leads away from the moon and the ENA would be observable out-
 826 side the atmosphere (green trajectories in figure 1). Our study focuses on the latter case;
 827 i.e., on the detectability of ENA emissions that emanate from Callisto’s and Europa’s
 828 atmospheres.

The detectable ENA flux is processed into a flux map through the surface of a spherical detector (centered at the moon) at altitude $h = R$ enclosing the Callisto's or Europa's entire atmosphere, thereby capturing all ENAs traveling away from the moon. Due to the inherent truncation of observable ENA flux by the finite field of view, an actual (point-like) spacecraft detector captures only a tiny fraction of the emitted ENA population. To preserve the entirety of the physics contained in the ENA pattern emitted from the moon's atmosphere, we employ a detector geometry that encapsulates the entire ENA generation region. The same approach was applied by Tippens et al. (2022) to investigate the global morphology of ENA emissions at Titan. Incorporation of a realistic, point-like detector geometry is a goal for future investigation, e.g., after the specifications of the ENA detector aboard JUICE have been made available. The spherical detector surrounding each moon in our model is binned into longitude and latitude segments $3^\circ \times 3^\circ$ in extension and the total flux associated with all ENAs intersecting each bin is calculated. To evaluate the dependence of the ENA emission morphology on the initial energy of the parent protons, ENA emission maps have been calculated separately for each of the five starting energies studied.

We do not consider subsequent reionization and reneutralization of ENAs, as done, e.g., for Titan by Garnier et al. (2008). Including these effects may rather be the subject of a future study. Sputtering of an icy moon's surface by impinging energetic ions can also result in ENA emissions, as was modeled at Ganymede by Pontoni et al. (2022). Our study focuses only on ENA generation from interactions with Callisto's and Europa's atmospheres. Taking into account ENAs emitted from the surface as well is beyond the scope of this study, as it would require a conceptually distinct modeling approach. However, this investigation allows follow-up studies to *isolate* the contribution of ENAs emitted from their atmosphere, compared to those generated at these moons' surfaces.

3 Model Results and Discussion

3.1 Perturbed Electromagnetic Fields At Callisto and Europa

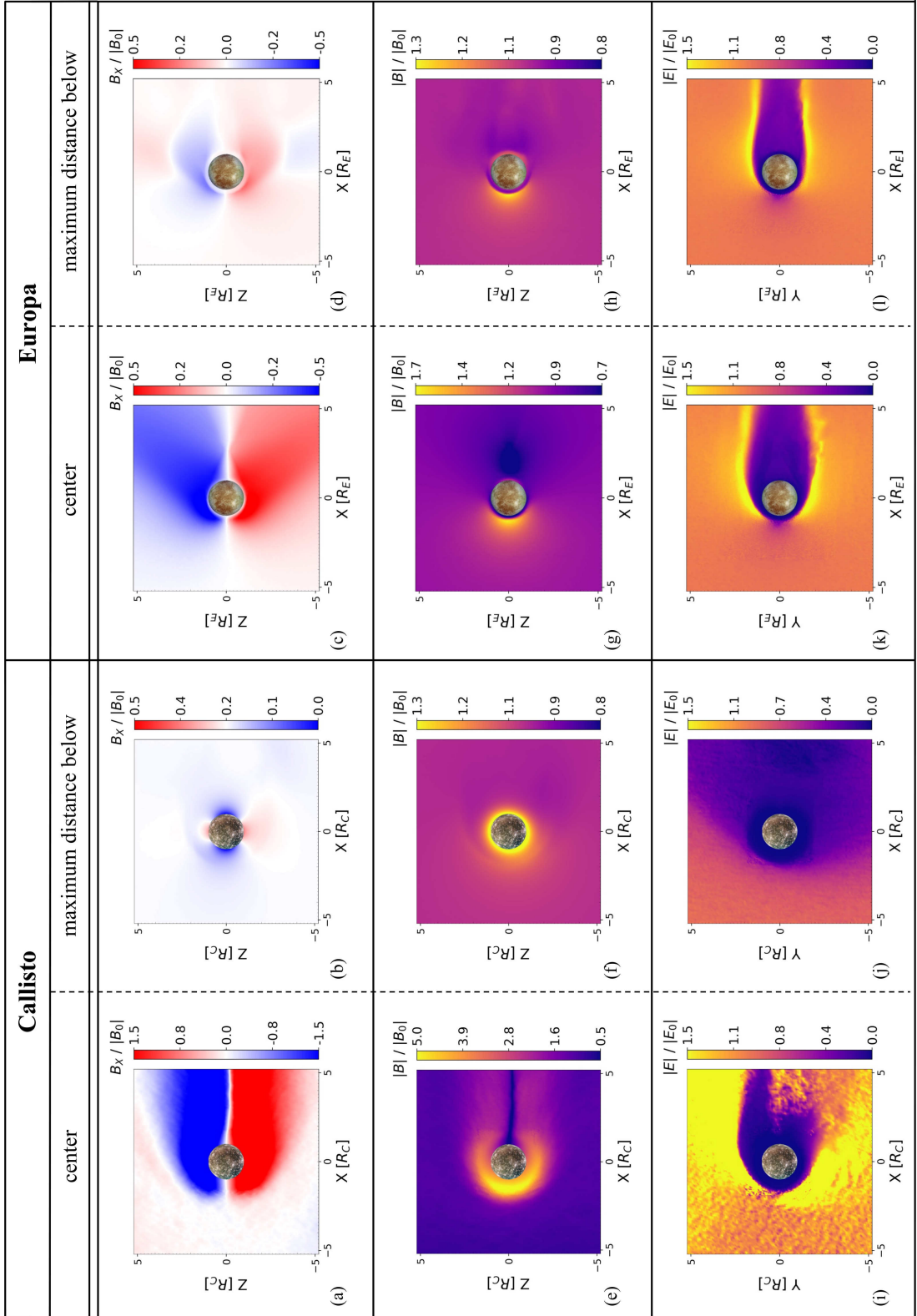


Figure 3. The perturbed electromagnetic environments around Callisto (left two columns) and Europa (right two columns) in planes containing the center of the moon, computed using the AIKEF hybrid model. Panels (a)-(d) show the flow-aligned component (B_x) of the magnetic field while panels (e)-(h) show the magnetic field magnitude ($|B|$) near the respective moon, both in the $y=0$ plane. Panels (i)-(l) show the magnitude of the electric field ($|E|$) in the $z=0$ plane. When either moon is located at the center of the Jovian plasma sheet (when they are exposed to a purely southward magnetospheric background field), the convective electric field \mathbf{E}_0 points in $(-y)$ direction and is therefore parallel to the $z = 0$ plane. Each quantity is plotted on a scale normalized to the respective background field value (i.e., $|B_0|$ for the top and middle row, $|E_0| = |\mathbf{u}_0 \times \mathbf{B}_0|$ for the bottom row, see Table 1). Within each column, the left sub-column corresponds to the respective moon at the center of the Jovian plasma sheet, and the right sub-column corresponds to the moon at its maximum distance below the plasma sheet. To ensure best possible visibility of the field perturbations, the ranges of the color bars are different between panels (a) and (b) as well as panels (e), (f), (g) and (h).

Figures 3 and 4 depict the structure of the perturbed electromagnetic environment in the vicinity of Europa and Callisto for each hybrid model configuration. The left two columns of Figure 3 correspond to Callisto at the center and at maximum distance below the center of the Jovian magnetospheric plasma sheet, respectively. The right two columns follow identical organization for Europa. The first row (panels 3(a) – 3(d)) and second row (panels 3(e) – 3(h)) show the flow-aligned magnetic field component B_x and field strength $|\mathbf{B}|$ in the $y = 0$ plane, respectively. The third row (panels 3(i) - 3(l)) displays the magnitude of the electric field $|\mathbf{E}|$ in the $z = 0$ plane. All quantities in Figure 3 are normalized to the respective upstream value, i.e., $|\mathbf{B}_0|$ for the top two rows and $|\mathbf{E}_0|$ for the bottom row. When either moon is at the center of the Jovian plasma sheet, the $y = 0$ plane contains the background magnetic field vector \mathbf{B}_0 , and the $z = 0$ plane contains the background convective electric field vector \mathbf{E}_0 . When Europa is located at its maximum distance below the Jovian plasma sheet, the background magnetic field is rotated against the $y = 0$ plane (toward Jupiter) by 28.5° , and the background electric field is correspondingly rotated by the same angle against the $z = 0$ plane. Analogously, when Callisto is located below the plasma sheet, the background magnetic field is rotated by 72.5° against the $y = 0$ plane toward Jupiter (see Table 1). For this case, a depiction of plasma and electromagnetic field quantities in planes containing the strongly inclined background fields is given in Figure 1 of Liuzzo et al. (2022). Figure 4 shows results for Europa when an H₂O atmospheric component is included in addition to molecular oxygen. We include in panels 4(a) and 4(b) the H₂O⁺ number density in the $z = 0$ and $y = 0$ planes, respectively. The bottom row of Figure 4 displays the electromagnetic field quantities.

Extensive discussions of the perturbed electromagnetic environment within the framework of AIKEF are given by Arnold et al. (2019), Arnold, Liuzzo, and Simon (2020), Arnold, Simon, and Liuzzo (2020), Breer et al. (2019), and Addison et al. (2021, 2022) for Europa, and by Liuzzo et al. (2015, 2016, 2017, 2018, 2019a, 2019b, 2022) for Callisto. Therefore, we provide only a brief discussion of the features relevant to our analysis of ENA emissions. For a more detailed discussion, the reader is referred to any of our preceding publications using the same model.

We begin our analysis with the case of either moon at the center of the Jovian plasma sheet, i.e., the two left columns of Figure 3. At both Europa and Callisto, the flow-oriented component $B_{x,0}$ of the upstream magnetospheric field is set to zero in these model se-

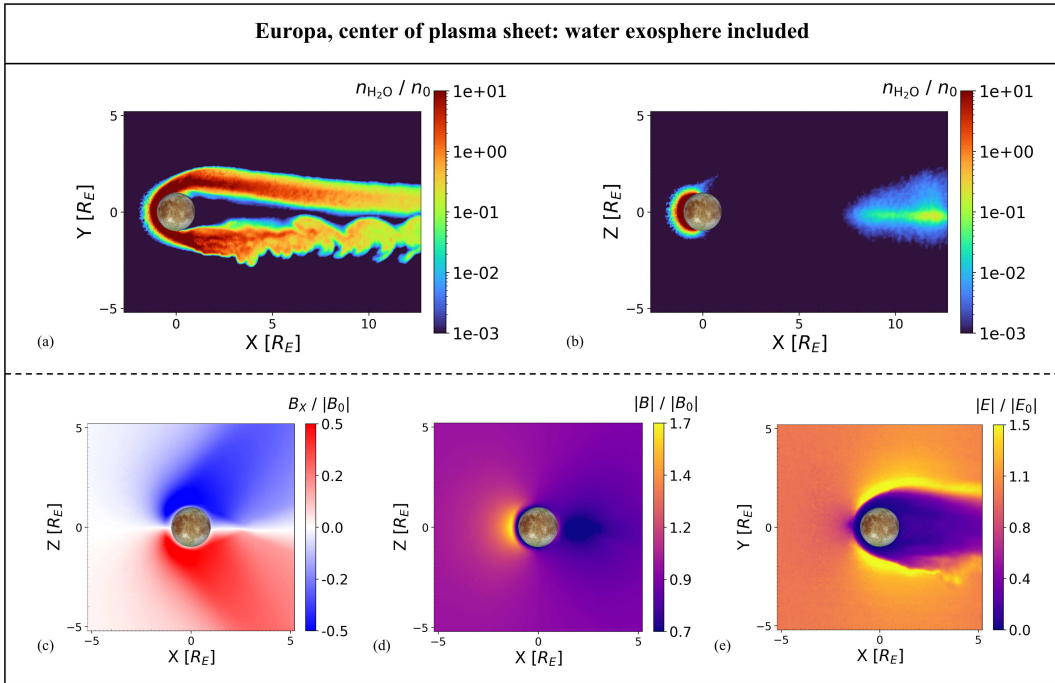


Figure 4. The perturbed plasma and electromagnetic environment near Europa when the moon is located at the center of the Jovian plasma sheet, including the localized H_2O exosphere near the moon’s ramside/subsolar apex. In panels (a) and (b), the number density of ionospheric H_2O^+ is displayed in the $z = 0$ and $y = 0$ planes, respectively. The flow-aligned component of the magnetic field B_x is plotted in panel (c) in the $y = 0$ plane. The magnitude of the magnetic field within the same plane is displayed in panel (d). The magnitude of the electric field is plotted in panel (e) for the $z = 0$ plane, containing the upstream flow velocity \mathbf{u}_0 , the background convective electric field vector $\mathbf{E}_0 = -\mathbf{u}_0 \times \mathbf{B}_0$, and the center of the moon. All quantities are normalized to the background magnetosospheric quantities at Europa, i.e., n_0 for panels (a) and (b) and $|\mathbf{B}_0|$ for panels (c) and (d). The electric field magnitude (panel (e)) is normalized to $|\mathbf{E}_0| = |\mathbf{u}_0 \times \mathbf{B}_0|$.

tups. As depicted in panels 3(a) and 3(c), B_x becomes negative (blue) north of each moon, and positive (red) south of it, with perturbations reaching strengths of $|\mathbf{B}_0|/2$ at Europa and $3|\mathbf{B}_0|/2$ at Callisto. Impinging magnetosospheric plasma is slowed and deflected around the obstacle due to ionospheric mass-loading (e.g., Saur et al., 1998; Rubin et al., 2015; Liuzzo et al., 2015). The frozen-in magnetic field is draped around the moon, as depicted in the cutting plane containing the background field \mathbf{B}_0 (panels 3(a) and 3(c)). At large distances from either moon, where field contributions from ionospheric currents are neg-

ligible, the interaction generates a system of Alfvén wings which propagate along characteristics $\mathcal{Z}^\pm = \mathbf{u}_0 \pm \mathbf{v}_{A,0}$ and connect Jupiter's polar ionosphere to the local interaction region (Neubauer, 1980, 1998). At Callisto, where the flow is super-alfvénic when near the center of the plasma sheet, the Alfvén wings are inclined against \mathbf{B}_0 by $\arctan M_A \approx 74^\circ$. At Europa, however, the Alfvén wings are only inclined by 34° relative to the background magnetic field. An enhancement in magnetic field magnitude around the upstream apex of either moon is visible in panels 3(e) and 3(g), depicted in yellow. At Callisto, the enhancement in magnetic field magnitude reaches a value larger than $5|\mathbf{B}_0|$. However, at Europa, the field strength in the pileup region is intensified only by a factor of 1.75 (see panel 3(g)). When Callisto is located at the center of the Jovian plasma sheet, the background magnetospheric field strength is over a factor of 100 weaker than at Europa (see Table 1). The plasma beta is also three orders of magnitude higher than at Europa. Due to the reduced "stiffness" of the magnetospheric field lines at Callisto, the field strength in the pileup region is elevated (relative to the respective background field) much more than at Europa.

The region between the Alfvén wings where B_x becomes zero corresponds to a thin neutral sheet in Callisto's wake (Liuzzo et al., 2022). In this region, the magnetic field magnitude falls to approximately $|\mathbf{B}_0|/2$ (see panels 3(e)). In contrast to Callisto where the Alfvén wings are strongly inclined towards the corotational flow direction, the Alfvén characteristics at Europa are only slightly inclined relative to \mathbf{B}_0 . Therefore, in the plane containing \mathbf{B}_0 , the region of reduced field strength is widened and exhibits a triangular shape. In panel 3(g), this region is depicted in dark purple with a wakeside depletion of about 30% of $|\mathbf{B}_0|$. The downstream deficit of magnetic pressure is compensated by the enhanced particle pressure of the ionospheric pick-up ions that populate this region at each moon (see, e.g., Liuzzo et al. (2015) or Arnold, Liuzzo, and Simon (2020) for details).

In panels 3(i) and 3(k), within the $z = 0$ plane (i.e., parallel to \mathbf{E}_0) the electric field magnitude falls close to zero (dark purple) in the wake region of either moon ($x > 0$). At Europa, this depletion region is approximately symmetric between the Jupiter-facing ($y > 0$) and Jupiter-averted ($y < 0$) half spaces. Comparatively, the region where \mathbf{E} is reduced near Callisto extends about one R_C further into the Jupiter-averted half space, and $|\mathbf{E}|$ returns to its background value in the $y > 0$ half space at a much larger x value than it does in the $y < 0$ half space. At both moons, the wakeside depletion

929 in $|\mathbf{E}|$ is a consequence of reduced bulk flow velocity \mathbf{u} as the magnetospheric plasma is
 930 mass-loaded by slow ionospheric constituents. In Europa's environment, where the Jo-
 931 vian background field strength is $|\mathbf{B}_0| \approx 400 \text{ nT}$, pickup ion gyroradii are less than $0.2R_E$.
 932 Therefore, the pickup tail is approximately symmetric about the y axis in planes par-
 933 allel to the undisturbed convective electric field (see also Arnold, Liuzzo, & Simon, 2020).
 934 At Callisto, the magnetospheric field strength is two orders of magnitude lower than at
 935 Europa, so heavy O₂ and CO₂ pickup ions have gyroradii larger than $6R_C$, yielding a
 936 highly asymmetric pickup tail (see also Liuzzo et al., 2015).

937 In the following, we discuss each moon's interaction at its maximum distance be-
 938 low the Jovian plasma sheet, i.e., the two right side sub-columns of Figure 3. When Cal-
 939 listo is located at this position, the background magnetospheric field is rotated by 72.5°
 940 against the $y = 0$ plane, and therefore the field line draping is only weakly visible in
 941 the cut shown by panel 3(b). Alternatively, at Europa the magnetospheric background
 942 field, and hence, the Alfvén wing characteristics ($\mathcal{Z}^\pm = \mathbf{u}_0 \pm \mathbf{v}_{A,0}$) are rotated out of
 943 the $y = 0$ plane by only 28.5°. In panel 3(d) the northern Alfvén characteristic \mathcal{Z}^- has
 944 a component out of the plane of the figure (i.e., it points away from Jupiter), and the
 945 southern characteristic \mathcal{Z}^+ has a component into the plane (towards Jupiter). At Eu-
 946 rropa, the induced dipole moment \mathbf{M}_{ind} is (nearly) aligned with the $(-y)$ axis. The vec-
 947 tor \mathbf{M}_{ind} generated by the nonzero \mathbf{B}_h forms an angle of 14° with the $(-y)$ axis at Cal-
 948 listo, i.e., it is tilted towards upstream.

949 At Callisto (panel 3(b)), an enhancement in B_x by $|\mathbf{B}_0|/5$ is visible above both the
 950 north and south pole of the moon, and a reduction of similar magnitude is present near
 951 the equator in the $y = 0$ plane. In this setup, the background field possesses a positive
 952 $B_{x,0}$ component of approximately $|\mathbf{B}_0|/4$. The induced dipole field takes the form of a
 953 “shamrock” in B_x viewed in the $z = 0$ plane (see also figures 1(b) and 1(j) of Liuzzo
 954 et al., 2022). If \mathbf{B}_h were completely aligned with $-\hat{\mathbf{y}}$, the B_x perturbation associated with
 955 the induced dipole is positive when x and y have opposite signs, and negative when both
 956 x and y have the same sign. A background field $B_{x,0} > 0$ rotates the shamrock struc-
 957 ture in B_x counterclockwise around the z axis. Therefore, the induced field at Callisto
 958 is characterized by $B_x < 0$ along the x axis, acting to reduce the ambient $B_{x,0}$ com-
 959 ponent. This rotation similarly causes an enhancement in B_x near the poles of Callisto
 960 in the $y = 0$ plane.

Immediately north and south of Europa, the B_x component (panel 3(d)) is negative (blue) and positive (red), respectively. At larger distances, the B_x component in this plane reverses its sign ($B_x > 0$, red, in the north, and $B_x < 0$, blue, in the south). In planes (approximately) perpendicular to the wing characteristics, the field lines of an Alfvén wing take the shape of a two-dimensional dipole (Neubauer, 1980). Consequently, outside of the wing tubes (which connect to Europa's ionosphere) the field lines form regions of “anti-draping”, i.e., the field vectors are antiparallel to those within the wing tubes to ensure field line closure (see, e.g., Figure 8 of Simon et al., 2011). This effect is visible in panel 3(d), since the distance between the center of the wing tubes and the cutting plane grows with increasing $|z|$ value. At Europa, the field strength in the ram-side pileup region (panel 3(h)) reaches $1.3|\mathbf{B}_0|$, accompanied by a depletion in magnitude downstream of the moon.

In the immediate vicinity of Callisto, the induced dipole acts to locally amplify the magnitude of the magnetic field by about 40%, as depicted by the bright yellow ring within the $y = 0$ plane (see panel 3(f)). Since the induced dipole moment mainly points in $(-y)$ direction, the vectors of the induced field possess a dominant component in the $(+y)$ direction (parallel to \mathbf{B}_0) within the $y = 0$ plane, thereby causing an approximately radially symmetric enhancement in the magnetic field magnitude within this plane. At Callisto, the electric field magnitude is reduced by up to 60% in a broad region extending downstream as well as into the Jupiter-facing and Jupiter-averted hemispheres, as shown in panel 3(j). This reduction in field strength is caused by the deflection of the upstream plasma flow around the Alfvén wings, whose characteristics \mathcal{Z}^\pm are close to the $z = 0$ plane. This deflection reduces $|\mathbf{u}|$ and produces a corresponding reduction in the magnitude of the convective electric field. The region of reduced electric field strength is asymmetric between $y > 0$ and $y < 0$ due to the positive $B_{x,0}$ component of the magnetospheric background field (see also Simon & Motschmann, 2009). In addition, when Callisto is at its maximum distance below the center of the Jovian plasma sheet, the 72.5° tilt of $|\mathbf{B}_0|$ against the $y = 0$ plane rotates the pickup tail away from the $z = 0$ plane, and therefore the tail does not contribute appreciably to the large-scale reduction of $|\mathbf{E}|$ in panel 3(j). However, at Europa, the tail of escaping ions is still primarily contained to the $z = 0$ plane, as can be seen from the similarity in the structure of $|\mathbf{E}|$ between panels 3(k) and 3(l). Even below the center of the Jovian plasma sheet, the background magnetic field at Europa is still nearly aligned with the z axis (see Table 1), and as a

994 result the electric field depletion remains approximately symmetric between the $y > 0$
 995 and $y < 0$ half spaces (see panel 3(l)).

996 For the case of an additional water atmosphere included around Europa's subso-
 997 lar and (coincident) upstream apex (Roth, 2021), Figures 4(a) and 4(b) display the num-
 998 ber density of the H_2O^+ pickup tail in the planes containing the center of Europa, \mathbf{u}_0 ,
 999 and \mathbf{E}_0 or \mathbf{B}_0 , respectively. In the $y = 0$ plane (panel 4(b)), the H_2O^+ tail exhibits a
 1000 gap in density between Europa's ionosphere (dark red) and the distant tail region (start-
 1001 ing around $x \approx 8R_E$). The reason for this is revealed in panel 4(a): the H_2O^+ ions form-
 1002 ing the tail are swept around the Jupiter-averted and Jupiter-oriented faces of Europa
 1003 as they propagate downstream. Immediately downstream of Europa, the tail takes a two-
 1004 pronged shape because the H_2O^+ ions (which are generated only around the ramside apex)
 1005 must first be transported around the moon in order to reach the downstream region. These
 1006 ions are thus carried out of the $y = 0$ plane around both sides of Europa, only for the
 1007 separated tails to rejoin about $8R_E$ downstream (panel 4(b), shown as light blue and green).
 1008 The ionospheric H_2O^+ has a factor of 10 greater number density than the ambient mag-
 1009 netospheric plasma ($n_0 = 200 \text{ cm}^{-3}$) in the region immediately surrounding the moon,
 1010 and its density falls to values similar to n_0 at approximately $7R_E$ downstream. The struc-
 1011 ture of the pick-up tail formed by O_2^+ ions from Europa's global atmosphere looks some-
 1012 what different. However, the physics involved in shaping the O_2^+ tail have already been
 1013 discussed in detail by, e.g., Arnold, Simon, and Liuzzo (2020), and we refer the reader
 1014 to that publication for further information.

1015 In panel 4(a), a wave-like pattern is visible in the long, Jovian-averted flank of the
 1016 H_2O^+ pickup tail. In the $y < 0$ half space (where \mathbf{E}_0 points *away* from Europa), flow
 1017 shear between ionospheric H_2O^+ and magnetospheric thermal plasma results in the ex-
 1018 citation of bi-ion waves. The location and shape of the wave signature are consistent with
 1019 modeled bi-ion wave features in the pickup tails of comets (Bagdonat & Motschmann,
 1020 2002) or Pluto (Delamere, 2009; Feyerabend et al., 2017). Specifically, in agreement with
 1021 our results for Europa, such waves were found to form only in the half space where \mathbf{E}_0
 1022 points away from the respective object (e.g., Delamere, 2009; Feyerabend et al., 2017).
 1023 The electric field perturbations in the $z = 0$ plane (panel 4(e)) are similar to the case
 1024 of Europa at the center of the Jovian plasma sheet without the H_2O atmosphere (panel
 1025 3(k)), except for a filamented structure visible along the $y < 0$ boundary of the deple-
 1026 tion region. This structure corresponds to the aforementioned wave signature which maps

1027 into the bulk velocity, and hence, leaves a weak imprint on the electric field. In the $y =$
 1028 0 plane, the magnetic draping pattern remains very similar to that obtained without in-
 1029 cluding the H₂O atmospheric component (panels 4(c) and 4(d)). This finding is consis-
 1030 tent with the MHD modeling results of Cervantes and Saur (2022), who demonstrated
 1031 that, even when the ram-wake asymmetry of the global O₂ atmosphere is *not* consid-
 1032 ered, the water vapor component generates only localized modifications to Europa's mag-
 1033 netic environment.

1034 3.2 Variability of ENA Emissions at Europa

1035 Figure 5 displays the global ENA emissions captured by a spherical detector around
 1036 Europa when the moon is located at the center of the Jovian plasma sheet. The model
 1037 results for a (hypothetical) case when the magnetospheric field is uniform and southward
 1038 are given in the left column, and results for motion of the parent protons through draped
 1039 fields are given in the right column. The ENA flux onto the spherical model detector is
 1040 projected onto a rectangular surface for visualization, using the West Longitude coor-
 1041 dinate system described in section 2. Each row corresponds to a single initial energy for
 1042 the parent protons when launched from the starting grid: 1 keV in row (a-b), 10 keV in
 1043 row (c-d), 40 keV in row (e-f), 70 keV in row (g-h), and 100 keV in row (i-j). Due to ac-
 1044 celeration of the parent protons in the draped electromagnetic fields, the energies of the
 1045 detectable ENAs may differ from the initial proton energies. However, for energetic pro-
 1046 tons traveling through Europa's environment, the changes in energy are generally small
 1047 (see Figure 13 of Nordheim et al., 2022).

1048 In the case of the uniform, southward field (panels 5(a), (c), (e), (g), and (i)) a dom-
 1049 inant band feature of high ENA flux parallel to Europa's equator is visible across the cen-
 1050 ter of each panel. This band is shaped like an annulus on the detector, wrapping around
 1051 Europa and oriented normal to the background magnetic field \mathbf{B}_0 . For example, 83% of
 1052 the total ENA flux through the detector in the 40 keV run (panel 5(e)) is contained be-
 1053 tween latitudes of $\pm 33^\circ$. Comparing the emission patterns in uniform fields at different
 1054 energies (panels 5(a), (c), (g), and (i)) reveals that the morphology of this equatorial band
 1055 exhibits little variation as a function of parent ion energy. Within the band, the detected
 1056 ENA flux is maximized around 300° W longitude at each energy, i.e., slightly west of the
 1057 detector's ramside apex (270° W longitude). However, the magnitude of the peak flux
 1058 varies non-monotonically as a function of initial proton energy.

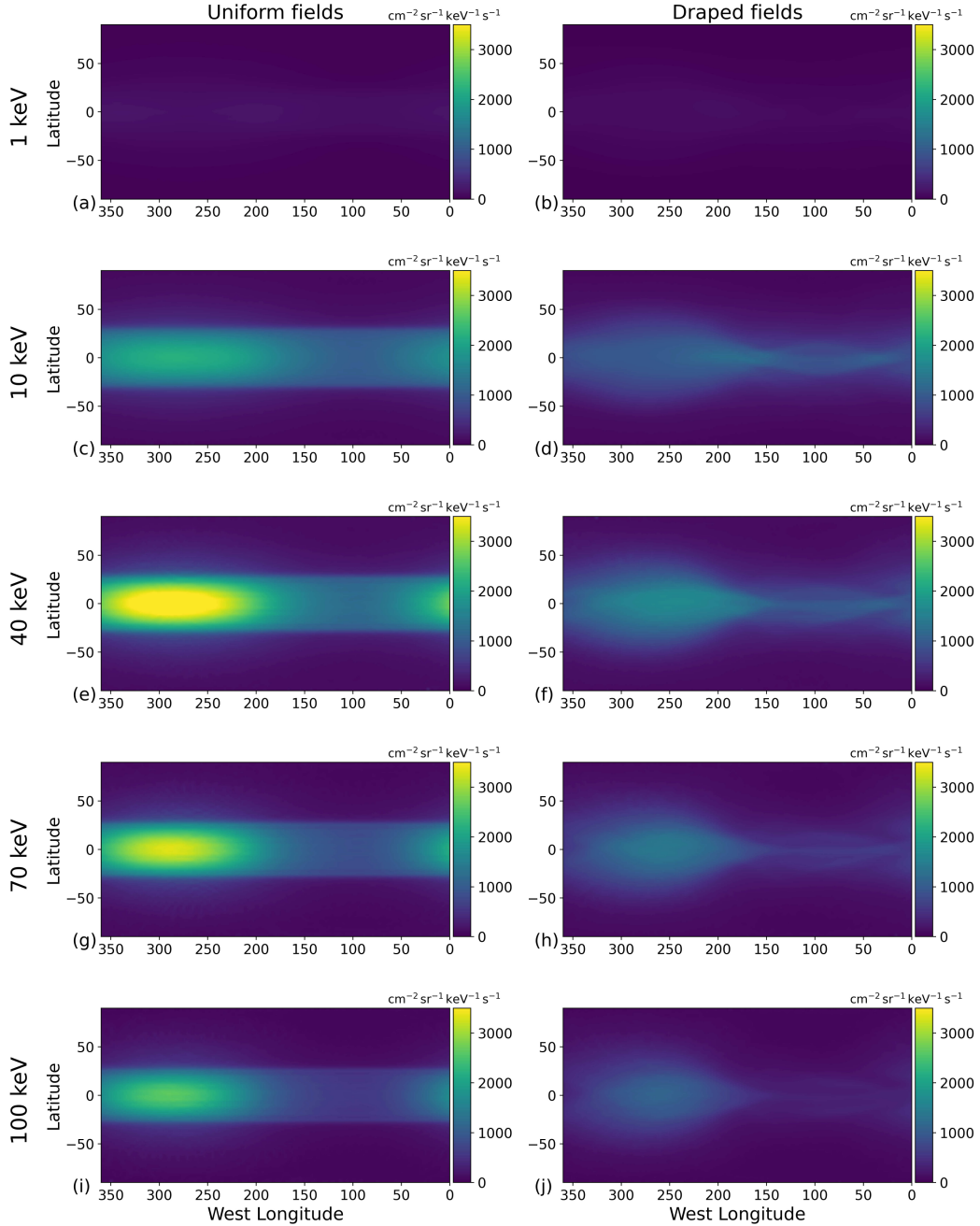


Figure 5. Global ENA emission flux maps from Europa's atmosphere through a concentric spherical detector with radius $2R_E$. In this scenario, Europa is located at the center of the Jovian plasma sheet (see Table 1). The West Longitude coordinate system is used in this projection. Each row represents ENA emissions generated by parent ions initialized on the starting grid at a certain kinetic energy, namely 1 keV in row (a-b), 10 keV in row (c-d), 40 keV in row (e-f), 70 keV in row (g-h), and 100 keV in row (i-j). The left column (panels (a), (c), (e), (g), and (i)) illustrates the ENA emission morphology when the energetic parent protons are evolved through the uniform Jovian background fields \mathbf{B}_0 and \mathbf{E}_0 . The right column (panels (b), (d), (f), (h), and (j)) displays ENA emissions when the parent ions move through the perturbed electromagnetic fields from the AIKEF hybrid model (see panels (c), (g), and (k) of Figure 3).

1059

The PAD of the energetic parent ions is isotropic in this model setup. However,
1060 ENA emissions at Europa are concentrated within this equatorial band perpendicular

1061 to \mathbf{B}_0 because parent ions with pitch angles near 90° make the dominant contribution
 1062 to the ENA flux. To illustrate this, we consider two test particles initialized on the start-
 1063 ing grid at an energy of $E = 40$ keV: the first of these parent ions is launched from the
 1064 upstream face of the starting grid and has a pitch angle of 90° . Its guiding center drifts
 1065 along a straight line parallel to the $(+x)$ axis, confined to the $y = 0$ plane and displaced
 1066 northward by $z = R_E + h_{s,E}$, where $h_{s,E}$ is the atmospheric scale height (see equa-
 1067 tion (4)). Thus, *all* ENAs emitted by this parent ion hit the detector; none of them are
 1068 obstructed by Europa's solid body. The "ENA trace" left by this proton on the detec-
 1069 tor is confined to a latitude of $\arcsin\left(\frac{R_E+h_{s,E}}{2R_E}\right) = 32.1^\circ$, i.e., it forms a circle. The sec-
 1070 ond parent ion has a pitch angle of 0° and is initialized on the starting grid's northern
 1071 $(+z)$ face such that its guiding center moves southward within the $y = 0$ plane and down-
 1072 stream of Europa at $x = R_E + h_{s,E}$. In other words, the trajectory of the guiding cen-
 1073 ter is perpendicular to that of the first particle. This second test particle translates mainly
 1074 along \mathbf{B}_0 because the corotation drift velocity in $(+x)$ direction ($|\mathbf{u}_0| = 100$ km/s) is
 1075 slow relative to the speed $\sqrt{\frac{2E}{m_p}} = 2,768$ km/s of a parent proton at $E = 40$ keV. The
 1076 length of the guiding center's trajectory through the atmosphere is the *same* for both
 1077 test particles: $l = 2\sqrt{(2R_E)^2 - (R_E + h_{s,E})^2} \approx 3.39R_E$. However, these two protons'
 1078 capacity to generate ENA flux is dependent on their actual path length within the at-
 1079 mosphere, and not merely the path length l traveled by the guiding center. Gyration causes
 1080 the actual path within the atmosphere to be extended compared to l only for the first
 1081 proton. Taking into account its drift in $(+x)$ direction at velocity u_0 , its guiding cen-
 1082 ter traverses Europa's atmosphere in $l/|\mathbf{u}_0| \approx 53$ s, equal to the time it takes to com-
 1083 plete about 330 gyrations within the atmosphere. Thus, the parent proton's path length
 1084 inside the atmosphere associated with gyration alone reads $330(2\pi r_g) = 93.6R_E$ (where
 1085 $r_g = 0.045R_E$ is the gyroradius, see Table 2). In contrast, the second parent ion trav-
 1086 els along the magnetic field and traverses a path length of $l \approx 3.39R_E$ inside of the at-
 1087 mosphere (in less than 2 seconds).

1088 Therefore, the first parent ion interacts with the atmosphere for at least 28 times
 1089 the path length that the second ion does. In other words, parent ions drifting with pitch
 1090 angles near 90° trace the longest paths through the atmosphere and emit the majority
 1091 of the ENA flux through the detector, forming the band of high flux perpendicular to
 1092 \mathbf{B}_0 seen in the left column of Figure 5. In addition, the second particle (moving along
 1093 the magnetic field) emits ENAs into only a small localized patch on the detector, clus-

tered at the point where its trajectory exits the detector sphere. Taking into account parent protons from the entire (isotropic) PAD, our example shows that their path length within the atmosphere maximizes at $\alpha = 90^\circ$ and falls rapidly as the velocity gains a field-aligned component. The intense ENA emissions detectable at Europa stem from long path lengths within the atmosphere, which are a result of the energetic proton's gyroradii being *small* compared to the extension of the moon's neutral gas envelope. This still holds at the highest energies considered because even a 100 keV proton has a gyroradius of only $r_g = 0.07R_E \approx 1.1h_{s,E}$ (see Table 2).

In the purely southward magnetic field used in this model configuration, ions with pitch angles of 90° gyrate in planes of constant z , which is why the outer boundaries of the band are circles with constant z value (i.e., constant latitude) on the detector sphere. In other words, the orientation of the equatorial band of high ENA flux on the detector sphere (left column of Figure 5) is governed by the orientation of the background magnetic field \mathbf{B}_0 . The latitudinal extension of the band is determined by the extension of the Europa obstacle along the magnetic field lines (i.e., in $\pm z$ direction), which is approximately $z = \pm(R_E + h_{s,E})$. At these z values, the gyroplanes of energetic protons are approximately tangential to Europa's dense, lower atmosphere (see also Figure 6(a) in Tippens et al., 2022). ENAs emitted at $z = \pm(R_E + h_{s,E})$ intersect the detector at a latitude θ_b given by

$$\sin \theta_b = \pm \left(\frac{R_E + h_{s,E}}{R_D} \right) , \quad (21)$$

where $R_D = 2R_E$ is the radius of the spherical detector (see also equation (11) in Tippens et al., 2022). Substituting $h_{s,E} = 100$ km yields $\theta_b = \pm 32.14^\circ$, consistent with our modeled results (left column of Figure 5).

The band of enhanced ENA flux does not gradually disappear with increasing latitude, but its boundaries are sharply defined around the “cut-off latitude” θ_b approximately given by equation (21). For instance, at an initial parent proton energy of 70 keV, the detected ENA flux transitions from about $1500 [\text{cm}^2 \text{ sr keV s}]^{-1}$ (turquoise) to $250 [\text{cm}^2 \text{ sr keV s}]^{-1}$ (dark blue) across less than 5° in latitude at the edges of the band (see panel 5(g)). This rapid drop in detected ENA flux with increasing latitude is mainly caused by the exponential decrease of atmospheric density with rising altitude (see equation (4)). Since the gyration planes of parent ions that generate the band are nearly parallel to the $z = 0$ plane, parent ions with increasing $|z|$ positions interact with a successively less dense re-

1125 gion of the atmosphere, which in turn generates reduced ENA emissions. In addition,
 1126 the spherical shape of the atmosphere contributes to the steep decrease of detected ENA
 1127 flux with latitude. For ions with pitch angles near 90° and $|z| > 1R_E$, (i.e., their gy-
 1128 roplanes intersect Europa's atmosphere but not Europa) the path length of the guiding
 1129 center within the atmosphere decreases with increasing $|z|$ value. This reduces the length
 1130 of the trajectory segment where such an ion can generate ENAs that would populate the
 1131 detector at a specific latitude, further amplifying the latitudinal decrease in ENA flux
 1132 with increasing $|z|$. These two effects combined result in the stark decrease of detected
 1133 ENA flux with latitude, as seen in the left column of Figure 5.

1134 In uniform fields, the ENA flux within the equatorial band is maximized at lon-
 1135 gitudes slightly west of the ramside apex, shifted approximately 20° – 30° in longitude to-
 1136 wards the Jupiter-facing apex. The observable ENA flux intensity drops with increas-
 1137 ing longitudinal distance to the maximum, with the minimum also positioned slightly
 1138 west of the detector's wakeside apex (see, e.g., panel 5(g)). This asymmetry is most clearly
 1139 visible at an initial parent ion energy of 40 keV in panel 5(e), but it is a persistent trend
 1140 also apparent in panels 5(c), (g), and (i). To investigate the reason for the shift in the
 1141 longitude of maximal emissions, we conduct a numerical experiment: consider a single,
 1142 proton trajectory that is initialized with an energy of 40 keV. This proton has a pitch
 1143 angle of 90° with an initial velocity parallel to $\hat{\mathbf{y}}$. It is launched on the starting grid at
 1144 $\mathbf{r}(t = 0) = (-8R_E, 0, 0)$, such that its trajectory is given by

$$\mathbf{r}(t) = r_g \begin{pmatrix} \cos \Omega t \\ \sin \Omega t \\ 0 \end{pmatrix} + \begin{pmatrix} u_0 t - (8R_E + r_g) \\ 0 \\ 0 \end{pmatrix}, \quad (22)$$

1145 where Ω denotes the gyrofrequency. Therefore, the proton's trajectory is confined to the
 1146 $z = 0$ plane, and the same holds for the trajectories of all ENAs it emits. Most impor-
 1147 tantly, the proton spends equal path lengths of its trajectory in the $y > 0$ and the $y <$
 1148 0 half spaces. We remind the reader that in our model, Europa's atmosphere is symmet-
 1149 ric between these two half spaces.

1150 The evolution of this parent ion is illustrated in Figure 6. Panels 6(a) and 6(b) show
 1151 projections of its trajectory onto the $z = 0$ and $y = 0$ planes, respectively. Panel 6(c)
 1152 displays the relative contributions of the detectable ENA flux onto the Jupiter-facing (or
 1153 Jupiter-averted) hemisphere of the detector, corresponding to cyan (or gold). Panels 6(d)

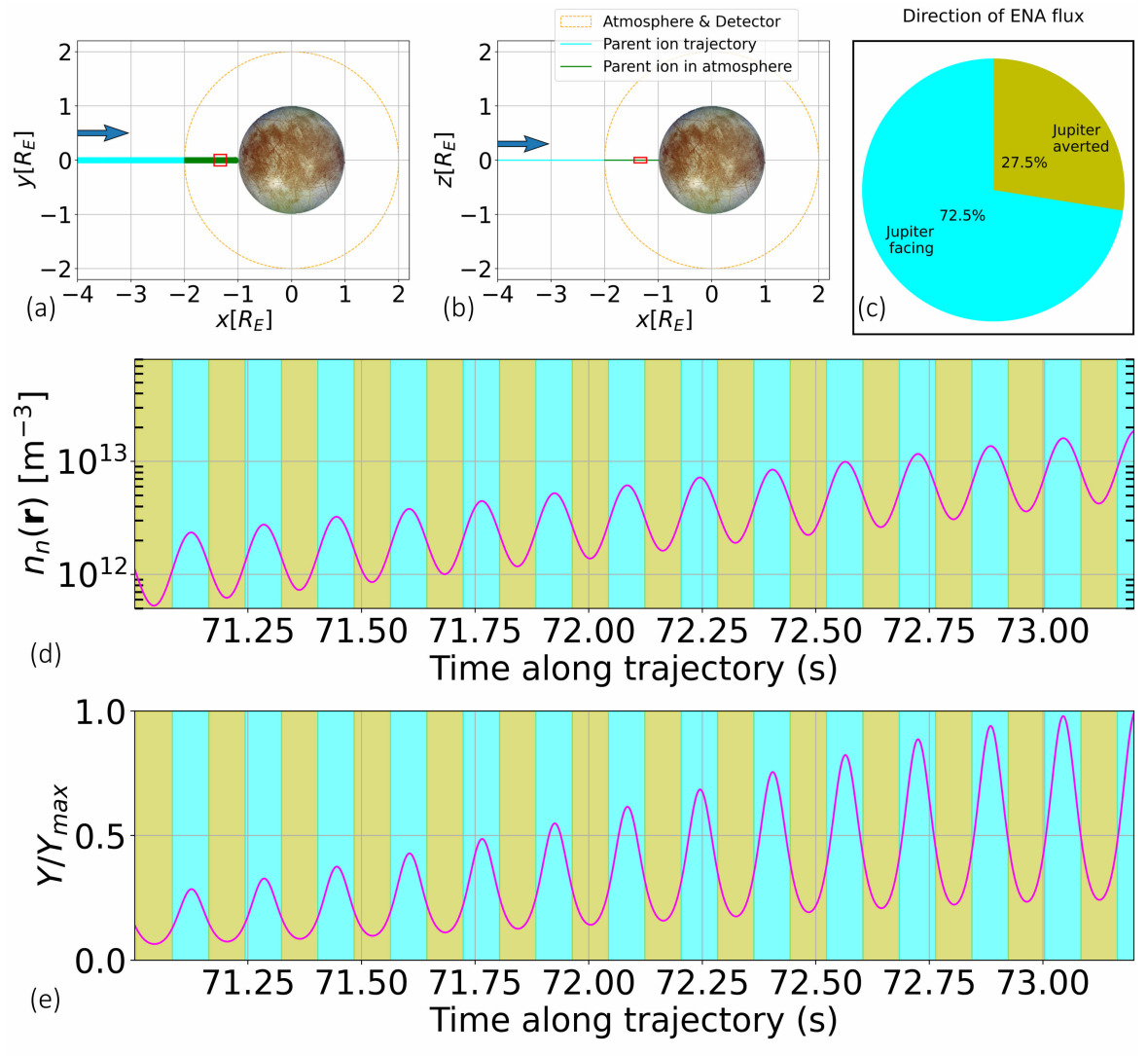


Figure 6. A sample energetic proton trajectory and ENA emission statistics highlighting the effect of parent ion gyration within the atmosphere on the morphology of ENA emissions at Europa. The parent ion is initialized at $\mathbf{r}(t = 0) = (-6R_E, 0, 0)$ with energy $E = 40 \text{ keV}$, pitch angle $\alpha = 90^\circ$, and initial velocity $\dot{\mathbf{r}}(t = 0) = (0, \sqrt{\frac{2E}{m_p}}, 0)$, and moves through *uniform* electromagnetic fields. The projection of the particle trajectory into the $z = 0$ and $y = 0$ planes is displayed in panels (a) and (b), respectively, with the blue arrow indicating the approximate direction of guiding center motion. The red rectangle contains the segment of the trajectory from $71 \text{ s} - 73.27 \text{ s}$, as shown in panels (d) and (e). The orange dashed circle represents the outer boundary of the moon's atmosphere in our model, coinciding with the detector sphere. The trajectory is depicted in cyan outside of the atmosphere (where no ENAs are produced) and green inside the atmosphere (where ENA generation takes place). In panel (c), the total ENA flux detected on the Jovian-oriented hemisphere of the detector (i.e., $y > 0$) is shown in cyan and compared to the total ENA flux detected by the Jovian-averaged hemisphere of the detector (i.e., $y < 0$), shown in gold. Note, only those ENAs which do not bombard Europa itself are actually detected and included in panel (c). The coordinate on the horizontal axes of panels (d) and (e) refers to the time that has elapsed since the ion was initiated at $\mathbf{r}(t = 0)$, see equation (22). The background colors in panels (d) and (e) show sign(\dot{r}_y) for the parent proton, with the time window shaded as either cyan when positive or gold when negative. In segments with $\dot{r}_y > 0$ (or $\dot{r}_y < 0$), the proton emits ENAs toward the Jupiter-facing (Jupiter-averaged) hemispheres of the detector. Panels (d) and (e) display the atmospheric neutral density at the location of the proton and the differential ENA flux $Y = |\text{d}J|$ emitted at each timestep as the parent proton travels through the atmosphere, respectively. In panel (e), the emitted ENA flux is normalized to the maximum value $Y_{\max} \approx 0.02 [\text{cm}^2 \text{ sr keV s}]^{-1}$ produced around $t = 73.27 \text{ s}$. Beyond that time (not shown in the figure), the emitted ENA flux during each gyration decreases since the parent proton has already depleted most of its initial numerical weight.

and 6(e) then show the atmospheric density $n_n(\mathbf{r})$ at the proton's position and the ENA flux generated at each point in time, respectively. The shading in panels 6(d) and 6(e)

1154

1155

denotes the sign of \dot{r}_y , which reverses each half-gyration. Since each ENA is emitted with
 the parent proton's momentary velocity, the sign of \dot{r}_y determines whether the ENA is
 emitted toward the $y > 0$ or the $y < 0$ half sphere of the detector (see panels 6(d) and
 (e)). The southward orientation of the magnetospheric background field \mathbf{B}_0 causes the
 parent proton to gyrate in the mathematically positive sense. Therefore, as it drifts into
 the atmosphere and begins to generate ENAs, it is located at lower altitudes (i.e., in a
 $more dense$ region of the atmosphere) when it emits ENAs towards the Jovian-facing hemi-
 sphere of the detector ($\dot{r}_y > 0$), and is located at higher altitudes (i.e., in a *less dense*
 region of the atmosphere) when it emits ENAs towards the detector's Jovian-averted hemi-
 sphere (i.e., $\dot{r}_y < 0$). As shown in panels 6(d) and 6(e), maxima in local atmospheric
 density at the proton's location coincide with the center of each interval for which $\dot{r}_y >$
 0, and also with maxima of the emitted ENA flux.

This asymmetric emission process causes a larger amount of ENA flux to be de-
 tected on the Jovian-facing hemisphere of the detector compared to the Jovian-averted
 hemisphere (see panel 6(c)). In other words, the slight shift of the ENA emission max-
 imum toward Jupiter (see left column of Figure 5) arises from the sense of proton gy-
 ration in the southward magnetic field \mathbf{B}_0 , combined with the fact that these particles
 can complete numerous gyrations within Europa's atmosphere (see also panels 6(a) and
 (b)). We note that analogously, the minimum of ENA flux does not occur exactly at the
 wakeside apex of the detector (90° W longitude), but is shifted toward larger longitudes
 (see left column of Figure 5). The solid body of Europa absorbs part of the emitted ENA
 population. Consequently, not all emitted ENAs are ultimately detected in our exper-
 iment displayed by Figure 6. However, during each gyroperiod, the drift displacement
 of an energetic proton toward Europa is smaller than the gyroradius and significantly
 smaller than R_E (see Table 2). Specifically, on scales of a single gyration the proton tra-
 jectory is approximately circular. Therefore, absorption of newly generated ENAs at Eu-
 ropa's surface does *not* introduce any new, substantial asymmetries into the ENA flux
 through the detector sphere.

When Europa is at the center of the Jovian plasma sheet, the average ENA flux
 detected in draped electromagnetic fields is diminished by about 50% in intensity across
 all energies compared to the average detectable ENA flux in uniform fields (see right col-
 umn of Figure 5). The slight longitudinal shift of the emission maximum toward Jupiter
 persists when field line draping is considered. The equatorial band of high ENA flux that

1189 was visible at all energies in uniform fields (see left column of Figure 5) is no longer present
 1190 in draped fields. For instance, the region of (slightly) enhanced ENA flux on the wake-
 1191 side of the detector shrinks in latitudinal extent when moving from uniform to draped
 1192 fields. In the latter setup, this region is confined between latitudes of $\pm 10^\circ$ (see, e.g., pan-
 1193 els 5(d), (e), and (f)), compared to $\pm 33^\circ$ in uniform fields. However, a “bulge-like” en-
 1194 hancement in ENA flux remains slightly west of the detector’s ramside apex, reaching,
 1195 e.g., $1750 [\text{cm}^2 \text{ sr keV s}]^{-1}$ at an initial proton energy of $E = 40 \text{ keV}$ (see panel 5(f)).
 1196 This corresponds to 44% of the maximum value reached in the uniform case at the same
 1197 energy ($4000 [\text{cm}^2 \text{ sr keV s}]^{-1}$, see panel 5(f)).

1198 An example of an energetic proton trajectory that contributes to the modified ENA
 1199 flux pattern in draped fields is depicted in Figure 7. Two energetic protons are propa-
 1200 gated with identical initial conditions: one through uniform electromagnetic fields (left
 1201 column) and another through perturbed fields from AIKEF (right column). In uniform
 1202 fields, the parent proton can readily penetrate into Europa’s wakeside atmosphere, emit-
 1203 ting ENA flux onto the detector (green segment of the trajectory). These ENAs contribute
 1204 to the signature on the wakeside of the detector, visible in the left column of Figure 5.
 1205 In draped fields, a parent proton launched with the same initial conditions is already de-
 1206 flected while north of Europa, far before it ever reaches the moon’s atmosphere (right
 1207 column of Figure 7). The draped field lines cause the energetic proton’s trajectory to
 1208 descend towards the *ramside* atmosphere (see blue arrow in panel 7(d)). ENAs emitted
 1209 along this parent proton’s trajectory at $|z| > R_E$ may populate any longitude of the
 1210 detector. However, the proton’s ability to populate the wakeside of the detector at low
 1211 latitudes is highly limited, since Europa absorbs most of the ENAs emitted into the $x >$
 1212 0 half space. Thus, in draped fields the proton can populate the wakeside of the detec-
 1213 tor with ENAs only from high latitudes along its trajectory, i.e., from regions where the
 1214 atmosphere is dilute (and hence, the emitted ENA flux is low). In contrast, when the
 1215 proton travels through the dense atmosphere near the ramside apex, all detectable ENAs
 1216 are emitted toward the upstream hemisphere of the detector. This parent proton’s tra-
 1217 jectory in both field configurations exemplifies how draped fields can redistribute par-
 1218 ent protons’ ENA emissions from the wakeside of the detector to the ramside, thereby
 1219 contributing to the thinning of the wakeside band seen in Figure 5.

1220 An example parent proton that illustrates a separate mechanism that acts to at-
 1221 tenuate the detectable ENA flux in draped fields is displayed in Figure 8. This 40 keV

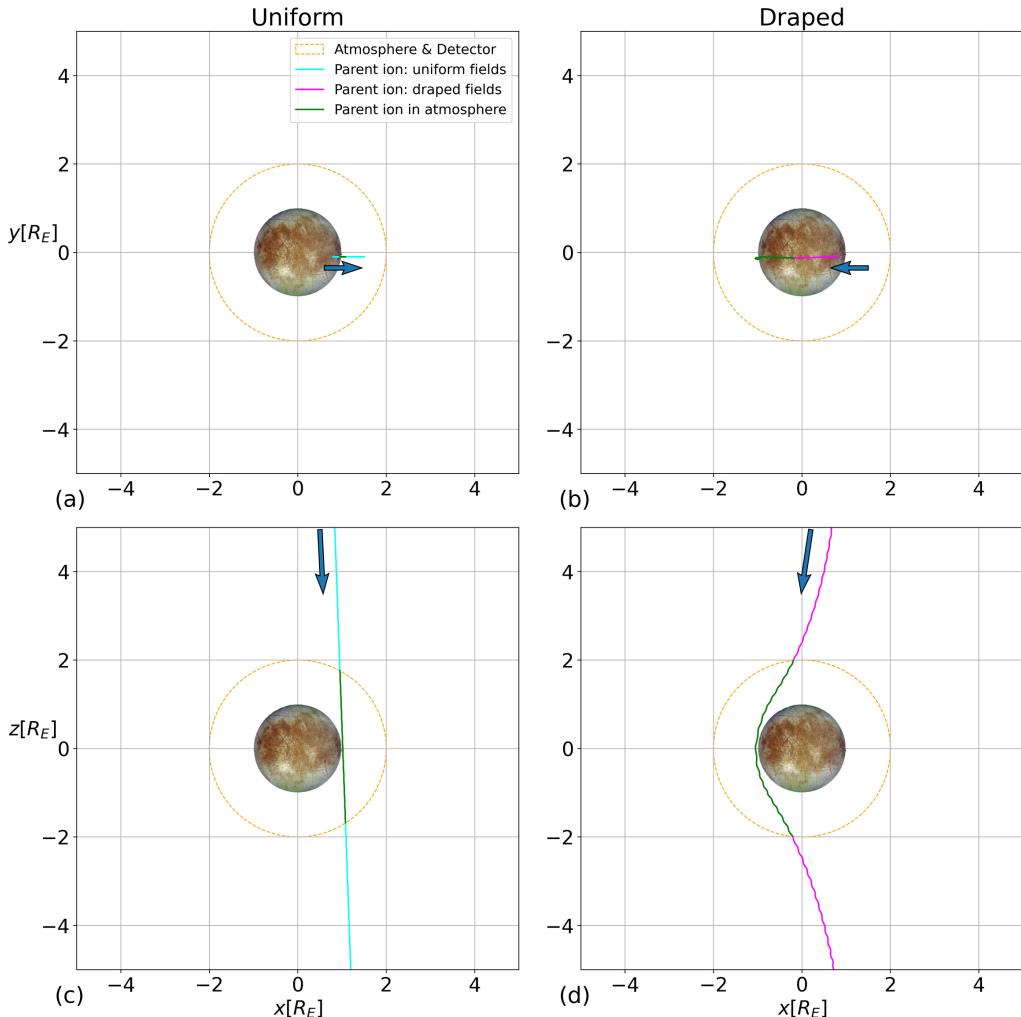


Figure 7. Sample energetic parent protons' evolution through Europa's electromagnetic environment. The 3D ion trajectories are projected into both the $z = 0$ (panels (a) and (b)) and $y = 0$ planes (panels (c) and (d)). We include two separate proton trajectories with the same initial conditions, traced through uniform (left column) and draped fields (right column). The arrow in each panel indicates the direction of guiding center motion during the ion's initial approach of Europa. When outside of the atmosphere, the proton trajectory is plotted in cyan (uniform fields) or magenta (draped fields). Both cases are colored in green when they are inside the atmosphere and generate ENAs. For both uniform and draped fields, the sample ion is initialized with $\mathbf{r}(t = 0) = (0.8 R_E, -0.1 R_E, 6 R_E)$, i.e., outside of the domain shown in the figure, and $\dot{\mathbf{r}}(t = 0) = \left(\sqrt{\frac{2E}{m_p}} \sin 5^\circ, 0, -\sqrt{\frac{2E}{m_p}} \cos 5^\circ\right)$, with a kinetic energy of $E = 40$ keV.

1222 proton is initialized at $\mathbf{r}(t = 0) = (-6R_E, -0.1R_E, -R_E/2)$, i.e., upstream of Europa,
 1223 in both uniform fields (left column) and draped fields (right column). The proton is launched
 1224 with an initial velocity of $\dot{\mathbf{r}}(t = 0) = \left(\sqrt{2E/m_p}\right) \hat{\mathbf{x}}$, corresponding to a pitch angle of
 1225 90° in the undisturbed upstream field \mathbf{B}_0 . Since the field is oriented southward, this ion's
 1226 gyration in uniform fields remains confined to the $z = -R_E/2$ plane throughout its evo-
 1227 lution until impacting Europa. Thus, the detected ENA flux associated with this par-
 1228 ticle is confined to a single latitude on the detector of -14° . Due to absorption by Eu-

1229 Europa's solid body, this proton cannot emit any ENAs toward the downstream hemisphere
 1230 of the detector. Such parent ions provide the dominant contribution to the ramside por-
 1231 tion of the band feature seen in the left column of Figure 5. Alternatively, in draped fields,

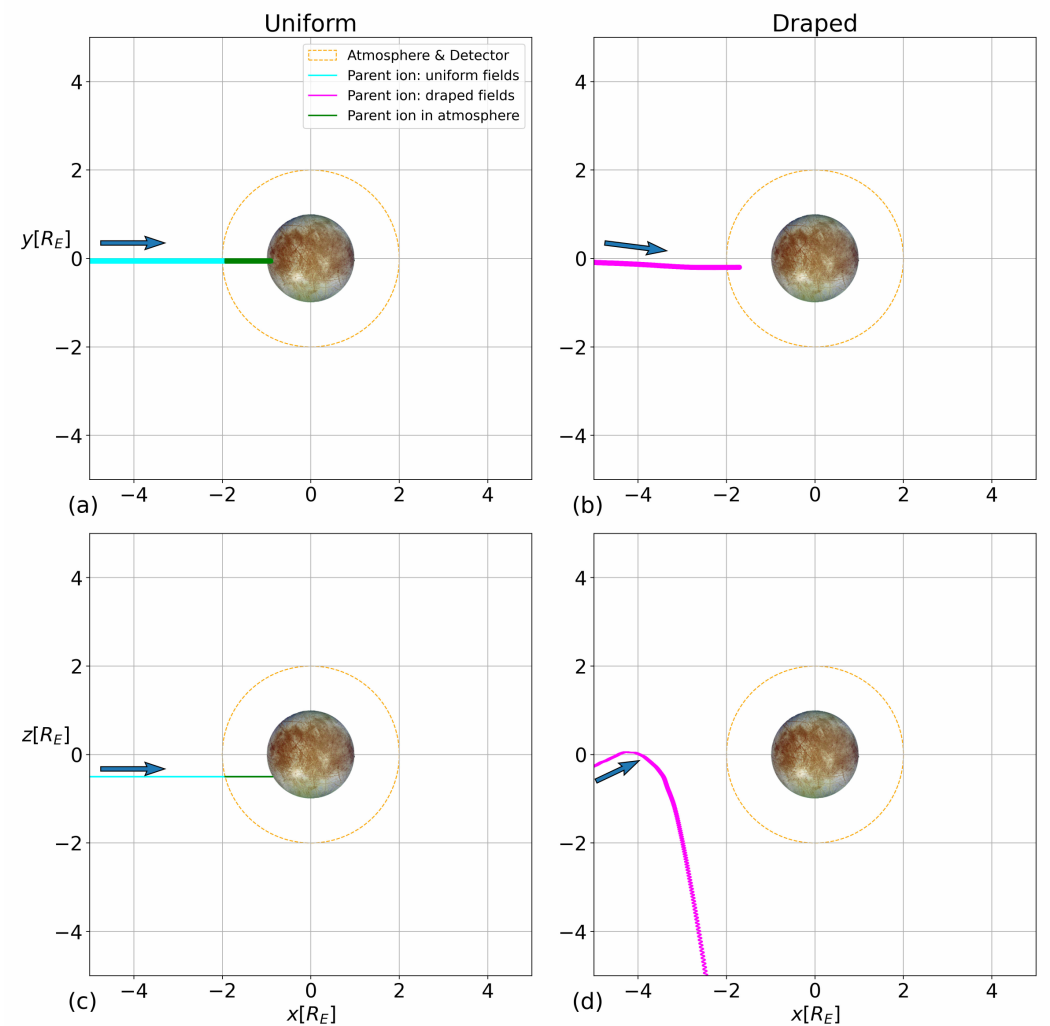


Figure 8. Sample energetic protons' evolution through Europa's environment, depicting a common fate shared by ions initialized upstream of the moon with pitch angles of 90° . The layout of this figure is identical to that of Figure 7, with analogous coloring. The test particles are initialized with $\mathbf{r}(t=0) = (-6R_E, -0.1R_E, -0.5R_E)$, i.e., outside of the domain plotted here, and $\dot{\mathbf{r}}(t=0) = (\sqrt{\frac{2E}{m_p}} \sin 90^\circ, 0, -\sqrt{\frac{2E}{m_p}} \cos 90^\circ)$ at an energy of $E = 40$ keV.

1231
 1232 the same parent proton is not capable of generating any ENA flux at all, but instead en-
 1233 tirely "misses" Europa's atmosphere. Upon encountering the outer edge of the moons
 1234 ramside magnetic pileup region near $x \approx -4R_E$ (see panels 3(g) and 8(d)), the parent
 1235 ion's pitch angle is shifted away from 90° by the mirror force in the enhanced \mathbf{B} field.
 1236 Then, the proton rapidly propagates into the $z < 0$ half space and passes the moon at

1237 large southern Jovian latitudes (i.e., outside of the plotted domain). Similar deflection
 1238 of many such ions thus contributes to the reduction of the ENA flux intensity in draped
 1239 fields.

1240 For both uniform and draped fields, the morphology of the detectable ENA emis-
 1241 sion patterns (see Figure 5) varies only slightly across different energies. However, the
 1242 ENA flux *intensity* depends non-monotonically on the parent protons' initial energy. Within
 1243 the range studied, the intensity of the detected ENA flux is smallest at an initial pro-
 1244 ton energy of 1 keV (row 5(a-b)), peaks at 40 keV (row 5(e-f)), and subsequently falls
 1245 off with increasing energy. At initial parent proton energies of 1 keV (see panels 5(a) and
 1246 (b)), the maximum detected ENA flux is less than 5% of the maximum value detected
 1247 for parent protons initialized at 40 keV. At initial energies of 100 keV, the maximum ENA
 1248 flux detected has again fallen and is now about 60% of its value for 40 keV parent pro-
 1249 tons (see panels 5(i) and (j)).

1250 The intensity $\tilde{I}(E)$ of energetic proton flux measured outside of Europa's interac-
 1251 tion region first increases with energy, reaches a maximum around 60 keV, and then falls
 1252 off again at higher energies (see section 2.2 and Paranicas et al. (2002)). The value of
 1253 $\tilde{I}(E)$ is more than a factor of 10 greater at the upper edge of our energy regime (100 keV)
 1254 than at its lower edge (1 keV). The cross section $\sigma(E)$ for charge exchange between pro-
 1255 tons and molecular oxygen decreases monotonically as a function of increasing parent
 1256 ion energy (see Figure 2). According to equation (20), the intensity of ENA emissions
 1257 generated by a parent ion of energy E is dependent on the product of $\tilde{I}(E)$ and $\sigma(E)$.
 1258 Therefore, the non-monotonic behavior of $\tilde{I}(E)$ –combined with the steady decrease of
 1259 $\sigma(E)$ – maps into the ENA emission patterns, causing the flux through the detector to
 1260 peak in our 40 keV model scenario.

1261 We now discuss the global morphology of ENA emissions at Europa when the moon
 1262 is located at its maximum distance below the center of the Jovian plasma sheet. In this
 1263 setup, the ambient magnetospheric field possesses a nonzero horizontal component \mathbf{B}_h .
 1264 Therefore, the induced field from Europa's subsurface ocean (see equation (1)) now in-
 1265 fluences parent ion dynamics in the moon's vicinity. To isolate the impact of the induced
 1266 field on the ENA emissions, we calculate emission maps (at all five initial energies) for
 1267 an additional case where the ambient magnetic field is obtained by superimposing the
 1268 uniform magnetospheric background field \mathbf{B}_0 and the induced dipole field, but *without*

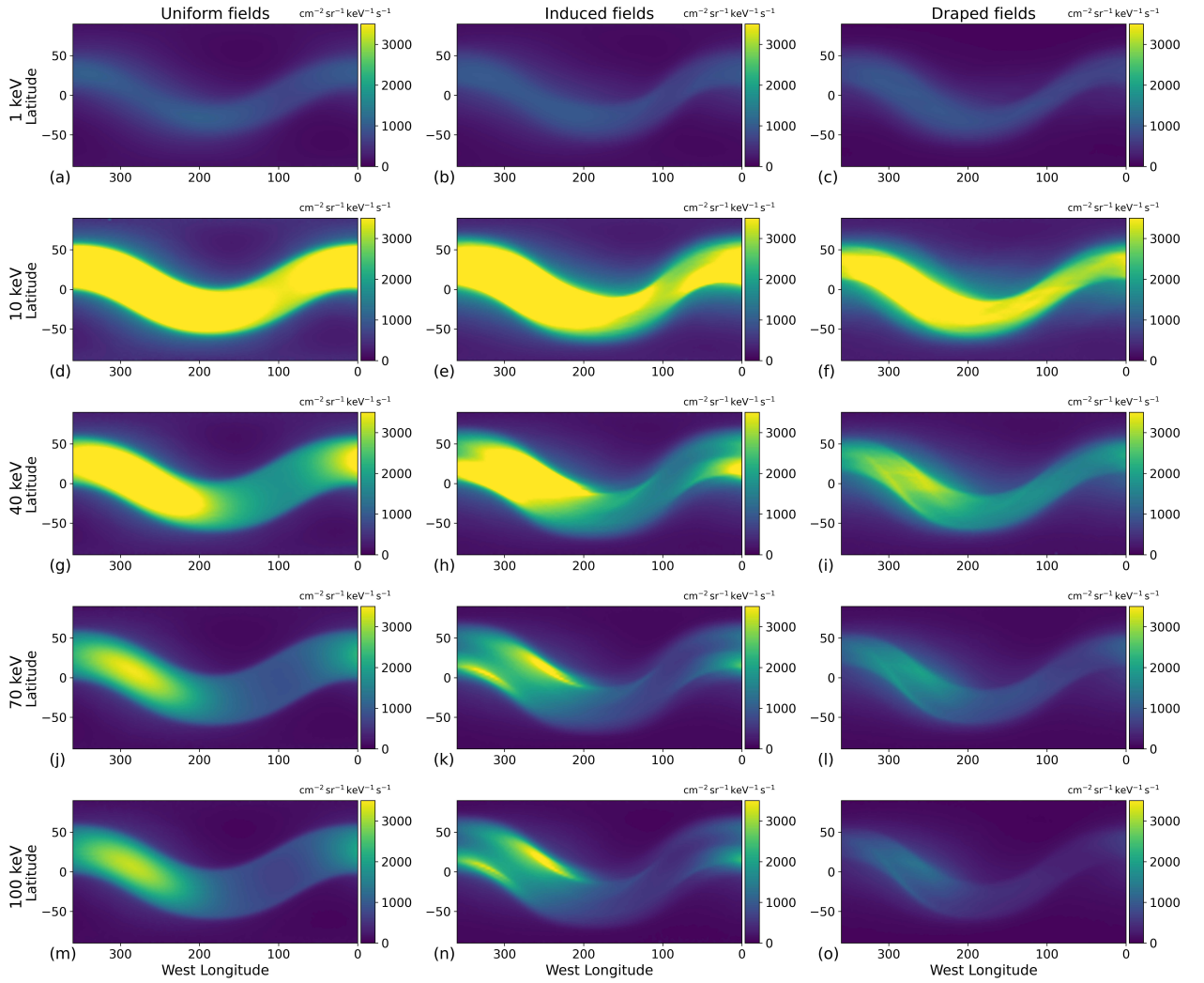


Figure 9. Global ENA flux maps from Europa when at its maximum distance below the center of the Jovian plasma sheet. The spherical detector is again concentric about the moon and located at $|\mathbf{r}| = 2R_E$. Analogous to Figure 5, each row represents ENA emissions generated by parent ions initialized at a certain kinetic energy, namely 1 keV in row (a-c), 10 keV in row (d-f), 40 keV in row (g-i), 70 keV in row (j-l), and 100 keV in row (m-o). Moving from left to right, the columns display the ENA flux maps in uniform magnetospheric background fields (panels (a), (d), (g), (j), and (m)), uniform magnetospheric fields superimposed with Europa's induced dipole (panels (b), (e), (h), (k), and (n)), and including the contribution of currents from the plasma interaction (panels (c), (f), (i), (l), and (o)). The color scale is identical to that used in Figure 5 to facilitate comparison.

including any plasma effects. In Figure 9, we present the ENA fluxes calculated for each of the three model field configurations, i.e., the uniform background field alone (left column), the uniform background field superimposed with Europa's induced dipole (center column), and the perturbed electromagnetic fields resulting from the plasma interaction with Europa's ionosphere and induced dipole (right column).

In contrast to ENA emissions at the center of the plasma sheet, in Figure 15 the band of high ENA flux is clearly discernible for all initial proton energies in draped fields.

1276 Although the width of the high flux band remains the same as it was at the center of
 1277 the plasma sheet (left column of Figure 5), the band now shows a sinusoidal variation
 1278 as a function of longitude. This apparent “waviness” of the band is generated solely by
 1279 the chosen projection in the plots: the band is still circular and present across all lon-
 1280 gitudes, centered in latitude around the great circle perpendicular to the magnetospheric
 1281 background field \mathbf{B}_0 . In contrast to the scenario from Figure 5, the background field is
 1282 no longer aligned with the ($-z$) axis but possesses a strong component toward Jupiter
 1283 (see Table 1). The high-flux band is mainly generated by parent ions with pitch angles
 1284 near 90° . Hence, the tilt of the background field against the north-south direction in-
 1285 herently rotates the gyroplanes of these parent ions. This results in an analogous rota-
 1286 tion of the high flux band on the detector sphere (see also Figure 6 of Tippens et al., 2022).
 1287 The maximum latitudinal deviation of the band’s center from 0° is thus approximately
 1288 equal to the tilt of the background magnetospheric field against the z axis: 28.5° (par-
 1289 ticularly visible in panels 9(d), (g), and (j)).

1290 At all five initial proton energies studied, the intensity of ENA emissions at max-
 1291 imum distance below the Jovian plasma sheet is persistently greater than in the corre-
 1292 sponding field configuration (uniform or draped) at the center of the sheet. In panels 9(d),
 1293 9(g), and 9(j), ENA flux detected within the band is at or above $3500 \text{ [cm}^2 \text{ sr keV s]}^{-1}$
 1294 across the entire ramside hemisphere of the detector. In the analogous case at the cen-
 1295 ter of the plasma sheet, the ENA flux only reaches this value within a tightly confined
 1296 region of the band. Besides, such high values occur only at an initial proton energy of
 1297 40 keV (see left column of Figure 5), i.e., near the peak of the ambient proton flux $\tilde{I}(E)$.
 1298 For instance, panel 9(g) demonstrates that in uniform fields, a flux of over $3500 \text{ [cm}^2 \text{ sr keV s]}^{-1}$
 1299 is detected across a longitudinal width of 185° (from 200° W to 25° W) inside the band,
 1300 compared to a longitudinal width of only 85° at the center of the plasma sheet (see panel
 1301 5(e)). The intensity $\tilde{I}(E)$ of the energetic proton flux observed outside of Europa’s in-
 1302 teraction region is elevated by about a factor of 3 at initial energies $E = 1 \text{ keV}$, $E =$
 1303 10 keV , and $E = 40 \text{ keV}$ when moving away from the center of Jupiter’s plasma sheet
 1304 (Paranicas et al., 2002, see their panel 2(a)). This drives the enhancement of ENA flux
 1305 at the lower half of our energy range, compared to the center of the plasma sheet (Fig-
 1306 ure 5 versus Figure 9).

1307 As can be seen from the middle column of Figure 9, the induced dipole field (in iso-
 1308 lation) plays a minor role in influencing the intensity and shape of ENA emissions at Eu-

1309 ropa. The rather subtle effect of the dipole is revealed by comparing, e.g., panels 9(g)
 1310 and 9(h): a portion of the high-flux region in panel 9(g) is “cut away” by the dipole (see
 1311 panel 9(h)), and the ENA flux within the wakeside band drops by about 15%. Besides,
 1312 comparing panels 9(j) and 9(k) illustrates that in uniform fields, the region of maximum
 1313 flux (about $3500 \text{ [cm}^2 \text{ sr keV s]}^{-1}$) is confined to the center of the band, whereas this value
 1314 is only reached within a thin segment near the band’s edges when the induced dipole field
 1315 is included.

1316 In the case of draped fields (right column of Figure 9), the intensity of ENA emis-
 1317 sions everywhere on the detector is reduced by approximately 40% at initial proton en-
 1318 ergies from $10 - 70 \text{ keV}$ compared to uniform fields, and by about 60% at 100 keV . Be-
 1319 low the center of the plasma sheet, the band of high flux still encloses the entire detec-
 1320 tor sphere when draping is included. When Europa is at the center of the Jovian plasma
 1321 sheet, the magnitude of the magnetic field reaches $1.7|\mathbf{B}_0|$ in the ramside pileup region,
 1322 compared to only $1.3|\mathbf{B}_0|$ far outside the sheet (see panels 3(g) and (h)). This reduced
 1323 magnetic field pileup upstream of Europa is less effective in diverting impinging parent
 1324 ions away from the moon, thereby having slightly less effect on the ENA emission mor-
 1325 phology than at the center of the sheet.

1326 Regardless of Europa’s distance to the center of the Jovian plasma sheet, a space-
 1327 craft on a polar flyby is likely to observe a much weaker ENA flux from the atmosphere
 1328 than one viewing the interaction from slightly west of the ramside pileup region within
 1329 the moon’s equatorial plane. Field line draping –which renders additional “protection”
 1330 to Europa’s polar atmosphere– is substantially weaker below the center of the Jovian plasma
 1331 sheet compared to within it (see Table 1): perturbations in B_x are only about half the
 1332 magnitude of those in the center case (see panels 3(c) and 3(d)). This increases the ac-
 1333 cessibility of energetic protons to the moon’s atmosphere (see also Addison et al. (2021)),
 1334 contributing to the overall enhancement in ENA flux through the detector. The empir-
 1335 ical model for the thermal magnetospheric plasma density utilized in this study predicts
 1336 a density value of $n_0 = 200 \text{ cm}^{-3}$ at the center of the Jovian plasma sheet, and a den-
 1337 sity of $n_0 = 40 \text{ cm}^{-3}$ at maximum distance below (Roth, Retherford, et al., 2014). How-
 1338 ever, Bagenal and Delamere (2011) suggest a much less oscillatory upstream density at
 1339 Europa, ranging from 50 cm^{-3} at the center to 37 cm^{-3} at Europa’s maximum distance
 1340 from the center. Both values provided by Bagenal and Delamere (2011) are sim-
 1341 ilar to the value used in our study for Europa at its maximum distance below the cen-

1342 ter of the Jovian plasma sheet, where the draping generates only minor modifications
 1343 to the ENA flux pattern (see Figure 9). In other words, when using the upstream den-
 1344 sity values from Bagenal and Delamere (2011) the features in the ENA flux morphology
 1345 at the center of the plasma sheet would be more similar to those from below the sheet
 1346 than suggested by our results (see Figure 9).

1347 **3.3 ENA Emissions at Europa with an Anisotropic Pitch Angle Distri-**
 1348 **bution**

1349 Figure 10 displays the global ENA emissions through the detector sphere when Eu-
 1350 ropa is located at the center of the Jovian plasma sheet, with two different PADs used
 1351 to initialize the parent protons on the starting grid. In both cases, the ENA flux maps
 1352 have been calculated using the draped fields from AIKEF, and the model results for an
 1353 isotropic PAD (see Figure 5) are shown again in the left column to aid comparison. ENA
 1354 emissions generated by parent protons with an anisotropic PAD (see equations (10) and
 1355 (12)) are given in the center column. The maps in the right column have been gener-
 1356 ated by subtracting the ENA flux maps for an anisotropic PAD (center column) from
 1357 those calculated with an isotropic PAD (left column) at each respective initial parent
 1358 ion energy. Positive values (red) then show regions where the anisotropic PAD *weakens*
 1359 the detectable ENA flux, and negative values (blue) display where the anisotropic PAD
 1360 *enhances* the ENA flux.

1361 With the anisotropic PAD, the qualitative morphology of ENA flux through the
 1362 detector is highly similar to the case of an isotropic PAD. In both instances, an enhance-
 1363 ment in ENA flux is formed near the detector's ramside apex, and a narrow band of slightly
 1364 elevated ENA flux along the equator can be seen at the wakeside (left and center columns
 1365 of Figure 10). Since \mathbf{B}_0 is aligned with the $(-z)$ axis, both features are approximately
 1366 symmetric about the detector's equator. Within the emission enhancement formed around
 1367 the ramside apex, the ENA flux detected with the anisotropic PAD is elevated by no more
 1368 than 7% compared to the isotropic case (see right column of Figure 10). At all initial
 1369 proton energies above 1 keV, the anisotropic PAD slightly elevates the ENA flux at mid-
 1370 latitudes, i.e. directly north and south of the central band.

1371 The initial velocity and position coordinates for the energetic protons launched on
 1372 the starting grid are the same for both PADs; only the initial numerical weights J of the

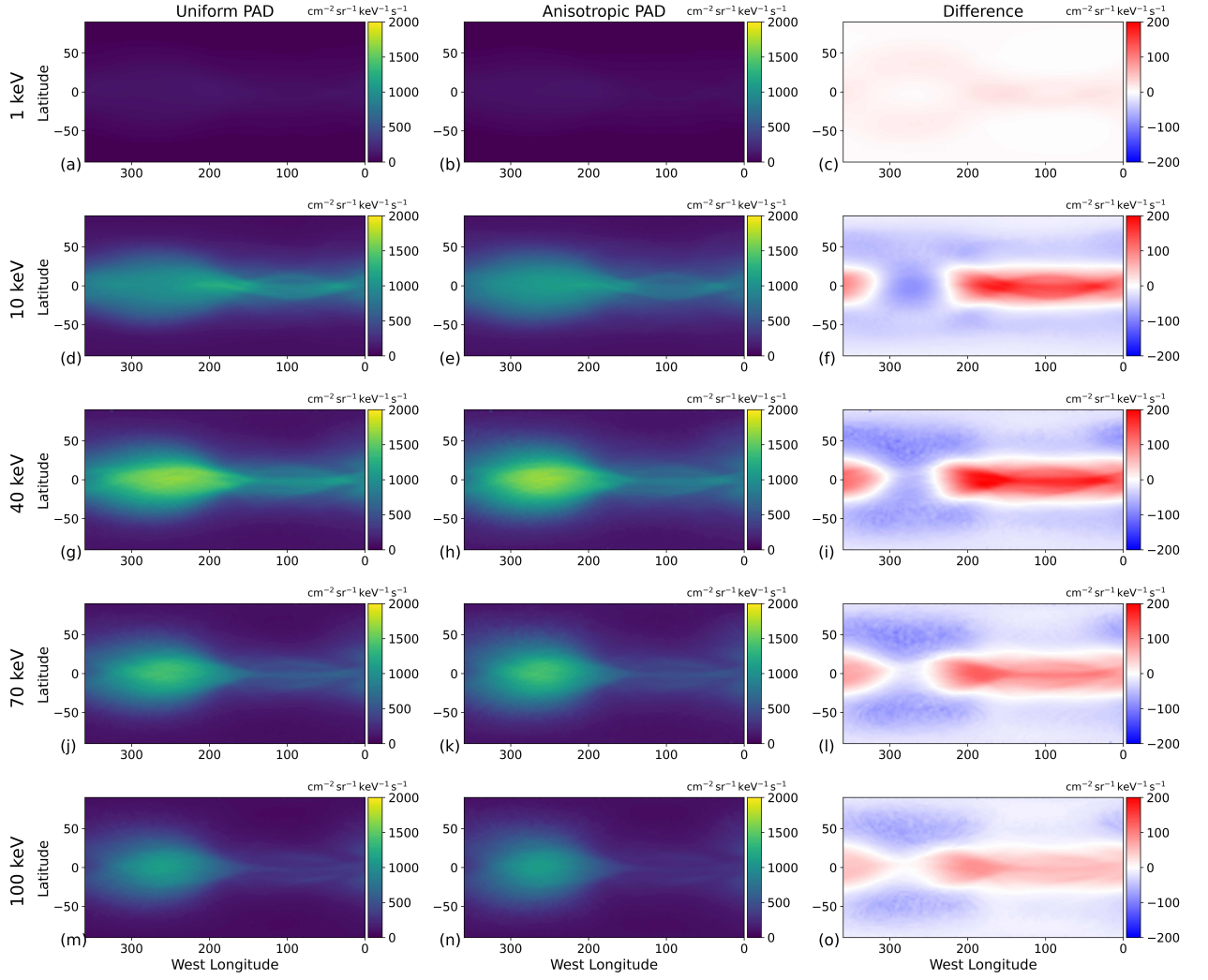


Figure 10. Influence of an anisotropic PAD on the global ENA emission morphology at Europa when situated at the center of the Jovian plasma sheet. The figure layout is analogous to that of Figure 5, where each row represents an initial parent proton energy. The left column displays the ENA flux with an isotropic PAD in draped electromagnetic fields (panels (a), (d), (g), (j), and (m)) to facilitate comparison, also shown in the right column of Figure 5. The center column (panels (b), (e), (h), (k), and (n)) displays detected ENA flux in the same field configuration, but using the anisotropic PAD given by equation (10). The right column (panels (c), (f), (i), (l), and (o)) then shows the difference between the detected ENA flux with an isotropic (left column) and with an anisotropic (center column) PAD, i.e., the left column minus the center column. The white regions in maps of the right column correspond to locations on the detector toward which the isotropic and anisotropic PAD emit the same detectable ENA flux. Red (positive) or blue (negative) indicate regions where the isotropic or anisotropic PAD generate more detectable ENA flux, respectively. Note that the range of the right column's colorscale is reduced relative to the scale used in the left and center columns.

parent protons differ between the isotropic and anisotropic PAD population. Therefore,
 1374 the inclusion of an anisotropic PAD can only alter the intensities of the ENA flux through
 1375 certain regions of the detector, but it does not change the overall pattern of the detected
 1376 flux since the atmospheric accessibility is not altered by changes to the PAD. The anisotropic
 1377 PAD assigns a higher differential flux J to parent protons with pitch angles near 0° and
 1378 180° than to protons with $\alpha \approx 90^\circ$. Using equations (8)–(11) reveals that the parent

1379 protons initialized with a pitch angle α between $\arcsin \frac{\pi}{4} \approx 52^\circ$ and $180^\circ - \arcsin \frac{\pi}{4} \approx$
 1380 128° carry *less* flux with the anisotropic PAD than the same protons initiated with an
 1381 isotropic PAD. Thus, for the ENA flux to be lower in a certain region of the detector with
 1382 the anisotropic PAD (i.e., red regions in the right column of Figure 10), the ENA flux
 1383 in that region must mainly stem from parent ions with initial pitch angles in the range
 1384 $52^\circ \leq \alpha \leq 128^\circ$. Conversely, the blue areas in the right column of Figure 10 imply
 1385 locations where the detector receives substantial ENA flux from parent ions with initial
 1386 pitch angles $\alpha \leq 52^\circ$ or $\alpha \geq 128^\circ$.

1387 For an anisotropic PAD, the detected ENA flux near the equator and away from
 1388 the ramside bulge is reduced in intensity by about $200 [\text{cm}^2 \text{sr keV s}]^{-1}$ (or 12%–18%, red
 1389 region in panels 10(f), (i), (l) and (o)) relative to the isotropic case at initial proton en-
 1390 ergies $E \geq 10 \text{ keV}$. The ENA flux within this region is mainly generated by parent pro-
 1391 tons with pitch angles near 90° (see section 3.2). This even holds at the detector’s wake-
 1392 side: protons initialized on the upstream face of the starting grid outside of Europa’s disk
 1393 (i.e., $\sqrt{y^2 + z^2} > R_E$) with $\alpha \approx 90^\circ$ emit ENAs towards the wakeside hemisphere wher-
 1394 ever the tangent to their helical trajectory intersects the detector sphere near its $x =$
 1395 $2R_E$ apex. The anisotropic PAD contains fewer particles with pitch angles around 90° ,
 1396 thereby causing the reduction in detected ENA flux (red band in the right column of Fig-
 1397 ure 10).

1398 At energies $E \geq 10 \text{ keV}$, the parent proton population initialized with an anisotropic
 1399 PAD emits a 20%–25% *greater* ENA flux towards mid-latitude regions on the detector,
 1400 located between $\pm 33^\circ$ and $\pm 80^\circ$ (blue in panels 10(f), (i), (l) and (o)). The ENA fluxes
 1401 in both scenarios again become similar when approaching the detector’s poles. For ex-
 1402 ample, at an initial energy of 40 keV , parent protons from an anisotropic PAD emit around
 1403 $50 [\text{cm}^2 \text{sr keV s}]^{-1}$ (or 23%) more ENA flux into the mid-latitude regions of the detec-
 1404 tor than protons with an isotropic PAD at the same energy (see panel 10(i)). This is most
 1405 visible in panels 10(i) and (l) on the detector’s upstream hemisphere. ENA flux through
 1406 the mid-latitude regions on the detector is mainly produced by parent ions that are ini-
 1407 tialized on the northern and southern faces of the starting grid with pitch angles around
 1408 0° (north) or 180° (south). These protons propagate with a field-aligned velocity that
 1409 is large compared to both the gyration velocity and drift velocity. ENAs generated by
 1410 these parent protons are mainly emitted along the magnetic field lines and can be de-
 1411 tected at all latitudes (see, e.g., panels 8(b) and (d)). Since the flux carried by parent

protons with pitch angles outside the range $52^\circ \leq \alpha \leq 180^\circ$ is higher for an anisotropic than for an isotropic PAD, the ENA flux through the mid-latitude regions of the detector is slightly elevated in the anisotropic case. Invoking the same mechanism, ENAs that travel toward the detector's polar caps are mainly generated by parent protons moving along magnetic field lines within Europa's disk $\sqrt{x^2 + y^2} \leq R_E$. However, such ENAs are intercepted by the moon's surface before they can reach the detector sphere and therefore, cannot contribute to the observable flux. For this reason, the flux through the detector's polar caps is equally low, regardless of the chosen PAD (white in Figure 10).

When switching from an isotropic PAD to an anisotropic PAD, the difference in ENA emission intensity at specific positions on the detector ranges from less than 0.1% to at most 35% at all initial proton energies above $E = 1$ keV. Globally, for parent protons initialized with an energy of, e.g., $E = 40$ keV, the integrated flux through the detector reads $3.52 \cdot 10^6$ [cm² keV s]⁻¹ with an isotropic PAD and $3.60 \cdot 10^6$ [cm² keV s]⁻¹ with the anisotropic PAD. Hence, including the anisotropic PAD only slightly increases the total signal at this energy. The region where the relative change peaks on the detector is located at the mid-latitudes ($\pm 66^\circ$), above and below the detector's ramside apex and colored in dark blue (panels 10(f), (i), (l), and (o)). Thus, the morphology of ENA emissions at Europa can only be used to constrain the ambient PAD if precise knowledge of the atmospheric structure, the upstream energetic proton distribution $\tilde{I}(E)$, and the draped magnetospheric field configuration is available.

3.4 ENA Emissions at Europa with a Localized H₂O Atmosphere

Figure 11 demonstrates the role that a localized H₂O atmospheric component (Roth, 2021), *in addition to* the primary molecular oxygen component, plays in influencing ENA emissions at Europa in draped fields when at the center of the Jovian plasma sheet. Both cases use the same, isotropic PAD to initialize parent protons on the starting grid. Displayed are the detectable ENA flux without the atmospheric H₂O component (left column), with the H₂O component included (center column), and the difference between the two maps at each energy (right column). Blue regions in the right column indicate where the detectable ENA emissions are elevated by the additional H₂O profile. The inclusion of the H₂O profile above the ramside apex results in a quantitative enhancement to the ENA emissions deposited in the low-latitude portion of the detector's ramside hemisphere, amplifying the bulge-like feature in the ENA emissions already present for a pure

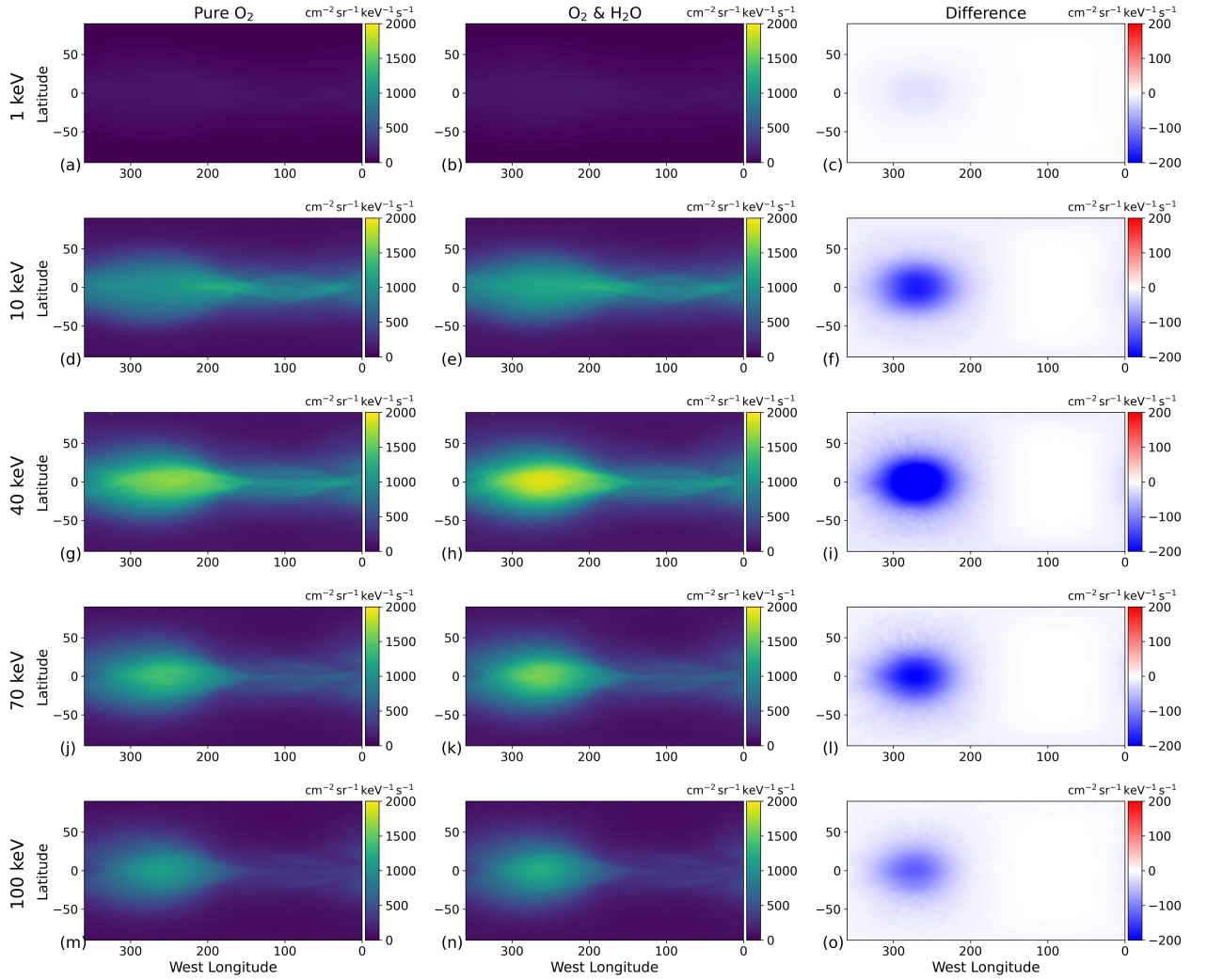


Figure 11. Influence of a localized atmospheric H_2O component around Europa's ramside apex on the global ENA emission maps at the center of the Jovian plasma sheet. The ENA flux is displayed analogously to Figures 5, 9, and 10, where each row represents an initial parent ion energy. The left column again displays the ENA flux in draped electromagnetic fields (adopted from Figure 5) without the neutral H_2O component (panels (a), (d), (g), (j), and (m)). The center column (panels (b), (e), (h), (k), and (n)) displays detected ENA flux in the slightly modified draped fields (see Figure 4), now including ENA generation through interaction with the additional H_2O component. The right column (panels (c), (f), (i), (l), and (o)) then shows the difference between the detected ENA flux with a purely O_2 atmosphere (left column) and an atmosphere including both the O_2 and the H_2O component (center column). The white regions in the right column correspond to locations where the detected ENA flux is identical with and without the H_2O included. Regions in red show where the ENA flux through the detector is higher *without* the atmospheric H_2O , and regions in blue show where the detector receives higher ENA flux from an atmosphere including both O_2 and H_2O . Note that the scale of the right column covers a much narrower range of values than the scale used in the left and center columns.

O₂ atmosphere. For example, at an initial parent proton energy of $E = 40 \text{ keV}$, the ENA flux maximum without the H_2O profile included is $285 [\text{cm}^2 \text{sr keV s}]^{-1}$ (or 17% weaker than with the H_2O included (see panels 11(g), (h) and (i))).

The presence of the H_2O exosphere only slightly alters the draped field configuration near Europa (see section 3.1 and Figure 4). Therefore, energetic parent protons

1449 are granted access to Europa's atmosphere in a very similar fashion to the configuration
 1450 that only includes an O₂ component. Thus, the ENA emission morphology shares a strong
 1451 resemblance between the two cases: differences are confined to the region of the detec-
 1452 tor above the confined H₂O profile. Since energetic proton gyroradii at Europa are 1 –
 1453 2 orders of magnitude smaller than the moon's radius (see Table 2), absorption by Eu-
 1454 ropa makes the detector's wakeside hemisphere largely inaccessible to ENAs generated
 1455 near the ramside apex. The charge exchange cross section between protons and H₂O (sim-
 1456 ilar to protons and O₂) decreases steadily with increasing energy (see Figure 2). Con-
 1457 sidering that the ambient differential proton flux peaks around 60 keV, the detected ENA
 1458 flux at Europa (both with and without the water vapor) is therefore weakest at an ini-
 1459 tial energy of 1 keV, peaks in the model results at an initial energy of 40 keV, and then
 1460 falls off monotonically with increasing initial energy (see left and center columns of Fig-
 1461 ure 11).

1462 The number density in Europa's ramside atmosphere is elevated by up to 43% with
 1463 the additional H₂O profile included, but the ENA flux around the detector's ramside apex
 1464 is kept below a 20% increase at all energies studied. As parent ions propagate through
 1465 the (now denser) atmosphere, their numerical weight is attenuated by the two neutral
 1466 species more rapidly than by the O₂ component alone. Therefore, while a proton trav-
 1467 eling through the combined O₂/H₂O atmosphere may produce more ENAs at higher al-
 1468 titudes than with O₂ alone, its ability to generate ENAs in the more dense lower atmo-
 1469 sphere is reduced. Thus, the quantitative changes to the ENA flux between both cases
 1470 are rather subtle, and the detection of such a confined neutral profile at Europa would
 1471 rely upon highly constrained upstream parameters in tandem with direct knowledge of
 1472 the energetic proton flux.

1473 In addition to a persistent H₂O atmosphere around Europa's ramside apex, sev-
 1474 eral remote and in-situ observations have revealed localized, transient plumes of H₂O va-
 1475 por emanating from Europa's surface (e.g., Roth, Saur, et al., 2014; Jia et al., 2018; Arnold
 1476 et al., 2019). Plumes generate a localized number density near the surface that is only
 1477 about a factor of 4 larger than the atmospheric H₂O density used in this study (Roth,
 1478 Saur, et al., 2014; Roth, 2021). The scale height of the H₂O density in such a plume is
 1479 estimated to be approximately 200 km (e.g., Arnold et al., 2019), i.e., only slightly larger
 1480 than those of the persistent O₂ and H₂O components. Thus, our results from Figure 11
 1481 suggest that such a plume would manifest at Europa only through a subtle quantitative

enhancement of the detected ENA flux above its source region. Such a feature would likely be difficult to discern from the “background” ENA emissions generated by protons that undergo charge exchange with the O₂ and H₂O components of the moon’s global atmosphere.

3.5 Variability of ENA Emissions at Callisto

In Figure 12, we present maps of the ENA flux through a concentric spherical detector of radius $2 R_C$ around Callisto when the moon is at the center of the Jovian plasma sheet. The layout of Figure 12 is analogous to that of Figure 5, with the left and right columns presenting the detectable ENA flux in uniform and draped electromagnetic fields, respectively. Again, each row corresponds to a distinct initial energy of the parent protons. When Callisto is at the center of the Jovian plasma sheet, the magnetospheric field in the vicinity of the moon is oriented approximately southward, and therefore we do not include an induction signal in this treatment (see Table 1). Since the strength of the magnetospheric field at the center of the plasma sheet falls around two orders of magnitude when moving outward from Europa to Callisto, the parent proton gyroradii at Callisto are approximately two orders of magnitude larger at each respective initial energy, becoming comparable to or larger than $1 R_C$. For instance, at $E = 10 \text{ keV}$, the gyroradius of a proton with $\alpha = 90^\circ$ is $1.5 R_C \approx 3,615 \text{ km}$ at Callisto but only $0.02 R_E \approx 31 \text{ km}$ at Europa.

As with Europa, we investigate the (hypothetical) case when Callisto is in uniform magnetospheric fields in order to obtain a baseline understanding of the ENA emission patterns. For this scenario, the bulk of the detectable ENA flux is focused onto the equatorial region of the detector (left column of Figure 12). This band of high flux is most distinct in panels 12(c), (e) and (g). The equatorial band wraps around Callisto normal to the orientation of the magnetospheric background field, and its latitudinal extension can again be estimated using equation (21) and the scale height $h_{O_2,C} = 230 \text{ km}$ of the moon’s molecular oxygen envelope. We determine an estimate of $\theta_b = 33.2^\circ$ for the half-width of the band, which is similar to the latitudinal extent of the modeled band on the detector (about $\theta_b \approx 36^\circ$; see, e.g., panel 12(e)).

The boundary of the high flux band at Callisto appears blurred when the moon is at the center of the Jovian plasma sheet. Regions receiving significant flux on the de-

1513 detector reach outside of the estimated boundaries of the band up to latitudes of $\pm 55^\circ$, par-
 1514 ticularly visible as the yellow region in panel 12(c). At Europa, the band of high ENA
 1515 flux has sharply pronounced latitudinal boundaries because parent protons with pitch

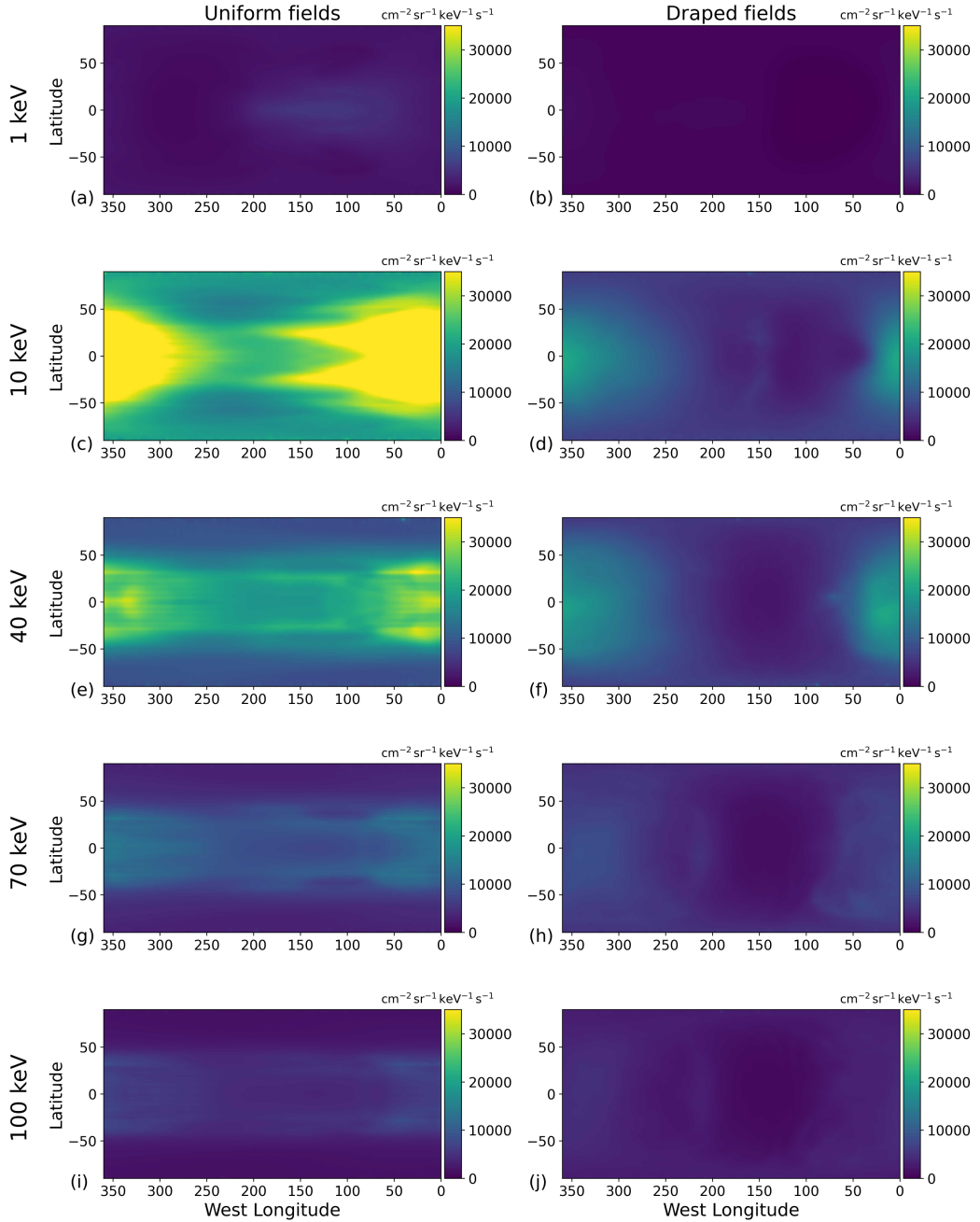


Figure 12. Global ENA emission flux maps at Callisto through a spherical detector centered at the origin with radius $2R_C$. In this setup, Callisto is located at the center of the Jovian plasma sheet (see Table 1). The figure is arranged in the same manner as Figure 5. The left and right columns show results for uniform and perturbed electromagnetic fields, respectively. Note that the colorscale covers a much broader range here than the scales used in Figures 5 and 9.

1516 angles near 90° trace much longer paths through the atmosphere than those that largely
 1517 travel along the magnetospheric field lines (see section 3.2). This difference in path lengths
 1518 stems from the fact that, due to the small gyroradii, parent protons can complete many
 1519 gyrations within Europa's atmosphere. In contrast, when Callisto is at the center of the
 1520 plasma sheet, even the gyroradii of 1 keV protons exceed the atmospheric scale height
 1521 $h_{O_2,C}$ by a factor of 5. Therefore, ENA generation from individual proton macroparti-
 1522 cles is limited to small contributions from partial gyrations within the atmosphere. The
 1523 left column of Figure 13 illustrates the trajectories of two protons that spend only a small
 1524 portion of their gyrations within the atmosphere. Both protons are initiated with an en-
 1525 ergy of 10 keV and a pitch angle of $\alpha = 90^\circ$ upstream of the moon. They propagate
 1526 through uniform electromagnetic fields, remain confined to the $z = 0$ plane (panel 13(b)),
 1527 and complete two partial gyrations within the atmosphere, each before impacting Cal-
 1528 listo. Each of these protons travels a total path length through the atmosphere of no more
 1529 than one gyration circle, i.e., $2\pi r_g \approx 6.3R_C$ (see panel 13(a)). This length is compa-
 1530 rable to the longest possible path of a proton with $\alpha = 0^\circ$ through the atmosphere in
 1531 uniform fields: $2\sqrt{3}R_C$, or the distance a proton travels along a magnetic field line tan-
 1532 gent to Callisto's surface while within the detector sphere. This example demonstrates
 1533 why the band (bounded by latitudes $\pm 36^\circ$) contains only 50% – 60% of the total detectable
 1534 ENA flux at each initial parent ion energy at Callisto (see left column of Figure 12). In
 1535 comparison, over 80% of the total detectable ENA flux was concentrated inside the band
 1536 at Europa (see left column of Figure 5).

1537 Across the studied energy range, the detectable ENA flux in uniform fields is max-
 1538 imized slightly downstream of the detector's Jupiter-facing apex. The minimum flux within
 1539 the band is detected slightly upstream of the Jupiter-averted apex (see, e.g., panel 12(c)).
 1540 For example, at an initial parent proton energy of 40 keV, the ENA flux reaches its max-
 1541 imum of over 37,000 [cm² sr keV s]⁻¹ at 24° W longitude near the northern edge of the
 1542 band. The minimum flux detected *within* the band at the same energy is only 45% the
 1543 intensity of the maximum, and it is clustered around approximately 200° W longitude.
 1544 In contrast to this, the maxima and minima of the ENA flux in uniform fields at Europa
 1545 occur close to the detector's ramside and wakeside apices, respectively (see Figure 5).

1546 To understand the locations of the ENA flux extrema at Callisto, we consider again
 1547 the energetic proton trajectories (solid and dashed lines) depicted in Figure 13(a). Of
 1548 the detectable ENA flux produced by the sample proton initialized in the $y < 0$ half

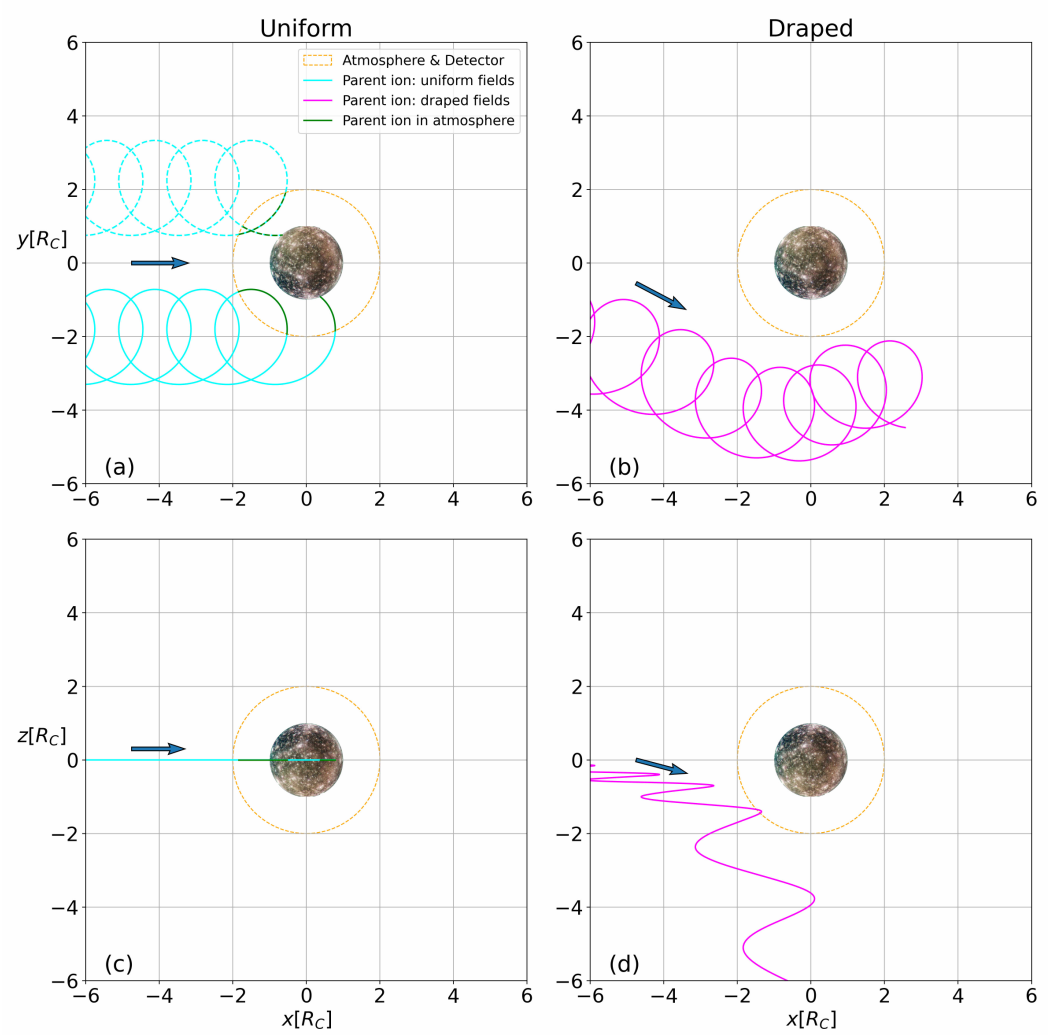


Figure 13. Two-dimensional projections of three representative parent proton trajectories through Callisto's electromagnetic environment. Each parent proton is initialized at an energy of $E = 10$ keV and travels through either uniform fields (panels (a) and (c)) or perturbed fields (panels (b) and (d)). Projections of the proton trajectories onto the $z = 0$ and the $y = 0$ planes are displayed in the top and bottom rows, respectively. The coloring is analogous to Figures 7 and 8, using light blue for the parent proton traced in uniform fields, magenta for the parent proton in draped fields, and green when either trajectory is embedded within the atmosphere (i.e., $|\mathbf{r}| \leq 2R_C$) and emitting ENAs. The parent protons with a solid trajectory are propagated from outside of the plot window through both uniform and draped fields, with an initial position given by $\mathbf{r}(t = 0) = (-10 R_C, -3.3 R_C, 0 R_C)$ and an initial velocity of $\dot{\mathbf{r}}(t = 0) = (\sqrt{\frac{2E}{m_p}} \sin 90^\circ, 0, -\sqrt{\frac{2E}{m_p}} \cos 90^\circ) = \sqrt{\frac{2E}{m_p}} \hat{\mathbf{x}}$. The parent proton with the dashed trajectory (visible only in panel (a)) is propagated through uniform fields only with an initial position of $\mathbf{r}(t = 0) = (-10 R_C, 3.3 R_C, 0 R_C)$ and an initial velocity equal to $\dot{\mathbf{r}}(t = 0) = \sqrt{\frac{2E}{m_p}} \hat{\mathbf{x}}$. In the $y = 0$ plane (panel (c)), the trajectory of this proton overlaps with that of the particle launched at $y < 0$. For the sake of clarity, the corresponding trajectory in draped fields is not displayed. The blue arrows again show an approximate bearing of the guiding center motion as the trajectory enters the panel frame.

space (solid line), the ENA flux emitted during the first trajectory segment within the atmosphere (solid green line) is mostly directed towards the Jupiter-facing, upstream quadrant of the detector. The flux generated during the proton's second incursion into the atmosphere is absorbed by Callisto. A complementary proton trajectory initialized in the $y > 0$ half space also completes two partial gyrations within the atmosphere (dashed

green line). During the first trajectory segment within the atmosphere, this proton only emits detectable ENAs towards the $y > 0$ half space. During the second segment, all its emitted ENAs are absorbed by Callisto. This example suggests that protons with pitch angles near 90° emit detectable ENA flux preferentially toward the Jupiter-facing hemisphere of the detector irrespective of their initial y coordinate, due to the direction of their gyration and their large gyroradii (see panels 12(c), (e), and (g)). If the ambient magnetospheric field orientation were inverted, ENAs would preferably be emitted into the $y < 0$ half space. If the ambient magnetic field magnitude were enhanced, the rotation of the extrema in ENA flux away from the x axis would be weakened (see section 3.2). For this reason, the locations of the emission maxima/minima at Europa (where $|\mathbf{B}_0|$ is 1-2 orders of magnitude stronger) differ from those at Callisto.

Our modeled ENA emission patterns for Callisto are consistent with the findings of Tippens et al. (2022) at Titan for a southward magnetospheric field, where the energetic proton gyroradii are also comparable to the size of that moon. Using a similar model, these authors found the band of high ENA flux to persistently form normal to the ambient Kronian magnetospheric field, and they determined an enhancement of over 50% in the ENA flux intensity around the Saturn-facing apex of the detector compared to the Saturn-averted apex.

As shown in the right column of Figure 12, the observable ENA flux at Callisto is reduced in intensity by the field line draping, compared to a uniform southward field. The detected maximum in ENA flux remains near the Jupiter-facing apex when the plasma interaction is considered. Similar to the case of draped fields at Europa (see right column of Figure 5), formation of a band signature of elevated ENA flux along the equator does not occur. Instead, the ENA flux is now diminished in almost the entire Jupiter-averted hemisphere of the detector. When draped fields are included, this hemisphere receives at least 53% less ENA flux at all initial proton energies, compared to reductions by only 15%–40% in the Jupiter-facing hemisphere of the detector. Near the center of the Jovian plasma sheet, Callisto’s tail of ionospheric pickup ions is highly asymmetric due to their large gyroradii ($1\text{--}10 R_C$), extending several R_C into the Jupiter-averted half space (see panel 3(i) in this study and panel 2(e) of Liuzzo et al., 2022). The ram-side magnetic pileup region is “stretched” along the upstream flank of this pickup tail, thereby reaching several R_C into the Jupiter-averted hemisphere (Liuzzo et al., 2015, 2022). Deflection of the impinging parent ions by the field enhancement in the ramside pileup

region further diminishes the accessibility of Callisto's Jupiter-averted atmosphere to energetic protons. A sample trajectory that illustrates proton deflection by the stretched pileup region is displayed in the right column of Figure 13. Panel 13(b) demonstrates how the trajectory is deflected strongly in the ($-y$) direction when approaching Callisto, entirely avoiding the atmosphere and generating no ENA flux. In addition, this trajectory in uniform fields is confined to the $z = 0$ plane, but in draped fields the pileup deflects the proton out of the $z = 0$ plane (see panels 13(c) and (d)).

In both uniform and perturbed fields, the detectable ENA flux is minimized at an initial proton energy of 1 keV, peaks around 10–40 keV, and begins to fall off as energy increases beyond 40 keV (see Figure 12). For our studied proton energies, the detectable ENA flux reaches its peak value of $55,700 \text{ [cm}^2 \text{ sr keV s]}^{-1}$ in uniform fields at 10 keV. The differential proton flux outside of Callisto's interaction region peaks between 10–20 keV (see, e.g., Figure 3 of Liuzzo et al., 2022). The product $\sigma(E) \cdot \tilde{I}(E)$ maximizes at comparable initial proton energies, consistent with the behavior of intensity as a function of initial parent ion energy in our ENA emission maps.

At the center of the Jovian plasma sheet, the ENA emission intensity at Callisto exceeds that at Europa at each initial proton energy (in uniform and draped fields) by a factor of 20–40 (compare Figures 5 and 12). The ambient proton flux at Callisto's orbit differs from that observed at Europa by less than an order of magnitude across the studied energy interval (Paranicas et al., 2002; Liuzzo et al., 2022). Hence, the difference in ENA flux intensity is largely driven by the disparity in atmospheric density: Callisto's atmosphere possesses an O₂ column density 2–3 orders of magnitude greater than the column density of Europa's O₂ envelope (Cunningham et al., 2015; Liuzzo et al., 2015; Roth et al., 2016; Carberry Mogan et al., 2021; de Kleer et al., 2023). Parent protons interacting with Callisto's atmosphere encounter a higher local density and therefore generate more ENA flux than at Europa. In addition, the weaker ambient magnetic field at Callisto allows energetic parent ions to gyrate on much larger scales. As a result, protons whose guiding center trajectories do not even come close to intersecting Callisto's atmosphere may still penetrate into the moon's neutral envelope and produce ENAs. This is not the case at Europa.

This is further illustrated in Figure 14, displaying the energy dependence of proton gyroradii at (a) Europa and (b) Callisto in the uniform magnetospheric background

fields at the center of and below the Jovian plasma sheet. In contrast to Table 2, the gyroradii are now normalized to the atmospheric scale height at the respective moon. As can be seen, gyroradii at Europa remain smaller than or comparable to the scale height, regardless of the moon's distance to the plasma sheet. However, when Callisto is located at the center of Jupiter's plasma sheet, proton gyroradii in the weak magnetospheric field may exceed the scale height by more than an order of magnitude.

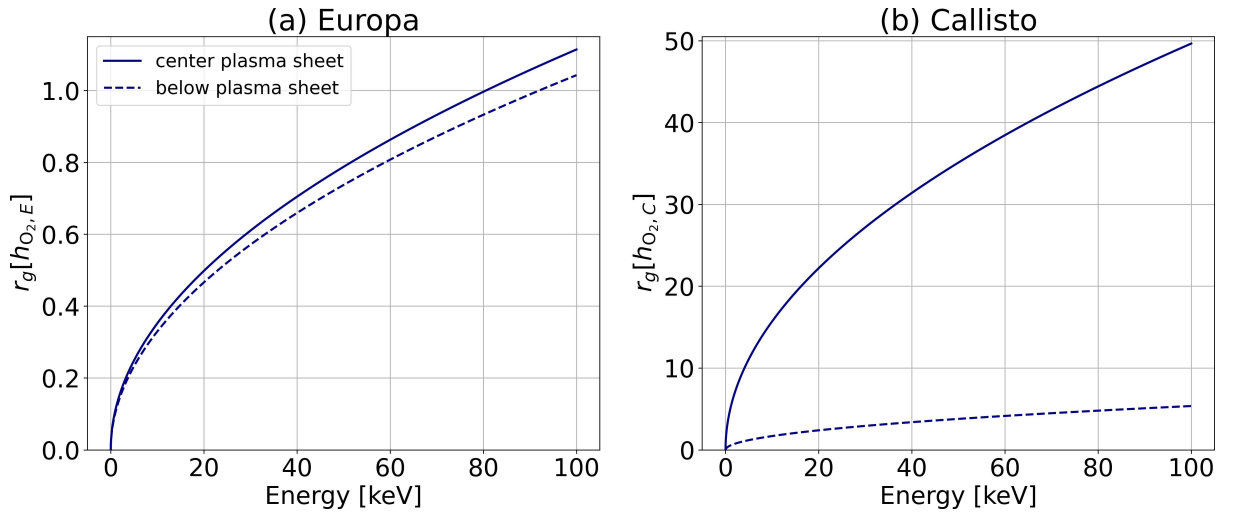


Figure 14. Proton gyroradii as a function of energy in the ambient magnetospheric background field \mathbf{B}_0 at (a) Europa and (b) Callisto. Gyroradius values are calculated assuming a pitch angle of $\alpha = 90^\circ$ and are normalized to the scale height of the molecular oxygen component in each moon's atmosphere. The solid and dashed curves denote gyroradii at the center and at maximum distance below the center of the Jovian plasma sheet, respectively.

In Figure 15, we present the ENA flux maps when Callisto is situated at its maximum distance below the center of the Jovian plasma sheet. Since the ambient magnetospheric field \mathbf{B}_0 is nearly parallel to the $z = 0$ plane and forms an angle of less than 17° against the y axis, we include an induced dipole moment at Callisto for this setup. Similar to section 3.2, we compare the detectable ENA emissions for a constant magnetospheric background field (left column), the constant background field superimposed with the induced dipole (center column), and the perturbed electromagnetic fields resultant from Callisto's interaction with the Jovian magnetosphere (right column). When Callisto is at its maximum distance below the sheet, the vast majority of ENA flux is again focused into a band of high flux on the detector, again centered about the great

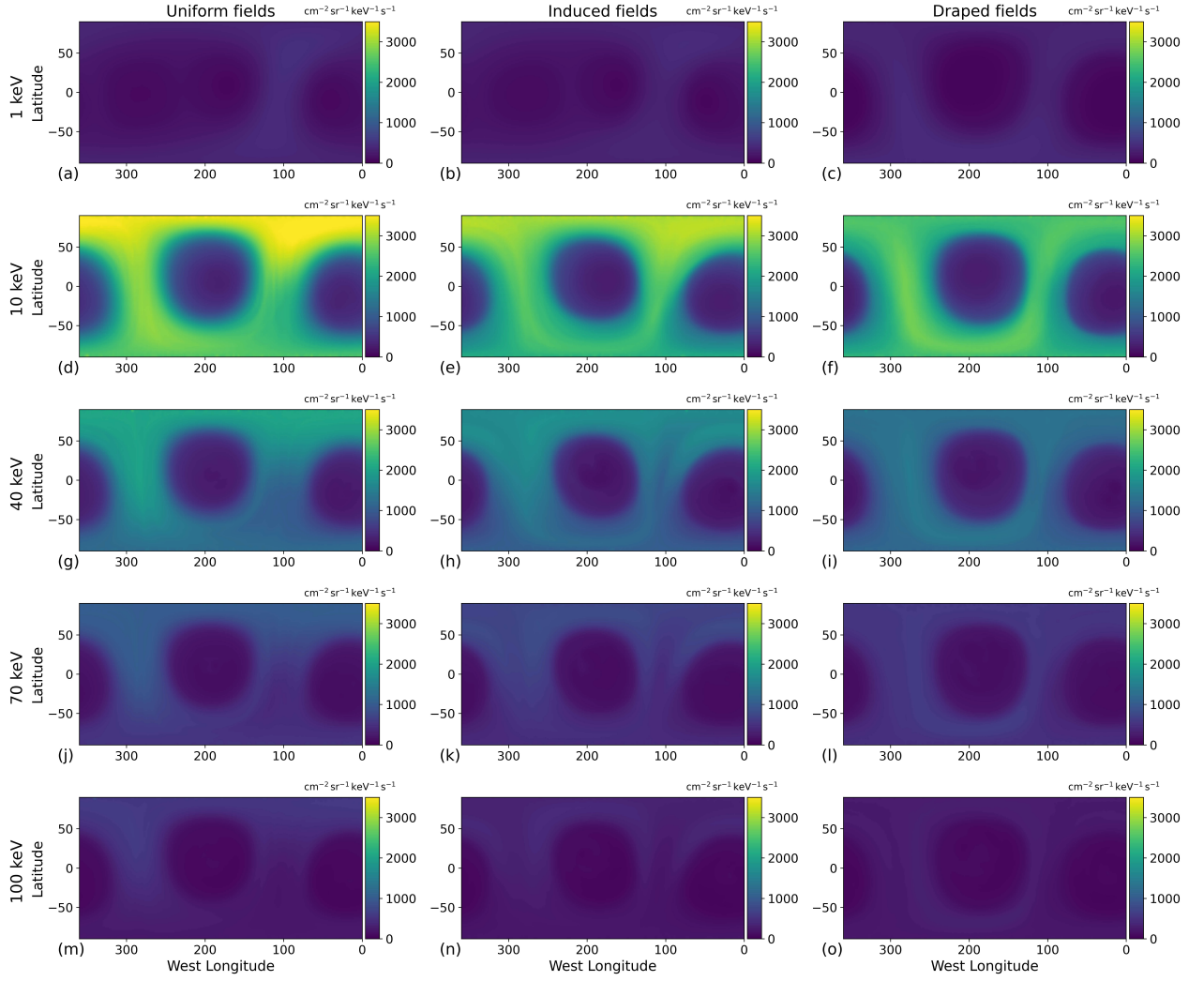


Figure 15. Maps of the ENA flux through a concentric spherical detector around Callisto when the moon is at its maximum distance below the center of the Jovian plasma sheet. See Figure 9 for details regarding the organizational structure. The range of the colorscale is equivalent to that used in Figure 9 to facilitate direct comparison between Europa and Callisto.

circle perpendicular to the background field, now wrapping around both geographic poles of the detector. The regions depleted of ENA flux are once again found above where the magnetospheric background field is largely normal to Callisto's surface. However, due to the magnetospheric field orientation, the flux is now depleted around the Jupiter-facing and Jupiter-averted apices (see Figure 15).

The regions near the north and south poles of the detector receive the highest ENA flux, and these two regions are connected by segments of the band centered around the meridional plane at approximately 100° and 280° W longitude. Outside of the band region, the detectable ENA flux falls by a factor of 3–9, similar to the spatial distribution

at Europa (see Figure 9). Moving away from the center of the plasma sheet, the strength of the background field at Callisto is enhanced by nearly a factor of 10 and thus energetic proton gyroradii (assuming $\alpha = 90^\circ$) range from $0.5h_{O_2,C} - 5.3h_{O_2,C}$, compared to $4.9h_{O_2,C} - 49.7h_{O_2,C}$ at the center of the sheet (see Table 2 and Figure 14). As a result, protons with pitch angles near 90° can complete a larger number of gyrations within the atmosphere, and the outer boundaries of the band become more sharply defined, as they are at Europa. In this configuration, the width of the meridional band is approximately $\theta_b \approx 37.5^\circ$ W longitude at the detector's equator where no latitudinal distortion occurs (see, e.g., panel 15(d)). This value is similar to the estimate of $\theta_b = 33.2^\circ$ provided by equation (21).

When at maximum distance below the Jovian plasma sheet, the ENA emission intensity at Callisto is again minimized around the initial proton energy $E = 1$ keV and increases drastically at 10 keV before falling off at higher energies. Following the approach of Liuzzo et al. (2022), we acquire the proton flux distribution $\tilde{I}(E)$ outside of Callisto's interaction region by scaling the distribution observed at the center of the plasma sheet with a factor of 1/10 at all energies to reflect magnetospheric migration to a substantially higher M shell value at Callisto's orbit (see section 2.2). The reduction in the ambient proton flux leads to a drop in overall ENA emission intensity by about an order of magnitude, compared to when at the center of the plasma sheet (see the upper limits of the color scales in Figures 12 and 15). Quantitative uncertainty in the ambient energetic proton distribution outside of the plasma sheet (see, e.g., Liuzzo et al., 2022) corresponds to analogous uncertainty in the magnitude of ENA emissions. However, the morphology of ENA emissions at a certain initial proton energy is robust to changes in the ambient proton distribution, since this distribution determines only the numerical weight of the proton macroparticles but not their motion through the electromagnetic fields.

When far from the center of the Jovian plasma sheet, the induced magnetic field at Callisto (in isolation) leaves the shape of the ENA emission patterns on the detector qualitatively unchanged. The differences in ENA emission maps without (left column of Figure 15) and with the induced field (center column of Figure 15) are highly localized and merely quantitative: only a slight attenuation of ENA flux intensity along with a subtle redistribution away from the edges of the high flux band toward its center occurs. This is most visible comparing the portion of the band near 100° W longitude in

1676 panels 15(g) and (h). Such a small quantitative change due to the induced field is con-
 1677 sistent with our findings at Europa (see section 3.2).

1678 Aside from a slight reduction in ENA flux across the entire detector, only minor
 1679 morphological adjustments to the ENA emission pattern are generated by field line drap-
 1680 ing. When Callisto is below the plasma sheet, the weak draping renders almost no pro-
 1681 tection to the atmosphere compared to when the moon is within the plasma sheet (see
 1682 panels 3(a), (b), (e), and (f)). As a result, the detectable ENA flux patterns shown in
 1683 the center and right columns of Figure 15 are highly similar. At Callisto, the variabil-
 1684 ity of the plasma interaction over a synodic rotation is large compared to that at Eu-
 1685 ropa (see Figure 3). Hence, this variability plays a greater role in influencing the mor-
 1686 phology of ENA emissions at Callisto: only at this moon does the appearance of the high
 1687 flux band change drastically between the “below” and the “center” case (see Figures 12
 1688 and 15). Further, the effect of the plasma interaction may be weakly discernible in de-
 1689 tectable ENA emissions emanating from Callisto’s atmosphere when the moon is far out-
 1690 side the Jovian plasma sheet.

1691 Though not yet directly confirmed through observations, the model of Carberry Mo-
 1692 gan et al. (2022) suggests the presence of an H₂ atmospheric component at Callisto which
 1693 is not included in our current model setup. Figure 11 of that study implies that this com-
 1694 ponent may have a column density comparable to that of O₂. Charge exchange cross sec-
 1695 tions between protons and molecular hydrogen (Tawara et al., 1985) are similar to those
 1696 for oxygen molecules, which would indicate a non-negligible contribution to ENA pro-
 1697 duction. Due to the lower mass, the scale height of the H₂ component would be elevated
 1698 compared to that of the O₂ included in our model. The presence of this component may
 1699 therefore increase ENA production at high altitudes (above the extension of the O₂ at-
 1700 mosphere). However, for a detector that encompasses Callisto’s *entire* atmosphere, the
 1701 ENA emission pattern would still be primarily focused into a band perpendicular to the
 1702 magnetospheric background field. Again using a detector radius of $2R_C$, equation (21)
 1703 suggests that inclusion of such an H₂ component would increase the latitudinal width
 1704 of the band on the detector. Besides, the H₂ envelope may increase the path length spent
 1705 by the energetic protons within Callisto’s atmosphere. Building upon our conclusions
 1706 for Europa (see section 3.2), this may rotate the maxima/minima of the detectable ENA
 1707 emissions closer toward the ram/wake apices, respectively. However, overall we do *not*
 1708 expect this component to introduce distinct, novel morphological features into our ENA

1709 emission maps. Since –in contrast to the H₂O bulge at Europa– the substantial presence
 1710 of H₂ at Callisto has not yet been verified through observations, it is not included in the
 1711 current iteration of our model.

1712 4 Summary and Concluding Remarks

1713 In this work, we have studied the intensity and morphology of energetic neutral atom
 1714 (ENA) emissions at Callisto and Europa. Charge exchange between energetic magne-
 1715 toospheric ions and cold atmospheric neutrals results in the production of such ENAs. Our
 1716 modeling framework is based upon a combination of a tracing tool for energetic mag-
 1717 netospheric ions and the AIKEF hybrid model (Müller et al., 2011) which calculates the
 1718 three-dimensional structure of the draped electromagnetic fields near both moons. We
 1719 trace billions of energetic parent ions through draped fields near the two moons. We cal-
 1720 culate maps of the ENA flux they emit through a spherical detector centered at each moon
 1721 and encompassing its entire atmosphere. Such a detector allows us to ascertain a com-
 1722 plete physical picture of detectable ENA emissions from Europa and Callisto which could
 1723 not be simultaneously captured by a point-like spacecraft detector with a limited field
 1724 of view.

1725 At both moons, we have constrained the variability of detectable ENA emissions
 1726 across a Jovian synodic rotation by comparing maps of the ENA flux when each moon
 1727 is either at the center or far outside the Jovian plasma sheet. The magnetospheric field
 1728 line draping at Callisto and Europa gradually weakens with distance to the center of the
 1729 plasma sheet. For each configuration, we have analyzed the influence of field line drap-
 1730 ing on parent ion dynamics and the resultant ENA emissions by comparing to a “base-
 1731 line” scenario with uniform electromagnetic fields. In order to constrain the detectable
 1732 ENA flux morphology as a function of parent ion energy, we have calculated maps of the
 1733 ENA flux through the detector sphere at five initial proton energies ranging from 1–100 keV.
 1734 As such, we predict the global distribution of ENA flux from Callisto’s and Europa’s at-
 1735 mospheres as will be observable during the upcoming JUICE mission (Grasset et al., 2013).

1736 We report our major results as follows:

- 1737 1. For a spacecraft located outside of Europa’s or Callisto’s atmosphere, detectable
 1738 ENA emissions are concentrated into a band of high flux, centered about the great
 1739 circle on the detector sphere normal to the ambient Jovian magnetospheric field.

- 1740 The latitudinal width of this band is determined by the extension of the obsta-
 1741 cle to the flow along the magnetospheric field lines, approximately given by the
 1742 sum of the moon's diameter and twice the atmospheric scale height. During the
 1743 course of a synodic rotation, the orientation of this band on the detector sphere
 1744 oscillates in phase with the time-varying background magnetic field vector.
- 1745 2. At the center of the Jovian plasma sheet where field line draping around Europa
 1746 and Callisto is strongest, the band of high ENA flux is attenuated in intensity re-
 1747 gardless of longitude on the spherical detector. In this case, the bulk of the ob-
 1748 servable ENA emissions is focused into a cluster of elevated ENA flux near the de-
 1749 tector's ramside apex (Europa) or Jupiter-facing apex (Callisto). When either moon
 1750 is located at its maximum distance below the center of the Jovian plasma sheet,
 1751 field line draping again attenuates the intensity of the observable ENA emissions,
 1752 but the emission patterns recorded on the detector are qualitatively similar for uni-
 1753 form and draped fields.
- 1754 3. The fraction of the total observable ENA flux that is confined to the high flux band
 1755 is determined by the ratio of energetic proton gyroradii and the moon's atmospheric
 1756 scale height. At Europa, regardless of its distance to the Jovian plasma sheet, par-
 1757 ent ions drifting with pitch angles near 90° can trace a path through the atmo-
 1758 sphere 10–100 times longer than that of ions traveling along the magnetic field.
 1759 This results in $\geq 80\%$ of the ENA flux emitted from Europa's atmosphere toward
 1760 the detector being concentrated within the high flux band. When Callisto is at
 1761 the center of the Jovian plasma sheet, energetic proton gyroradii are a factor of
 1762 5 – 50 larger than the atmospheric scale height. In consequence, protons with pitch
 1763 angles near 90° can only complete partial gyrations within the atmosphere. There-
 1764 fore, the band contains only 50 – 60% of the total ENA flux leaving Callisto's at-
 1765 mosphere. A significant population of ENAs hit the detector above or below the
 1766 band. Far outside the Jovian plasma sheet, the ratio of parent ion gyroradii and
 1767 Callisto's atmospheric scale height is similarly small as at Europa. Therefore, the
 1768 observable ENA emissions are again largely focused into a band perpendicular to
 1769 the background field.
- 1770 4. At both moons, a local maximum and a local minimum in ENA intensity form within
 1771 the band of high flux, separated on the spherical detector by approximately 180°
 1772 in longitude along the great circle that defines the band's equator. At Europa, the

maximum ENA flux is detected slightly west of the ramside apex. When gyrating ions drift into the moon's atmosphere from upstream, they emit ENAs toward Jupiter (i.e., west of the ramside apex) if they gyrate deep into the dense, lower atmosphere. They emit ENAs away from Jupiter (i.e., east of the ramside apex) if their gyration carries them back toward upstream, and they undergo charge exchange with the more rarefied neutral gas at higher altitudes. Since the likelihood of charge exchange is proportional to the local neutral density, a larger ENA flux is detectable west of the ramside apex than east of it. When Callisto is at the center of the plasma sheet, the maximum in ENA flux through the detector is further shifted, now located close to the Jupiter-facing apex. In this scenario, the magnetospheric field strength at Callisto is 1-2 orders of magnitude weaker than at Europa. Therefore, ion gyroradii at Callisto are large compared to the moon's atmospheric scale height. Due to their sense of gyration, parent ions mostly emit ENAs along trajectory segments bearing *toward* Jupiter, thereby causing the longitudinal shift in the location of the emission maximum. If the heavier magnetospheric ion species (oxygen, sulfur) were included in our Europa ENA model, their larger gyroradii would make the emission maps appear more similar to those calculated for protons at Callisto. However, the occurrence of the band-like structure would be largely unaffected.

5. The anisotropic PAD observed for protons at Europa by Juno (Sarkango et al., 2023) carries elevated particle fluxes at pitch angles near 0° and 180° . Including such an anisotropic PAD in our model leaves the morphology of the detectable ENA flux largely unchanged, compared to a setup using the approximately isotropic PAD observed by Galileo (Mauk et al., 2004). Including the anisotropic PAD increases the observable ENA flux by up to 25% in the mid-latitude regions of the detector's ramside hemisphere. The detectable ENA flux within the high flux band is diminished from the anisotropic PAD because it contains fewer parent ions with pitch angles near 90° than the isotropic one.
6. A localized H_2O exosphere around Europa's ramside apex (Roth, 2021), in addition to the moon's global O_2 atmosphere, produces only minor quantitative enhancements to the observable ENA flux. This suggests that even more localized and compact populations of water vapor (e.g., a plume) are likely difficult to detect against the "background" of ENA flux from Europa's global atmosphere, un-

1806 less they are located in regions where the magnetic field is perpendicular to the
1807 moons surface (i.e., outside of the band) and their scale height greatly exceeds that
1808 of the persistent atmosphere.

1809 The natural next step building upon this study is to incorporate a realistic, point-
1810 like spacecraft ENA detector with a limited field of view into our ENA generation model.
1811 In this way, we can perform predictive modeling of observable ENA emissions during sched-
1812 uled JUICE flybys of Callisto and Europa. Our work also forms the basis for assessing
1813 the relative contributions of ENAs emitted from the moons' atmospheres and surfaces
1814 (Pontoni et al., 2022) in a future study.

1815 Open Research Section

1816 Data supporting the production and conclusions of this work can be obtained from
1817 Haynes et al. (2023).

1818 Acknowledgments

1819 The authors acknowledge financial support through NASA's *Solar System Workings Pro-*
1820 *gram* 2019, grant # 80NSSC21K0152 as well as *Solar System Workings Program* 2020,
1821 grants # 80NSSC22K0097 and # 80NSSC23K0351. The authors perceive no financial
1822 conflicts of interest. The authors would like to thank Bob DeMajistre (Johns Hopkins
1823 University) for careful inspection of the manuscript and for valuable comments.

1824 **References**

- 1825 Addison, P., Liuzzo, L., Arnold, H., & Simon, S. (2021). Influence of Eu-
 1826 ropa's Time-Varying Electromagnetic Environment on Magnetospheric
 1827 Ion Precipitation and Surface Weathering. *Journal of Geophysical Re-*
 1828 *search: Space Physics*, 126(5), e2020JA029087. Retrieved from <https://agupubs.onlinelibrary.wiley.com/doi/abs/10.1029/2020JA029087>
 1830 (e2020JA029087 2020JA029087) doi: <https://doi.org/10.1029/2020JA029087>
- 1831 Addison, P., Liuzzo, L., & Simon, S. (2022). Effect of the Magnetospheric Plasma
 1832 Interaction and Solar Illumination on Ion Sputtering of Europa's Surface Ice.
 1833 *Journal of Geophysical Research: Space Physics*, 127(2), e2021JA030136.
 1834 Retrieved from <https://agupubs.onlinelibrary.wiley.com/doi/abs/10.1029/2021JA030136> (e2021JA030136 2021JA030136) doi: <https://doi.org/10.1029/2021JA030136>
- 1835 Arnold, H., Liuzzo, L., & Simon, S. (2019). Magnetic Signatures of a Plume at Eu-
 1836 ropa during the Galileo E26 Flyby. *Geophysical Research Letters*, 46(3), 1149–
 1837 1157. doi: 10.1029/2018GL081544
- 1838 Arnold, H., Liuzzo, L., & Simon, S. (2020). Plasma Interaction Signatures
 1839 of Plumes at Europa. *Journal of Geophysical Research: Space Physics*,
 1840 125(1), e2019JA027346. Retrieved from <https://agupubs.onlinelibrary.wiley.com/doi/abs/10.1029/2019JA027346> (e2019JA027346
 1841 10.1029/2019JA027346) doi: 10.1029/2019JA027346
- 1842 Arnold, H., Simon, S., & Liuzzo, L. (2020). Applying Ion Energy Spec-
 1843 trograms to Search for Plumes at Europa. *Journal of Geophysical Re-*
 1844 *search: Space Physics*, 125(9), e2020JA028376. Retrieved from <https://agupubs.onlinelibrary.wiley.com/doi/abs/10.1029/2020JA028376>
 1845 (e2020JA028376 10.1029/2020JA028376) doi: <https://doi.org/10.1029/2020JA028376>
- 1846 Bagdonat, T., & Motschmann, U. (2002). From a weak to a strong comet – 3D
 1847 global hybrid simulation studies. *Earth, Moon and Planets*, 90, 305–321.
- 1848 Bagenal, F., & Delamere, P. A. (2011). Flow of mass and energy in the magne-
 1849 tospheres of Jupiter and Saturn. *Journal of Geophysical Research (Space*
 1850 *Physics)*, 116, A05209. doi: 10.1029/2010JA016294
- 1851 Bagenal, F., Sidrow, E., Wilson, R. J., Cassidy, T. A., Dols, V., Crary, F. J., ... Pa-

- 1857 terson, W. R. (2015, November). Plasma conditions at Europa's orbit. *Icarus*,
 1858 261, 1-13. doi: 10.1016/j.icarus.2015.07.036
- 1859 Bagenal, F., Wilson, R. J., Siler, S., Paterson, W. R., & Kurth, W. S. (2016). Sur-
 1860 vey of Galileo plasma observations in Jupiter's plasma sheet. *Journal of Geo-*
 1861 *physical Research: Planets*, 121(5), 871-894. Retrieved from <https://agupubs.onlinelibrary.wiley.com/doi/abs/10.1002/2016JE005009> doi: <https://doi.org/10.1002/2016JE005009>
- 1862 Belkić, D. (2021). Single charge exchange in collisions of energetic nuclei with
 1863 biomolecules of interest to ion therapy. *Zeitschrift für Medizinische Physik*,
 1864 31(2), 122-144. Retrieved from <https://www.sciencedirect.com/science/article/pii/S0939388920300891> (Special Issue: Ion Beam Therapy, Part I)
 1865 doi: <https://doi.org/10.1016/j.zemedi.2020.07.003>
- 1866 Brandt, P., Dialynas, K., Dandouras, I., Mitchell, D., Garnier, P., & Krimigis, S.
 1867 (2012). The distribution of Titan's high-altitude (out to 50,000km) exo-
 1868 sphere from energetic neutral atom (ENA) measurements by Cassini/INCA.
 1869 *Planetary and Space Science*, 60(1), 107-114. Retrieved from <https://www.sciencedirect.com/science/article/pii/S0032063311001541> (Titan
 1870 Through Time: A Workshop on Titan's Formation, Evolution and Fate) doi:
 1871 <https://doi.org/10.1016/j.pss.2011.04.014>
- 1872 Breer, B. R., Liuzzo, L., Arnold, H., Andersson, P. N., & Simon, S. (2019). En-
 1873 ergetic Ion Dynamics in the Perturbed Electromagnetic Fields near Europa.
 1874 *Journal of Geophysical Research (Space Physics)*, 124(9), 7592–7613. doi:
 1875 [10.1029/2019JA027147](https://doi.org/10.1029/2019JA027147)
- 1876 Carberry Mogan, S. R., Johnson, Robert E., Vorburger, Audrey, & Roth, Lorenz.
 1877 (2023). Electron impact ionization in the icy Galilean satellites' atmospheres.
 1878 *Eur. Phys. J. D*, 77(2), 26. Retrieved from <https://doi.org/10.1140/epjd/s10053-023-00606-8> doi: 10.1140/epjd/s10053-023-00606-8
- 1879 Carberry Mogan, S. R., Tucker, O. J., Johnson, R. E., Sreenivasan, K. R., &
 1880 Kumar, S. (2020). The influence of collisions and thermal escape in
 1881 Callisto's atmosphere. *Icarus*, 352, 113932. Retrieved from <https://www.sciencedirect.com/science/article/pii/S0019103520303080> doi:
 1882 <https://doi.org/10.1016/j.icarus.2020.113932>
- 1883 Carberry Mogan, S. R., Tucker, O. J., Johnson, R. E., Vorburger, A., Galli, A.,
 1884

- 1890 Marchand, B., ... Sreenivasan, K. R. (2021). A tenuous, collisional at-
 1891 mosphere on Callisto. *Icarus*, 368, 114597. Retrieved from <https://www.sciencedirect.com/science/article/pii/S0019103521002621> doi:
 1892 <https://doi.org/10.1016/j.icarus.2021.114597>
- 1893 Carberry Mogan, S. R., Tucker, O. J., Johnson, R. E., Roth, L., Alday, J., Vor-
 1894 burger, A., ... Oza, A. V. (2022). Callisto's atmosphere: First evidence for
 1895 h₂ and constraints on h₂O. *Journal of Geophysical Research: Planets*, 127(11),
 1896 e2022JE007294. Retrieved from <https://agupubs.onlinelibrary.wiley.com/doi/abs/10.1029/2022JE007294> (e2022JE007294 2022JE007294) doi:
 1897 <https://doi.org/10.1029/2022JE007294>
- 1898 Carlson, R. W. (1999). A tenuous carbon dioxide atmosphere on jupiter's
 1899 moon callisto. *Science*, 283(5403), 820-821. Retrieved from <https://www.science.org/doi/abs/10.1126/science.283.5403.820> doi:
 1900 <https://doi.org/10.1126/science.283.5403.820>
- 1901 Cervantes, S., & Saur, J. (2022). Constraining Europa's Subsolar Atmosphere With
 1902 a Joint Analysis of HST Spectral Images and Galileo Magnetic Field Data.
 1903 *Journal of Geophysical Research: Space Physics*, 127(9), e2022JA030472.
 1904 Retrieved from <https://agupubs.onlinelibrary.wiley.com/doi/abs/10.1029/2022JA030472> (e2022JA030472 2022JA030472) doi: <https://doi.org/10.1029/2022JA030472>
- 1905 Clark, G., Mauk, B. H., Kollmann, P., Paranicas, C., Bagenal, F., Allen, R. C., ...
 1906 Westlake, J. H. (2020). Heavy Ion Charge States in Jupiter's Polar Mag-
 1907 netosphere Inferred From Auroral Megavolt Electric Potentials. *Journal of*
 1908 *Geophysical Research: Space Physics*, 125(9), e2020JA028052. Retrieved
 1909 from <https://agupubs.onlinelibrary.wiley.com/doi/abs/10.1029/2020JA028052> (e2020JA028052 2020JA028052) doi: <https://doi.org/10.1029/2020JA028052>
- 1910 Clark, G., Mauk, B. H., Paranicas, C., Kollmann, P., & Smith, H. T. (2016, March).
 1911 Charge states of energetic oxygen and sulfur ions in Jupiter's magnetosphere.
 1912 *Journal of Geophysical Research (Space Physics)*, 121, 2264-2273. doi:
 1913 [10.1002/2015JA022257](https://doi.org/10.1002/2015JA022257)
- 1914 Connerney, J. E., Acuña, M. H., Ness, N. F., & Satoh, T. (1998). New models of
 1915 Jupiter's magnetic field constrained by the Io flux tube footprint. *Journal of*
 1916 *Geophysical Research (Space Physics)*, 103(A11), 22701-22716.
- 1917

- 1923 *Geophysical Research: Space Physics*, 103(A6), 11929–11939.
- 1924 Connerney, J. E. P., Timmins, S., Herceg, M., & Joergensen, J. L. (2020). A
 1925 Jovian Magnetodisc Model for the Juno Era. *Journal of Geophysical Re-*
 1926 *search: Space Physics*, 125(10), e2020JA028138. Retrieved from <https://agupubs.onlinelibrary.wiley.com/doi/abs/10.1029/2020JA028138>
 1927 (e2020JA028138 2020JA028138) doi: <https://doi.org/10.1029/2020JA028138>
- 1928 Connerney, J. E. P., Timmins, S., Oliverson, R. J., Espley, J. R., Joergensen, J. L.,
 1929 Kotsiaros, S., ... Levin, S. M. (2022). A New Model of Jupiter's Magnetic
 1930 Field at the Completion of Juno's Prime Mission. *Journal of Geophys-*
 1931 *ical Research: Planets*, 127(2), e2021JE007055. Retrieved from <https://agupubs.onlinelibrary.wiley.com/doi/abs/10.1029/2021JE007055>
 1932 (e2021JE007055 2021JE007055) doi: <https://doi.org/10.1029/2021JE007055>
- 1933 Cooper, J. F., Johnson, R. E., Mauk, B. H., Garrett, H. B., & Gehrels, N. (2001).
 1934 Energetic ion and electron irradiation of the icy Galilean satellites. *Icarus*,
 1935 149(1), 133–159. doi: 10.1006/icar.2000.6498
- 1936 Cunningham, N. J., Spencer, J. R., Feldman, P. D., Strobel, D. F., France, K., &
 1937 Osterman, S. N. (2015). Detection of Callisto's oxygen atmosphere with the
 1938 Hubble Space Telescope. *Icarus*, 254, 178–189. Retrieved from <https://www.sciencedirect.com/science/article/pii/S0019103515001219> doi:
 1939 <https://doi.org/10.1016/j.icarus.2015.03.021>
- 1940 Dandouras, J., & Amsif, A. (1999). Production and imaging of energetic neutral
 1941 atoms from Titan's exosphere: a 3-D model. *Planetary and Space Science*,
 1942 47(10), 1355–1369. Retrieved from <https://www.sciencedirect.com/science/article/pii/S0032063399000574> doi: [https://doi.org/10.1016/S0032-0633\(99\)00057-4](https://doi.org/10.1016/S0032-0633(99)00057-4)
- 1943 de Kleer, K., Milby, Z., Schmidt, C., Camarca, M., & Brown, M. E. (2023, Feb.).
 1944 The Optical Aurorae of Europa, Ganymede, and Callisto. *The Planetary Sci-*
 1945 *ence Journal*, 4(2), 37. Retrieved from <https://dx.doi.org/10.3847/PSJ/acb53c> doi: 10.3847/PSJ/acb53c
- 1946 Delamere, P. A. (2009). Hybrid code simulations of the solar wind interaction with
 1947 Pluto. *Journal of Geophysical Research: Space Physics*, 114(A3). Retrieved
 1948 from <https://agupubs.onlinelibrary.wiley.com/doi/abs/10.1029/2008JA013756> doi: <https://doi.org/10.1029/2008JA013756>

- 1956 Dennerl, K. (2010, Dec). Charge transfer reactions. *Space Science Reviews*, 157(1-
1957 4), 57–91. doi: 10.1007/s11214-010-9720-5
- 1958 Desai, R. T., Cowee, M. M., Wei, H., Fu, X., Gary, S. P., Volwerk, M., & Coates,
1959 A. J. (2017). Hybrid Simulations of Positively and Negatively Charged Pickup
1960 Ions and Cyclotron Wave Generation at Europa. *Journal of Geophysical Re-*
1961 *search: Space Physics*, 122(10), 10,408-10,420. Retrieved from <https://agupubs.onlinelibrary.wiley.com/doi/abs/10.1002/2017JA024479> doi:
1962 <https://doi.org/10.1002/2017JA024479>
- 1963 Feyerabend, M., Liuzzo, L., Simon, S., & Motschmann, U. (2017). A Three-
1964 Dimensional Model of Pluto’s Interaction With the Solar Wind During the
1965 New Horizons Encounter. *Journal of Geophysical Research: Space Physics*,
1966 122(10), 356–10. doi: 10.1002/2017JA024456
- 1967 Galli, A., Vorburger, A., Carberry Mogan, S. R., Roussos, E., Stenberg Wieser, G.,
1968 Wurz, P., ... Liuzzo, L. (2022). Callisto’s Atmosphere and Its Space Envi-
1969 ronment: Prospects for the Particle Environment Package on Board JUICE.
1970 *Earth and Space Science*, 9(5), e2021EA002172. Retrieved from <https://agupubs.onlinelibrary.wiley.com/doi/abs/10.1029/2021EA002172>
1971 (e2021EA002172 2021EA002172) doi: <https://doi.org/10.1029/2021EA002172>
- 1972 Garnier, P., Dandouras, I., Toublanc, D., Roelof, E. C., Brandt, P. C., Mitchell,
1973 D. G., ... Wahlund, J.-E. (2008). The lower exosphere of Titan: En-
1974 ergetic neutral atoms absorption and imaging. *Journal of Geophysical
1975 Research: Space Physics*, 113(A10). Retrieved from <https://agupubs.onlinelibrary.wiley.com/doi/abs/10.1029/2008JA013029> doi:
1976 <https://doi.org/10.1029/2008JA013029>
- 1977 Garnier, P., Dandouras, I., Toublanc, D., Roelof, E. C., Brandt, P. C., Mitchell,
1978 D. G., ... Wahlund, J.-E. (2010). Statistical analysis of the energetic ion
1979 and ENA data for the Titan environment. *Planet. Space Sci.*, 58(14–15),
1811–1822. doi: 10.1016/j.pss.2010.08.009
- 1980 Grasset, O., Dougherty, M., Coustenis, A., Bunce, E., Erd, C., Titov, D., ... Van
1981 Hoolst, T. (2013). JUpiter ICy moons Explorer (JUICE): An ESA mission
1982 to orbit Ganymede and to characterise the Jupiter system. *Planetary and
1983 Space Science*, 78, 1-21. Retrieved from <https://www.sciencedirect.com/science/article/pii/S0032063312003777> doi: <https://doi.org/10.1016/j.pss.2012.12.001>

- 1989 j.pss.2012.12.002
- 1990 Hall, D. T., Strobel, D. F., Feldman, P. D., McGrath, M. A., & Weaver, H. A.
 1991 (1995, February). Detection of an oxygen atmosphere on Jupiter's moon Europa. *Nature*, 373, 677–679. doi: 10.1038/373677a0
- 1992 Harris, C. D. K., Jia, X., Slavin, J. A., Toth, G., Huang, Z., & Rubin, M.
 1993 (2021). Multi-Fluid MHD Simulations of Europa's Plasma Interaction
 1994 Under Different Magnetospheric Conditions. *Journal of Geophysical Re-*
 1995 *search: Space Physics*, 126(5), e2020JA028888. Retrieved from <https://agupubs.onlinelibrary.wiley.com/doi/abs/10.1029/2020JA028888>
 1996 (e2020JA028888 2020JA028888) doi: <https://doi.org/10.1029/2020JA028888>
- 1997 Hartkorn, O., & Saur, J. (2017). Induction signals from Callisto's ionosphere and
 1998 their implications on a possible subsurface ocean. *Journal of Geophysical*
 1999 *Research: Space Physics*, 122(11), 11,677-11,697. Retrieved from <https://agupubs.onlinelibrary.wiley.com/doi/abs/10.1002/2017JA024269> doi:
 2000 <https://doi.org/10.1002/2017JA024269>
- 2001 Hartkorn, O., Saur, J., & Strobel, D. F. (2017). Structure and density of Cal-
 2002 listo's atmosphere from a fluid-kinetic model of its ionosphere: Comparison
 2003 with Hubble Space Telescope and Galileo observations. *Icarus*, 282, 237-259.
 2004 Retrieved from <https://www.sciencedirect.com/science/article/pii/S0019103516305929> doi: <https://doi.org/10.1016/j.icarus.2016.09.020>
- 2005 Haynes, C. M., Tippens, T., Addison, P., Liuzzo, L., Poppe, A. R., & Simon,
 2006 S. (2023). Data for “Emission of Energetic Neutral Atoms from the
 2007 Magnetosphere-Atmosphere Interactions at Callisto and Europa” by Haynes
 2008 et al., 2023 [Data set]. *Zenodo*, <https://doi.org/10.5281/zenodo.8148610>. doi:
 2009 [10.5281/zenodo.8148610](https://doi.org/10.5281/zenodo.8148610)
- 2010 Jia, X., Kivelson, M. G., Khurana, K. K., & Kurth, W. S. (2018). Evidence of a
 2011 plume on Europa from Galileo magnetic and plasma wave signatures. *Nature*
 2012 *Astronomy*, 2, 459–464. doi: 10.1038/s41550-018-0450-z
- 2013 Johnson, L. K., Gao, R. S., Smith, K. A., & Stebbings, R. F. (1988, Sep.). Ab-
 2014 solute differential cross sections for very-small-angle scattering of keV H
 2015 and He atoms by H₂ and N₂. *Phys. Rev. A*, 38, 2794–2797. Retrieved
 2016 from <https://link.aps.org/doi/10.1103/PhysRevA.38.2794> doi:
 2017 [10.1103/PhysRevA.38.2794](https://doi.org/10.1103/PhysRevA.38.2794)

- 2022 Kabanovic, S., Feyerabend, M., Simon, S., Meeks, Z., & Wulms, V. (2018, March).
 2023 Influence of asymmetries in the magnetic draping pattern at Titan on the
 2024 emission of energetic neutral atoms. *Planet. Space Sci.*, 152, 142-164. doi:
 2025 10.1016/j.pss.2017.12.017
- 2026 Khurana, K. K. (1997). Euler potential models of Jupiter's magnetospheric field.
 2027 *Journal of Geophysical Research (Space Physics)*, 102, 11295–11306. doi: 10
 2028 .1029/97JA00563
- 2029 Khurana, K. K., Kivelson, M. G., Stevenson, D. J., Schubert, G., Russell, C. T.,
 2030 Walker, R. J., & Polanskey, C. (1998). Induced magnetic fields as evidence for
 2031 subsurface oceans in Europa and Callisto. *Nature*, 395(6704), 777–780. doi:
 2032 10.1038/27394
- 2033 Kim, T. K., Ebert, R. W., Valek, P. W., Allegrini, F., McComas, D. J., Bage-
 2034 nal, F., ... Bolton, S. J. (2020). Survey of Ion Properties in Jupiter's
 2035 Plasma Sheet: Juno JADE-I Observations. *Journal of Geophysical Re-*
 2036 *search: Space Physics*, 125(4), e2019JA027696. Retrieved from <https://agupubs.onlinelibrary.wiley.com/doi/abs/10.1029/2019JA027696>
 2037 (e2019JA027696 10.1029/2019JA027696) doi: <https://doi.org/10.1029/2019JA027696>
- 2040 Kivelson, M. G., Bagenal, F., Kurth, W. S., Neubauer, F. M., Paranicas, C., &
 2041 Saur, J. (2004). Magnetospheric interactions with satellites. In F. Bagenal,
 2042 T.E. Dowling and W.B. McKinnon (Ed.), *Jupiter. The planet, satellites and*
 2043 *magnetosphere* (pp. 513–536). Cambridge Univ. Press.
- 2044 Kivelson, M. G., Khurana, K. K., Russell, C. T., Volwerk, M., Walker, R. J., & Zim-
 2045 mer, C. (2000). Galileo Magnetometer Measurements: A Stronger Case for
 2046 a Subsurface Ocean at Europa. *Science*, 289(5483), 1340–1343. Retrieved
 2047 from <https://science.sciencemag.org/content/289/5483/1340> doi:
 2048 10.1126/science.289.5483.1340
- 2049 Kivelson, M. G., Khurana, K. K., Stevenson, D. J., Bennett, L., Joy, S., Russell,
 2050 C. T., ... Polanskey, C. (1999). Europa and Callisto: Induced or intrinsic
 2051 fields in a periodically varying plasma environment. *Journal of Geophysical*
 2052 *Research (Space Physics)*, 104(A3), 4609–4626. doi: 10.1029/1998JA900095
- 2053 Kollmann, P., Paranicas, C., Clark, G., Mauk, B. H., Haggerty, D. K., Rymer,
 2054 A. M., ... Bolton, S. (2017). A heavy ion and proton radiation belt in-

- 2055 side of Jupiter's rings. *Geophysical Research Letters*, 44(11), 5259-5268.
2056 Retrieved from <https://agupubs.onlinelibrary.wiley.com/doi/abs/10.1002/2017GL073730> doi: <https://doi.org/10.1002/2017GL073730>
- 2057 Kollmann, P., Paranicas, C., Clark, G., Roussos, E., Lagg, A., & Krupp, N. (2016).
2059 The vertical thickness of Jupiter's Europa gas torus from charged particle
2060 measurements. *Geophysical Research Letters*, 43(18), 9425-9433. Retrieved
2061 from <https://agupubs.onlinelibrary.wiley.com/doi/abs/10.1002/2016GL070326> doi: <https://doi.org/10.1002/2016GL070326>
- 2063 Kollmann, P., Roussos, E., Paranicas, C., Woodfield, E. E., Mauk, B. H., Clark, G.,
2064 ... Vandegriff, J. (2018). Electron Acceleration to MeV Energies at Jupiter
2065 and Saturn. *Journal of Geophysical Research: Space Physics*, 123(11), 9110-
2066 9129. Retrieved from <https://agupubs.onlinelibrary.wiley.com/doi/abs/10.1029/2018JA025665> doi: <https://doi.org/10.1029/2018JA025665>
- 2068 Krimigis, S. M., Mitchell, D. G., Hamilton, D. C., Livi, S., Dandouras, J., Jaskulek,
2069 ... Williams, D. J. (2004, September). Magnetosphere Imaging Instrument
2070 (MIMI) on the Cassini Mission to Saturn/Titan. *Space Science Reviews*, 114,
2071 233-329, doi: 10.1007/s11214-004-1410-8.
- 2072 Kurth, W. S., Gurnett, D. A., Persoon, A. M., Roux, A., Bolton, S. J., & Alexander,
2073 C. J. (2001, March). The plasma wave environment of Europa. *Planet. Space
Sci.*, 49, 345-363. doi: 10.1016/S0032-0633(00)00156-2
- 2075 Lagg, A., Krupp, N., Woch, J., & Williams, D. J. (2003). In-situ observations
2076 of a neutral gas torus at Europa. *Geophysical Research Letters*, 30(11).
2077 Retrieved from <https://agupubs.onlinelibrary.wiley.com/doi/abs/10.1029/2003GL017214> doi: <https://doi.org/10.1029/2003GL017214>
- 2079 Lindkvist, J., Holmström, M., Khurana, K. K., Fatemi, S., & Barabash, S. (2015).
2080 Callisto plasma interactions: Hybrid modeling including induction by a sub-
2081 surface ocean. *Journal of Geophysical Research: Space Physics*, 120(6), 4877-
2082 4889. Retrieved from <https://agupubs.onlinelibrary.wiley.com/doi/abs/10.1002/2015JA021212> doi: <https://doi.org/10.1002/2015JA021212>
- 2084 Lindsay, B. G., & Stebbings, R. F. (2005, December). Charge transfer cross sec-
2085 tions for energetic neutral atom data analysis. *Journal of Geophysical Research
(Space Physics)*, 110, A12213. doi: 10.1029/2005JA011298
- 2087 Liuzzo, L., Feyerabend, M., Simon, S., & Motschmann, U. (2015, November). The

- 2088 impact of Callisto's atmosphere on its plasma interaction with the Jovian mag-
 2089 netosphere. *Journal of Geophysical Research (Space Physics)*, 120, 9401-9427.
 2090 doi: 10.1002/2015JA021792
- 2091 Liuzzo, L., Poppe, A. R., Addison, P., Simon, S., Nénon, Q., & Paranicas, C. (2022).
 2092 Energetic Magnetospheric Particle Fluxes onto Callisto's Atmosphere. *Journal*
 2093 *of Geophysical Research: Space Physics*, n/a(n/a), e2022JA030915. Retrieved
 2094 from <https://agupubs.onlinelibrary.wiley.com/doi/abs/10.1029/2022JA030915> (e2022JA030915 2022JA030915) doi: <https://doi.org/10.1029/2022JA030915>
- 2097 Liuzzo, L., Simon, S., & Feyerabend, M. (2018). Observability of Callisto's In-
 2098 ductive Signature During the JUpiter ICY Moons Explorer Mission. *Journal*
 2099 *of Geophysical Research: Space Physics*, 123(11), 9045-9054. Retrieved
 2100 from <https://agupubs.onlinelibrary.wiley.com/doi/abs/10.1029/2018JA025951> doi: <https://doi.org/10.1029/2018JA025951>
- 2102 Liuzzo, L., Simon, S., Feyerabend, M., & Motschmann, U. (2016). Disentan-
 2103 gling plasma interaction and induction signatures at Callisto: The Galileo
 2104 C10 flyby. *Journal of Geophysical Research: Space Physics*, 121(9), 8677–
 2105 8694. Retrieved from <http://dx.doi.org/10.1002/2016JA023236> doi:
 2106 <https://doi.org/10.1002/2016JA023236>
- 2107 Liuzzo, L., Simon, S., Feyerabend, M., & Motschmann, U. (2017). Magnetic signa-
 2108 tures of plasma interaction and induction at Callisto: The Galileo C21, C22,
 2109 C23, and C30 flybys. *Journal of Geophysical Research: Space Physics*, 122(7),
 2110 7364–7386. doi: [10.1002/2017JA024303](https://doi.org/10.1002/2017JA024303)
- 2111 Liuzzo, L., Simon, S., & Regoli, L. (2019a). Energetic electron dynamics near
 2112 Callisto. *Planetary and Space Science*, 179, 104726. Retrieved from
 2113 <http://www.sciencedirect.com/science/article/pii/S0032063319302430>
 2114 doi: <https://doi.org/10.1016/j.pss.2019.104726>
- 2115 Liuzzo, L., Simon, S., & Regoli, L. (2019b). Energetic ion dynamics near Cal-
 2116 listo. *Planetary and Space Science*, 166, 23-53. Retrieved from <https://www.sciencedirect.com/science/article/pii/S0032063318301648> doi:
 2117 <https://doi.org/10.1016/j.pss.2018.07.014>
- 2119 Loand, H., & Tite, W. (1969). Electron-capture and loss cross sections for fast,
 2120 heavy particles passing through gases. *Atomic Data and Nuclear Data*

- 2121 Tables, 1, 305-328. Retrieved from <https://www.sciencedirect.com/science/article/pii/S0092640X69800252> doi: [https://doi.org/10.1016/S0092-640X\(69\)80025-2](https://doi.org/10.1016/S0092-640X(69)80025-2)
- 2124 Mauk, B. H., Clark, G., Allegrini, F., Bagenal, F., Bolton, S. J., Connerney, J. E. P.,
 2125 ... Rymer, A. M. (2020). Juno Energetic Neutral Atom (ENA) Remote Measurements
 2126 of Magnetospheric Injection Dynamics in Jupiter's Io Torus Regions.
 2127 *Journal of Geophysical Research: Space Physics*, 125(5), e2020JA027964.
 2128 Retrieved from <https://agupubs.onlinelibrary.wiley.com/doi/abs/10.1029/2020JA027964> (e2020JA027964 2020JA027964) doi: <https://doi.org/10.1029/2020JA027964>
- 2131 Mauk, B. H., Mitchell, D., Krimigis, S., Roelof, E., & Paranicas, C. (2003, February).
 2132 Energetic neutral atoms from a trans-Europa gas torus at Jupiter.
 2133 *Nature*, 421(6926), 920—922. Retrieved from <https://doi.org/10.1038/nature01431> doi: 10.1038/nature01431
- 2135 Mauk, B. H., Mitchell, D., McEntire, R., Paranicas, C., Roelof, E., Williams, D., ...
 2136 Lagg, A. (2004). Energetic ion characteristics and neutral gas interactions
 2137 in Jupiter's magnetosphere. *Journal of Geophysical Research: Space Physics*,
 2138 109(A9). doi: 10.1029/2003JA010270
- 2139 Mitchell, D. G., Brandt, P. C., Roelof, E. C., Dandouras, J., Krimigis, S. M., &
 2140 Mauk, B. H. (2005). Energetic Neutral Atom Emissions from Titan Interaction
 2141 with Saturn's Magnetosphere. *Science*, 308(5724), 989-992. Retrieved
 2142 from <https://www.science.org/doi/abs/10.1126/science.1109805> doi:
 2143 10.1126/science.1109805
- 2144 Mitchell, D. G., Cheng, A. F., Krimigis, S. M., Keath, E. P., Jaskulek, S. E., Mauk,
 2145 B. H., ... Drake, V. A. (1993). INCA: the ion neutral camera for energetic
 2146 neutral atom imaging of the Saturnian magnetosphere. *Optical Engineering*,
 2147 32(12), 3096 – 3101. Retrieved from <https://doi.org/10.1117/12.155609>
 2148 doi: 10.1117/12.155609
- 2149 Mitchell, D. G., Krimigis, S. M., Cheng, A. F., Hsieh, S.-L., Jaskulek, S. E., Keath,
 2150 E. P., ... Williams, D. J. (1996). Imaging-neutral camera (INCA) for the
 2151 NASA Cassini mission to Saturn and Titan. *Proceedings of SPIE*, 2803,
 2152 154 – 161. Retrieved from <https://doi.org/10.1117/12.253415> doi:
 2153 10.1117/12.253415

- 2154 Müller, J., Simon, S., Motschmann, U., Schüle, J., Glassmeier, K.-H., & Pringle,
 2155 G. J. (2011). A.i.k.e.f.: Adaptive hybrid model for space plasma sim-
 2156 ulations. *Computer Physics Communications*, 182(4), 946-966. Retrieved
 2157 from <https://www.sciencedirect.com/science/article/pii/S0010465510005266> doi: <https://doi.org/10.1016/j.cpc.2010.12.033>
- 2159 Neubauer, F. M. (1980). Nonlinear standing Alfvén wave current system at Io - The-
 2160 ory. *J. Geophys. Res.*, 85, 1171–1178. doi: 10.1029/JA085iA03p01171
- 2161 Neubauer, F. M. (1998). The sub-Alfvénic interaction of the Galilean satellites with
 2162 the Jovian magnetosphere. *J. Geophys. Res.*, 103, 19843–19866. doi: 10.1029/
 2163 97JE03370
- 2164 Neubauer, F. M. (1999). Alfvén wings and electromagnetic induction in the inte-
 2165 riors: Europa and Callisto. *Journal of Geophysical Research (Space Physics)*,
 2166 104(A12), 28671–28684. doi: 10.1029/1999JA900217
- 2167 Neubauer, F. M., Backes, H., Dougherty, M. K., Wennmacher, A., Russell, C. T.,
 2168 Coates, A., ... Saur, J. (2006). Titan's near magnetotail from magnetic field
 2169 and plasma observations and modelling: Cassini flybys TA, TB and T3. *J.
 2170 Geophys. Res.*, 111, A10220. doi: 10.1029/2006JA011676
- 2171 Nordheim, T. A., Regoli, L. H., Harris, C. D. K., Paranicas, C., Hand, K. P., & Jia,
 2172 X. (2022, jan). Magnetospheric Ion Bombardment of Europa's Surface. *The
 2173 Planetary Science Journal*, 3(1), 5. Retrieved from <https://dx.doi.org/10.3847/PSJ/ac382a> doi: 10.3847/PSJ/ac382a
- 2175 Nénon, Q., & André, N. (2019). Evidence of Europa Neutral Gas Torii From En-
 2176 ergetic Sulfur Ion Measurements. *Geophysical Research Letters*, 46(7), 3599-
 2177 3606. Retrieved from <https://agupubs.onlinelibrary.wiley.com/doi/abs/10.1029/2019GL082200> doi: <https://doi.org/10.1029/2019GL082200>
- 2179 Nénon, Q., Sicard, A., Kollmann, P., Garrett, H. B., Sauer, S. P. A., & Paranicas,
 2180 C. (2018). A Physical Model of the Proton Radiation Belts of Jupiter inside
 2181 Europa's Orbit. *Journal of Geophysical Research: Space Physics*, 123(5), 3512-
 2182 3532. Retrieved from <https://agupubs.onlinelibrary.wiley.com/doi/abs/10.1029/2018JA025216> doi: <https://doi.org/10.1029/2018JA025216>
- 2184 Paganini, L., Villanueva, G. L., Roth, L., Mandell, A. M., Hurford, T. A., Rether-
 2185 ford, K. D., & Mumma, M. J. (2019, November). A measurement of water
 2186 vapour amid a largely quiescent environment on Europa. *Nature Astronomy*,

- 2187 4, 266-272. doi: 10.1038/s41550-019-0933-6
- 2188 Paranicas, C., Cooper, J. F., Garrett, H. B., Johnson, R. E., & Sturner, S. J. (2009).
 2189 Europa's Radiation Environment and Its Effects on the Surface. In R. T. Pap-
 2190 palardo, W. B. McKinnon, & K. K. Khurana (Eds.), *Europa, edited by robert*
 2191 *t. pappalardo, william b. mckinnon, krishan k. khurana ; with the assistance of*
 2192 *rené dotson with 85 collaborating authors. university of arizona press, tucson,*
 2193 *2009. the university of arizona space science series isbn: 9780816528448, p.529*
 2194 (p. 529).
- 2195 Paranicas, C., Hibbitts, C., Kollmann, P., Ligier, N., Hendrix, A., Nordheim, T., ...
 2196 Clark, G. (2018). Magnetospheric considerations for solar system ice state.
 2197 *Icarus*, 302, 560-564. Retrieved from <https://www.sciencedirect.com/science/article/pii/S0019103517304128> doi: <https://doi.org/10.1016/j.icarus.2017.12.013>
- 2200 Paranicas, C., McEntire, R. W., Cheng, A. F., Lagg, A., & Williams, D. J. (2000,
 2201 July). Energetic charged particles near Europa. *J. Geophys. Res.*, 105, 16005-
 2202 16016. doi: 10.1029/1999JA000350
- 2203 Paranicas, C., Ratliff, J. M., Mauk, B. H., Cohen, C., & Johnson, R. E. (2002,
 2204 March). The ion environment near Europa and its role in surface energetics.
 2205 *GRL*, 29, 18-1. doi: 10.1029/2001GL014127
- 2206 Plainaki, C., Cassidy, T. A., Shematovich, V. I., Milillo, A., Wurz, P., Vor-
 2207 burger, A., ... Teolis, B. (2018, February). Towards a Global Unified
 2208 Model of Europa's Tenuous Atmosphere. *Space Sci. Rev.*, 214, 40. doi:
 2209 10.1007/s11214-018-0469-6
- 2210 Pontoni, A., Shimoyama, M., Futaana, Y., Fatemi, S., Poppe, A. R., Wieser, M., &
 2211 Barabash, S. (2022). Simulations of Energetic Neutral Atom Sputtering From
 2212 Ganymede in Preparation for the JUICE Mission. *Journal of Geophysical Re-*
 2213 *search: Space Physics*, 127(1), e2021JA029439. Retrieved from <https://agupubs.onlinelibrary.wiley.com/doi/abs/10.1029/2021JA029439>
 2214 (e2021JA029439 2021JA029439) doi: <https://doi.org/10.1029/2021JA029439>
- 2216 Regoli, L., Roussos, E., Feyerabend, M., Jones, G. H., Krupp, N., Coates, A. J., ...
 2217 Dougherty, M. (2016). Access of energetic particles to Titan's exobase: A
 2218 study of Cassini's t9 flyby. *Planetary and Space Science*, 130, 40-53. doi:
 2219 10.1016/j.pss.2015.11.013

- 2220 Regoli, L. H., Roussos, E., Dialynas, K., Luhmann, J. G., Sergis, N., Jia, X., ...
 2221 Rae, I. J. (2018). Statistical Study of the Energetic Proton Environment at Titan's Orbit From the Cassini Spacecraft. *Journal of Geophysical Research: Space Physics*, 123(6), 4820-4834. Retrieved from <https://agupubs.onlinelibrary.wiley.com/doi/abs/10.1029/2018JA025442> doi: <https://doi.org/10.1029/2018JA025442>
- 2226 Roth, L. (2021). A Stable H₂O Atmosphere on Europa's Trailing Hemisphere
 2227 From HST Images. *Geophysical Research Letters*, 48(20), e2021GL094289.
 2228 Retrieved from <https://agupubs.onlinelibrary.wiley.com/doi/abs/10.1029/2021GL094289> (e2021GL094289 2021GL094289) doi: <https://doi.org/10.1029/2021GL094289>
- 2231 Roth, L., Alday, J., Becker, T. M., Ivchenko, N., & Retherford, K. D. (2017).
 2232 Detection of a hydrogen corona at Callisto. *Journal of Geophysical Research: Planets*, 122(5), 1046-1055. Retrieved from <https://agupubs.onlinelibrary.wiley.com/doi/abs/10.1002/2017JE005294> doi: <https://doi.org/10.1002/2017JE005294>
- 2236 Roth, L., Retherford, K. D., Ivchenko, N., Schlatter, N., Strobel, D. F., Becker,
 2237 T. M., & Grava, C. (2017, jan). Detection of a Hydrogen Corona in HST Ly
 2238 Images of Europa in Transit of Jupiter. *The Astronomical Journal*, 153(2),
 2239 67. Retrieved from <https://dx.doi.org/10.3847/1538-3881/153/2/67> doi:
 2240 [10.3847/1538-3881/153/2/67](https://doi.org/10.3847/1538-3881/153/2/67)
- 2241 Roth, L., Retherford, K. D., Saur, J., Strobel, D. F., Feldman, P. D., McGrath,
 2242 M. A., & Nimmo, F. (2014, December). Orbital apocenter is not a suf-
 2243 ficient condition for HST/STIS detection of Europa's water vapor aurora.
 2244 *Proceedings of the National Academy of Science*, 111, E5123-E5132. doi:
 2245 [10.1073/pnas.1416671111](https://doi.org/10.1073/pnas.1416671111)
- 2246 Roth, L., Saur, J., Retherford, K. D., Strobel, D. F., Feldman, P. D., McGrath,
 2247 M. A., & Nimmo, F. (2014). Transient Water Vapor at Europa's South Pole.
 2248 *Science*, 343(6167), 171–174. doi: [10.1126/science.1247051](https://doi.org/10.1126/science.1247051)
- 2249 Roth, L., Saur, J., Retherford, K. D., Strobel, D. F., Feldman, P. D., McGrath,
 2250 M. A., ... Ivchenko, N. (2016). Europa's far ultraviolet oxygen aurora
 2251 from a comprehensive set of HST observations. *Journal of Geophysical Research (Space Physics)*, n/a. Retrieved from <http://dx.doi.org/10.1002/>

- 2253 2015JA022073 doi: 10.1002/2015JA022073
- 2254 Roth, L., Smith, H. T., Yoshioka, K., Becker, T. M., Blöcker, A., Cunningham,
 2255 N. J., ... Tsuchiya, F. (2023, may). Constraints on Europa's Water Group
 2256 Torus from HST/COS Observations. *The Planetary Science Journal*, 4(5),
 2257 87. Retrieved from <https://dx.doi.org/10.3847/PSJ/accded> doi:
 2258 10.3847/PSJ/accded
- 2259 Rubin, M., Jia, X., Altweig, K., Combi, M. R., Daldorff, L. K. S., Gombosi,
 2260 T. I., ... Wurz, P. (2015, May). Self-consistent multifluid MHD simu-
 2261 lations of Europa's exospheric interaction with Jupiter's magnetosphere.
 2262 *Journal of Geophysical Research (Space Physics)*, 120, 3503–3524. doi:
 2263 10.1002/2015JA021149
- 2264 Sarkango, Y., Szalay, J. R., Poppe, A. R., Nénon, Q., Kollmann, P., Clark, G.,
 2265 & McComas, D. J. (2023). Proton Equatorial Pitch Angle Distributions
 2266 in Jupiter's Inner Magnetosphere. *Geophysical Research Letters*, 50(11),
 2267 e2023GL104374. Retrieved from <https://agupubs.onlinelibrary.wiley.com/doi/abs/10.1029/2023GL104374> (e2023GL104374 2023GL104374) doi:
 2268 <https://doi.org/10.1029/2023GL104374>
- 2269 Saur, J., Feldman, P. D., Roth, L., Nimmo, F., Strobel, D. F., Rutherford, K. D.,
 2270 ... Grodent, D. (2011, aug.). Hubble Space Telescope Advanced Cam-
 2271 era for Survey Observations of Europa's Atmospheric Ultraviolet Emis-
 2272 sion at Eastern Elongation. *The Astrophysical Journal*, 738(2), 153. Re-
 2273 tried from <https://doi.org/10.1088/0004-637x/738/2/153> doi:
 2274 10.1088/0004-637x/738/2/153
- 2275 Saur, J., Neubauer, F. M., & Glassmeier, K.-H. (2010). Induced magnetic fields in
 2276 solar system bodies. *Space Science Reviews*, 152(1-4), 391–421.
- 2277 Saur, J., Strobel, D. F., & Neubauer, F. M. (1998, September). Interaction of the
 2278 Jovian magnetosphere with Europa: Constraints on the neutral atmosphere.
 2279 *Journal of Geophysical Research (Space Physics)*, 103, 19947–19962. doi:
 2280 10.1029/97JE03556
- 2281 Schilling, N., Neubauer, F. M., & Saur, J. (2007). Time-varying interaction of
 2282 Europa with the Jovian magnetosphere: Constraints on the conductivity of
 2283 Europa's subsurface ocean. *Icarus*, 192(1), 41–55. Retrieved from <https://www.sciencedirect.com/science/article/pii/S0019103507002837> doi:
 2284

- 2286 https://doi.org/10.1016/j.icarus.2007.06.024
- 2287 Seufert, M., Saur, J., & Neubauer, F. M. (2011). Multi-frequency electromagnetic
2288 sounding of the Galilean moons. *Icarus*, 214(2), 477–494. doi: 10.1016/j.icarus
2289 .2011.03.017
- 2290 Shen, X.-C., Li, W., Ma, Q., Nishimura, Y., Daly, A., Kollmann, P., ... Bolton, S.
2291 (2022). Energetic Proton Distributions in the Inner and Middle Magnetosphere
2292 of Jupiter Using Juno Observations. *Geophysical Research Letters*, 49(16),
2293 e2022GL099832. Retrieved from <https://agupubs.onlinelibrary.wiley.com/doi/abs/10.1029/2022GL099832> (e2022GL099832 2022GL099832) doi:
2294 <https://doi.org/10.1029/2022GL099832>
- 2295 Shprits, Y., Menietti, D., Drozdov, A., Horne, R., Woodfield, E., Groene, J.,
2296 ... Gurnett, D. (2018). Strong whistler mode waves observed in the
2297 vicinity of Jupiter's moons. *Nature Communications*, 9(1), 7–12. doi:
2298 [10.1038/s41467-018-0543](https://doi.org/10.1038/s41467-018-0543)
- 2299 Simon, S., Boesswetter, A., Bagdonat, T., Motschmann, U., & Schuele, J. (2007).
2300 Three-dimensional multispecies hybrid simulation of Titan's highly variable
2301 plasma environment. *Annales Geophysicae*, 25(1), 117–144. Retrieved
2302 from <https://angeo.copernicus.org/articles/25/117/2007/> doi:
2303 [10.5194/angeo-25-117-2007](https://doi.org/10.5194/angeo-25-117-2007)
- 2304 Simon, S., & Motschmann, U. (2009). Titan's induced magnetosphere under
2305 non-ideal upstream conditions: 3D multi-species hybrid simulations. *Plan-
2306 etary and Space Science*, 57(14), 2001-2015. Retrieved from <https://www.sciencedirect.com/science/article/pii/S0032063309002499> doi:
2307 <https://doi.org/10.1016/j.pss.2009.08.010>
- 2308 Simon, S., Roussos, E., & Paty, C. S. (2015). The interaction between Saturn's
2309 moons and their plasma environments. *Physics Reports*, 602, 1-65. Retrieved
2310 from <https://www.sciencedirect.com/science/article/pii/S037015731500441X> (The interaction between Saturn's moons and their
2311 plasma environments) doi: <https://doi.org/10.1016/j.physrep.2015.09.005>
- 2312 Simon, S., Saur, J., Kriegel, H., Neubauer, F., Motschmann, U., & Dougherty, M.
2313 (2011). Influence of negatively charged plume grains and hemisphere coupling
2314 currents on the structure of Enceladus' Alfvén wings: Analytical modelling of
2315 Cassini magnetometer observations. *Journal of Geophysical Research (Space*

- 2319 *Physics*), 116(A4), A04221. doi: 10.1029/2010JA016338
- 2320 Smith, H., Mitchell, D., Johnson, R., & Paranicas, C. (2009). Investigation
 2321 of energetic proton penetration in Titan's atmosphere using the Cassini
 2322 INCA instrument. *Planetary and Space Science*, 57(13), 1538-1546. Retrieved
 2323 from <https://www.sciencedirect.com/science/article/pii/S0032063309000993> (Surfaces and Atmospheres of the Outer Planets,
 2324 Their Satellites and Ring Systems: Part V) doi: <https://doi.org/10.1016/j.pss.2009.03.013>
- 2327 Smith, H., Mitchell, D. G., Johnson, R. E., Mauk, B. H., & Smith, J. E. (2019,
 2328 jan). Europa neutral torus confirmation and characterization based on ob-
 2329 servations and modeling. *The Astrophysical Journal*, 871(1), 69. Retrieved
 2330 from <https://doi.org/10.3847/1538-4357/aaed38> doi: 10.3847/1538-4357/
 2331 aaed38
- 2332 Styczinski, M. J., & Harnett, E. M. (2021, January). Induced magnetic moments
 2333 from a nearly spherical ocean. *Icarus*, 354, 114020. Retrieved from <https://europepmc.org/articles/PMC8819694> doi: 10.1016/j.icarus.2020.114020
- 2335 Szalay, J. R., Allegrini, F., Bagenal, F., Bolton, S., Clark, G., Connerney, J. E. P.,
 2336 ... Wilson, R. J. (2017). Plasma measurements in the Jovian polar re-
 2337 gion with Juno/JADE. *Geophysical Research Letters*, 44(14), 7122-7130.
 2338 Retrieved from <https://agupubs.onlinelibrary.wiley.com/doi/abs/10.1002/2017GL072837> doi: <https://doi.org/10.1002/2017GL072837>
- 2340 Tawara, H., Kato, T., & Nakai, Y. (1985). Cross sections for electron capture
 2341 and loss by positive ions in collisions with atomic and molecular hydrogen.
 2342 *Atomic Data and Nuclear Data Tables*, 32(2), 235-303. Retrieved from
 2343 <https://www.sciencedirect.com/science/article/pii/0092640X85900075>
 2344 doi: [https://doi.org/10.1016/0092-640X\(85\)90007-5](https://doi.org/10.1016/0092-640X(85)90007-5)
- 2345 Tippens, T., Liuzzo, L., & Simon, S. (2022). Influence of Titan's Variable Electro-
 2346 magnetic Environment on the Global Distribution of Energetic Neutral Atoms.
 2347 *Journal of Geophysical Research: Space Physics*, 127(10), e2022JA030722.
 2348 Retrieved from [\(e2022JA030722 2022JA030722\)](https://agupubs.onlinelibrary.wiley.com/doi/abs/10.1029/2022JA030722) doi: <https://doi.org/10.1029/2022JA030722>
- 2351 Toburen, L. H., Nakai, M. Y., & Langley, R. A. (1968, Jul). Measurement

- 2352 of High-Energy Charge-Transfer Cross Sections for Incident Protons and
 2353 Atomic Hydrogen in Various Gases. *Phys. Rev.*, *171*, 114–122. Retrieved
 2354 from <https://link.aps.org/doi/10.1103/PhysRev.171.114> doi:
 2355 [10.1103/PhysRev.171.114](https://doi.org/10.1103/PhysRev.171.114)
- 2356 Vance, S. D., Panning, M. P., Stähler, S., Cammarano, F., Bills, B. G., Tobie, G.,
 2357 ... Banerdt, B. (2018). Geophysical Investigations of Habitability in Ice-
 2358 Covered Ocean Worlds. *Journal of Geophysical Research: Planets*, *123*(1),
 2359 180–205. Retrieved from <https://agupubs.onlinelibrary.wiley.com/doi/abs/10.1002/2017JE005341> doi: <https://doi.org/10.1002/2017JE005341>
- 2360 Vance, S. D., Styczinski, M. J., Bills, B. G., Cochrane, C. J., Soderlund, K. M.,
 2361 Gómez-Pérez, N., & Paty, C. (2021). Magnetic Induction Responses of
 2362 Jupiter's Ocean Moons Including Effects From Adiabatic Convection. *Jour-*
 2363 *nal of Geophysical Research: Planets*, *126*(2), e2020JE006418. Retrieved
 2364 from <https://agupubs.onlinelibrary.wiley.com/doi/abs/10.1029/2020JE006418> (e2020JE006418 2020JE006418) doi: <https://doi.org/10.1029/2020JE006418>
- 2365 Volwerk, M., Kivelson, M. G., & Khurana, K. K. (2001). Wave activity in
 2366 Europa's wake: Implications for ion pickup. *Journal of Geophysical Re-*
 2367 *search: Space Physics*, *106*(A11), 26033–26048. Retrieved from <https://agupubs.onlinelibrary.wiley.com/doi/abs/10.1029/2000JA000347> doi:
 2368 <https://doi.org/10.1029/2000JA000347>
- 2369 Vorbburger, A., Wurz, P., Lammer, H., Barabash, S., & Mousis, O. (2015).
 2370 Monte-Carlo simulation of Callisto's exosphere. *Icarus*, *262*, 14–29. Re-
 2371 tried from <https://www.sciencedirect.com/science/article/pii/S0019103515003401> doi: <https://doi.org/10.1016/j.icarus.2015.07.035>
- 2372 Wedlund, C., Bodewits, Dennis, Alho, Markku, Hoekstra, Ronnie, Behar, Eti-
 2373 enne, Gronoff, Guillaume, ... Beth, Arnaud (2019). Solar wind charge
 2374 exchange in cometary atmospheres - I. Charge-changing and ionization
 2375 cross sections for He and H particles in H₂O. *A&A*, *630*, A35. Re-
 2376 tried from <https://doi.org/10.1051/0004-6361/201834848> doi:
 2377 [10.1051/0004-6361/201834848](https://doi.org/10.1051/0004-6361/201834848)
- 2378 Wulms, V., Saur, J., Strobel, D. F., Simon, S., & Mitchell, D. G. (2010, June). En-
 2379 ergetic neutral atoms from Titan: Particle simulations in draped magnetic and
- 2380
- 2381
- 2382
- 2383
- 2384

- 2385 electric fields. *Journal of Geophysical Research (Space Physics)*, 115, A06310,
2386 doi: 10.1029/2009JA014893.
- 2387 Zimmer, C., Khurana, K. K., & Kivelson, M. G. (2000). Subsurface Oceans on
2388 Europa and Callisto: Constraints from Galileo Magnetometer Observations.
2389 *Icarus*, 147(2), 329–347. doi: 10.1006/icar.2000.6456